UNIVERSITÀ DEGLI STUDI DI PADOVA

Dipartimento di Fisica e Astronomia “Galileo Galilei”

Erasmus Mundus Joint Master Degree in Experimental Nuclear Physics

Final Dissertation

Measurement of the D^0 meson production in Pb-Pb collisions with the ALICE experiment at the LHC

Thesis supervisor	Candidate
Prof. Marcello Lunardon	Michelangelo Traina
Thesis co-supervisors	
Dr. Andrea Dainese	
Dr. Andrea Rossi	

Academic Year 2018/2019

Contents

Introduction

The D^0 is the lightest particle with a charm quark and is particularly well suited for the study of charm production and interaction with the Quark-Gluon Plasma (QGP). This phase of matter is characterised by colour-charge deconfinement and quark and gluon degrees of freedom. It can form only when very high energy densities are reached. The ultra-relativistic lead-lead collisions studied at the LHC provide these conditions, allowing to investigate in-medium (QGP) interaction mechanisms for heavy quarks. The data collected by the ALICE experiment during the 2018 run allow the most precise measurement to date of such effects.

In this thesis work, the D^0 production in Pb-Pb collisions at $\sqrt{s_{\mathrm{NN}}} = 5.02$ TeV is measured via the reconstruction of its decay into a charged pion and kaon. The aim is to set important boundaries for the understanding of the interaction of charm quarks with the high-energy-density QCD medium, especially at transverse momenta in the 1-to-3 GeV/c range, where several concurring phenomena come into play.

The signal reconstruction is accomplished by studying the decay topology, in order to best exploit the excellent spatial resolution and particle-identification capabilities of the ALICE detector. In particular, a selection process discarding the so-called combinatorial background, distinctively abundant in the high-multiplicity environment of Pb-Pb collisions, is carried out. Each pair of tracks candidate to be considered as stemming from a D^0 decay must fulfil a set of conditions, which are optimised through the maximisation of the statistical significance of the signal. In order to circumvent gross misestimations due to possible background fluctuations, this optimisation uses signal samples produced through HIJING and PYTHIA Monte Carlo simulations. The overall goal is the extraction of the transverse momentum spectrum and nuclear modification factor, denoted by R_{AA}. The latter observable is the ratio of the transverse-momentum D^0 production spectra obtained in the Pb-Pb and in the pp colliding systems, where the latter is rescaled in the hypothesis that the heavy-ion collision be a superposition of independent nucleon-nucleon collisions. Whenever this hypothesis is correct, then $R_{AA} \approx 1$ within uncertainties – this has been observed to be the case, for instance, in p-Pb collisions, where an extended volume of QGP matter is not expected to form. However, if so-called final-state interactions between the charm quarks and the QGP take place, then a suppression of the nuclear modification factor for values of p_{T} larger than a few GeV/c is expected.

Neutral D meson transverse momentum spectrum and nuclear modification factor are thus evaluated and presented, accompanied by statistical and systematic uncertainties. The latter are estimated taking into account the several assumptions made throughout the analysis, mainly in the MC production of D^0's and during the yield extraction stage.

The described tasks are carried out with state-of-the-art computational tools such as dedicated data analysis framework AliRoot, C++ and Python programming languages. Furthermore, multivariate technique of Boosted Decision Trees is considered, in view of a possible enhancement of low-p_{T} signal extraction through a more effective optimisation of topological selection conditions.

In the first chapter (chapter 1) of this thesis the physics of Heavy-Ion Collisions is reviewed, along with the theory of strong interactions, Quantum Chromodynamics. In the latter case, the focus is in particular directed on heavy quark dynamics through a plasma of quarks and gluons.

The chapter 2 is devoted to the description of ALICE experiment at the CERN LHC. The detectors more strongly involved in the collection of data relevant in the present work are considered in detail.

The study of the decay geometry and the search for the optimal configuration of topological conditions to classify signal and background are subjects of chapter 3. The lowest transverse momentum bin analysed in this work is taken into deeper consideration due to low signal purity in such range.

Signal extraction and the measurement of the observables of interest are covered in chapter 4. Moreover, a part of the chapter is devoted to the estimation of systematic uncertainties. The measured nuclear modification factor, as the most important observable to understand heavy quark energy loss through QGP, is compared to trends predicted by theoretical models and past experimental results, as well.

In the last chapter (chapter 5) a forest of boosted decision trees is employed to perform a multivariate optimisation of the topological cuts used for the lowest-p_{T} bin. The best signal-background classifier is found and tested to assess whether an improvement is possible with respect to traditional tools.

Chapter 1

Heavy-Ion Collisions and Heavy-Flavour Physics

When heavy ions are collided their structure and the sub-structure of the nucleons they consist of are simultaneously probed, with a relative importance that depends on the energy scales and the geometry at which each event occurs. Heavy ions colliding at ultra-relativistic energies produce thermodynamical conditions that are hypothesised to have occurred within the first few microseconds after the Universe birth. In fact, at very high energy density and temperature, quarks and gluons are expected to be in a quasi-free state, named quark-gluon plasma (QGP). The study of this phase is essential to answer questions at the core of quantum chromodynamics – the theory of the strong interaction – and cosmology. Among the experiments that have undertaken this endeavour, ALICE is one of the leading, operating at energy scales of the TeV per nucleon pair. The fact that in a heavy-ion collision (HIC) both nuclear and sub-nuclear structure are, in general, involved implies that a huge variety of processes can take place, and the very large particle *multiplicity* is a challenge at the boundaries of modern detection technology.

In this chapter the probabilistic Glauber model of heavy ion collisions is first introduced, to then move on to a brief overview of Quantum Chromodynamics (QCD), the theory describing strong interactions, which are predominant at LHC energy scales. The concept of Quark-Gluon Plasma, the main subject of study at ALICE, is then presented, devoting particular attention to its formation and evolution as a macroscopic strongly-interacting system. One of its best probes, heavy flavour quarks (HF), is subsequently taken into consideration, briefly listing the main interaction mechanisms, and discussing the dynamics through the plasma. Finally, the most important physical quantity as far as the understanding of HF energy exchange is concerned, the nuclear modification factor, denoted as R_{AA}, is introduced. This is also important to comprehend the role of nuclear effects in modifying heavy flavour differential yields with respect to proton-proton collisions.

1.1 HIC Theory

A model describing the physics of a heavy-ion collision must take into consideration its geometry as well as the nature of the interactions occurring, as accurately as possible. While, in principle, at energies below the Coulomb barrier nuclei can be treated as point-like objects; at the opposite end of the currently *accessible* spectrum, at energies involving the colour force, one needs take into account the full spatial configuration of the nuclei and of the partons composing them. This, in practice, is not possible, so that resorting to probabilistic models of such processes is necessary. The Glauber model [1] successfully describes the geometry of a heavy ion collision and is used to classify recorded collisions on the basis of their "centrality".

1.1.1 Glauber Modeling of HIC Geometry

Colliding nuclei are Lorentz-contracted in the traveling direction, so that only their transverse size is given doubling the usual expression for nuclear radii: $R_A \sim A^{\frac{1}{3}}$ fm. The associated collision geometry is normally characterised by means of the following quantities:

- The impact parameter, b;
- The number of participating nucleons, $\mathrm{N}_{\mathrm{part}}$;
- The number of collisions, $\mathrm{N}_{\mathrm{coll}}$.

Experimentally, the impact parameter cannot be assessed (and is not even well defined given the quantum nature of nuclei). In practice, the *centrality* of the event is used: collisions are subdivided in centrality classes employing the charged-particle multiplicity distribution, $\mathrm{d}\sigma/\mathrm{dN}_{\mathrm{ch}}$, relying on the monotonic relation between the impact parameter and the charged-particle multiplicity, N_{ch}.[1]

The number of participating nucleons quantifies how many nucleons occupying the overlap volume take part in the collision. When two nuclei collide, the two numbers of participants can be summed, however, evaluating how many nucleon-nucleon collisions occur requires a detailed knowledge of the nuclear profile functions of both.

The total number of incoherent nucleon-nucleon collisions is thus estimated taking into account the distributions of nucleons for both nuclei and their interaction cross section.

---

[1] The total number of particles measured in the detectors after a heavy-ion collision is commonly referred to as multiplicity. The importance of this observable arises from the information it provides concerning the centrality and the energy density reached in the collision. Its most naive estimate in AA collisions consists in the reference for proton-proton collisions rescaled by the total number of possible incoherent nucleon-nucleon scatterings. Expectedly, this usually represents a considerable overestimate of the number of produced particles, thus demonstrating the presence of collective behaviour [2].

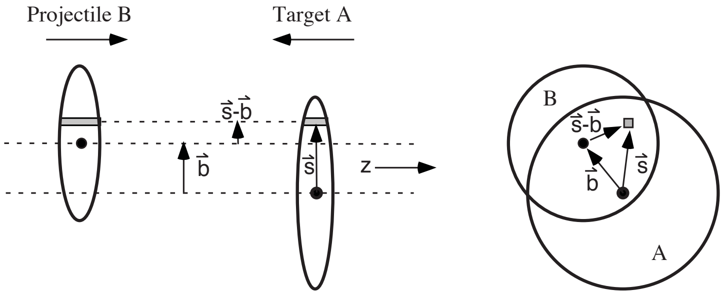

Figure 1.1: Glauber geometrical schematisation of a heavy-ion collision. Longitudinal and transverse views [3].

The Glauber model allows the computation of b, $\mathrm{N_{part}}$ and $\mathrm{N_{coll}}$. Here, its formulation in the (optical) limit of smooth continuous nucleon distribution functions is considered. Given two nuclei colliding at an impact parameter b, the infinitesimal flux tube at a transverse position $\vec{s}$ with respect to the barycentre of the target identified as A constitutes a target-projectile overlap region; as represented in figure 1.1. The probability per unit-transverse-area of finding a nucleon in such volume reads:

$$T_A(\vec{s}) = \int \mathrm{d}z_A \; \rho_A(\vec{s} - z_A), \tag{1.1}$$

where $\rho_A(\vec{s} - z_A)$ is the unit-volume probability of finding a nucleon at position z_A along the flux tube, normalised to unity. Combining this information for the two ions, two nucleons will be located in the overlapping target and projectile flux tubes with a transverse-area probability density of:

$$T_{AB}(b) = \int \mathrm{d}^2\mathrm{s} \; T_A(\vec{s}) T_B(\vec{s} - \vec{b}), \tag{1.2}$$

$\mathrm{d}^2\mathrm{s}$ representing the tubes surface element. The probability of having n nucleon-nucleon collisions can thus be extracted as:

$$\mathbb{P}(n, b) = \binom{AB}{n} \left[T_{AB}(b)\sigma_{\mathrm{nn}}^{\mathrm{inel}}\right]^n \left[1 - T_{AB}(b)\sigma_{\mathrm{nn}}^{\mathrm{inel}}\right]^{AB-n}. \tag{1.3}$$

This expression is justified observing that, out of the total number of possible interactions, AB, one needs only consider those cases involving n collisions. Each of the latter, will overall be $\left[T_{AB}(b)\sigma_{\mathrm{nn}}^{\mathrm{inel}}\right]^n \cdot \left[1 - T_{AB}(b)\sigma_{\mathrm{nn}}^{\mathrm{inel}}\right]^{AB-n}$ probable, since n collisions and $AB - n$ misses occur.

The total number of binary collisions for a given impact parameter will then be:

$$\mathrm{N_{coll}}(b) = \sum_{n=1}^{AB} n\mathbb{P}(n, b) = AB T_{AB}(b)\sigma_{\mathrm{nn}}^{\mathrm{inel}}. \tag{1.4}$$

On the other hand, the number of participating nucleons for a given impact parameter will be:

$$\begin{aligned} \mathrm{N_{part}}(b) = A \int \mathrm{d}^2 s \; T_A(\vec{s}) \Big\{ 1 - \left[1 - T_B(\vec{s} - \vec{b})\sigma_{\mathrm{nn}}^{\mathrm{inel}}\right]^B \Big\} \\ + B \int \mathrm{d}^2 s \; T_B(\vec{s} - \vec{b}) \Big\{ 1 - \left[1 - T_A(\vec{s})\sigma_{\mathrm{nn}}^{\mathrm{inel}}\right]^A \Big\}. \end{aligned} \tag{1.5}$$

Here, the two similar terms represent participants contributions from the two ions. The integral factor, more specifically, amounts to the fraction of nucleons associated to one ion involved in the process, computed integrating over the flux tube surface the joint probability per unit-area that one such nucleon is found in the region of interest and that all the nucleons present in the overlap volume of the other nucleus participate in the interaction.

1.1.2 Experimental Observables Related to the Collision Geometry

Just as in the case of the impact parameter, neither N_{part}, nor N_{coll} are directly measurable. Instead their averages can be calculated via mapping procedures, where a measured distribution is mapped to the corresponding distribution obtained from phenomenological analytic or Monte Carlo Glauber calculations. This is done by defining centrality classes in both the measured and calculated distributions and then connecting the mean values from the same centrality class [3].

Experimentally, observables tightly tied to the collision geometry are the charged particle multiplicity, i.e., the number of charged particles counted during an event, and the energy of remnants of the nuclei traveling in the beam direction: the so-called zero degree energy.

The multiplicity allows the subdivision of events in centrality classes. This is done as shown in the plot in figure 1.2, exploiting its monotonic relationship with the impact parameter.

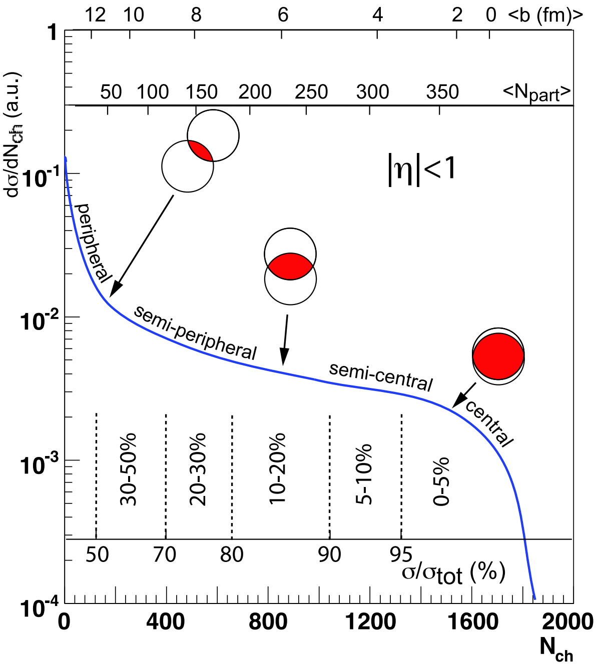

Figure 1.2: The charged particle multiplicity spectrum as a means for classifying a heavy-ion collision based on its centrality and number of participating nucleons [3].

The classes can be defined by means of the fraction of the total integral of the multiplicity distribution over $\mathrm{N_{ch}}$, linking central events to the highest multiplicities and peripheral events to the lowest multiplicities. The consequent extraction of average values of $\mathrm{N_{part}}$ and $\mathrm{N_{coll}}$ in a given class is based on the hypothesis that the multiplicity distribution stem from both soft and hard processes,[2] associated to $\mathrm{N_{part}}$ and $\mathrm{N_{coll}}$, respectively. In practice the experimental multiplicity distribution is reproduced through a linear combination of simulated $\mathrm{N_{part}}$ and $\mathrm{N_{coll}}$ distributions. Once the coefficients of such linear combination are found, centrality classes are defined for the fitting, linear-combined distribution, too. In this way, the average values of $\mathrm{N_{part}}$ and $\mathrm{N_{coll}}$ leading to the $\mathrm{N_{ch}}$ value which is reference for a centrality class can be computed.

The zero degree energy is linked to the number of nucleons that do not participate in the collision, also called *spectators*. In ALICE, its measurement is carried out by the Zero Degree Calorimeters (ZDC). Once measured, it can be used to define centrality classes and obtain estimates for the discussed quantities, too. However, fragment formation amongst the spectator nucleons breaks the simple linear and monotonic relation in the measured variables, since some spectator nucleons are bound into light nuclear fragments that have a charge over mass ratio similar to the beam, therefore, remaining inside the beam-pipe, undetected by the ZDC. Consequently, the ZDC information needs to be correlated to another quantity that has a monotonic relation with the number of participating nucleons [4].

1.2 The Quark-Gluon Plasma

The interaction landscape of ultra-relativistic heavy ion collisions is dominated by the strong force. In particular, the trend of the strong coupling strength, α_s, which predicts decreasing interaction strengths for high values of the transferred momentum, as opposed to QED, leads to the hypothesis of an asymptotic high-temperature state of deconfined quarks and gluons: the quark-gluon plasma. The properties of strongly-interacting matter in such regime, quite different from the standard nuclear matter conditions, can thus be investigated in HIC experiments, at present the only physical systems able to reach such conditions on Earth.[3]

To better appreciate the characteristics of high-temperature QCD, a brief overview of its features as a quantum field theory is provided subsequently.

1.2.1 Quantum Chromodynamics

Quantum chromodynamics is the theory of strong interactions. Its Lagrangian is written in terms of quarks and gluons, objects possessing a colour charge – the property

---

[2] The adjectives soft and hard refer to the scales of momentum transfer involved in such processes.

[3] Deconfined matter might exist in nature in the core of superdense neutron stars [5].

characterising strongly-interacting particles. The fact that gluons, i.e., the strong force carriers, are colourful is a peculiarity of QCD as a non-abelian gauge theory. Quarks, the theory fermion fields, are colour triplets and come in six flavours: *up*, *down*, *strange*, *charm*, *beauty* and *top*. Their mass spans a range going from 1-2 MeV/c^2 to 170 GeV/c^2, where the extreme values are associated to the up and top quarks, respectively. Multiplets of quarks are called *hadrons*. These objects constitute the majority (in mass) of detectable matter in the physical world and are colourless (or colour singlets), being formed by ensembles of particles whose net colour amounts to zero.[4]

Confinement and Asymptotic Freedom

The most outstanding features of QCD are colour confinement and asymptotic freedom. These properties explain the short range character of the strong interaction and why free quarks cannot be observed.

Confinement refers to the fact that colourful objects cannot exist as free asymptotic states, but need be bound in hadrons such as baryons (three-fold ensembles of quarks), or mesons (mixed-flavour quark-antiquark pairs), confined in regions less extended than the QCD spatial scale of $\sim \Lambda_{\mathrm{QCD}}^{-1} \sim 1$ fm. This holds for quarks and gluons, both being colour multiplets. Confinement can be more easily understood through the following expression for the static quark-antiquark potential:

$$V(r) = -\frac{4}{3}\frac{\alpha_s}{r} + kr. \tag{1.6}$$

Observing how the potential density of such a system increases linearly in distance, the reason behind confinement is apparent. When q and $\bar{q}$ get farther in space, the creation of another pair is energetically favourable, so that in practice none of them goes unpaired. A simple representation of this situation is shown in figure 1.3.

Figure 1.3: A pictorial representation of QCD confinement for a generic meson. Figure adapted from Quora: What is quark colour confinement?.

The parton[5] energy loss mechanism in vacuum has *hadronisation* as a net effect, and can be interpreted in terms of confinement. The current picture has quarks and gluons

---

[4] This is equivalent to saying that they consist of an equal number of quarks of different colours, or of a quark-antiquark pair.

[5] Parton is a generic word used to indicate quarks and gluons as elementary constituents of hadrons. It stems from the so-called Parton Model, whose basic assumption was that some objects called partons inside the proton are basically free.

fragmenting their momenta as follows: quarks release energy by radiating gluons that continuously transform into $q\bar{q}$ pairs as a consequence of confinement. These, in turn, emit more gluons and end up forming colour singlets, i.e., baryons and mesons, with other quarks. In this way, the initial momentum of a parton is basically distributed to many others (fragmentation) and overall results in the formation of hadrons (hence the term hadronisation).

Asymptotic freedom, on the other hand, can be explained by introducing a screening factor, so that the potential becomes:

$$V(r) = \Big(-\frac{4}{3}\frac{\alpha_s}{r} + kr \Big) e^{-\frac{r}{R_D}}, \tag{1.7}$$

where R_D is the Debye radius, setting the maximum distance at which the two quarks can be considered as bound. In this way, as the distance grows beyond R_D, the exponential decrease overcomes the linear growth of the first factor, thus weakening the strength of the interaction. Physically, an intuitive argument justifying the addition of the exponential factor is the following: at short distances, the presence of free colour charges carried by exchanged gluons acts as a screen for the potential. Actually, R_D itself is reduced due to the presence of free colourful objects. In this regime, quarks and gluons can be regarded as locally free.

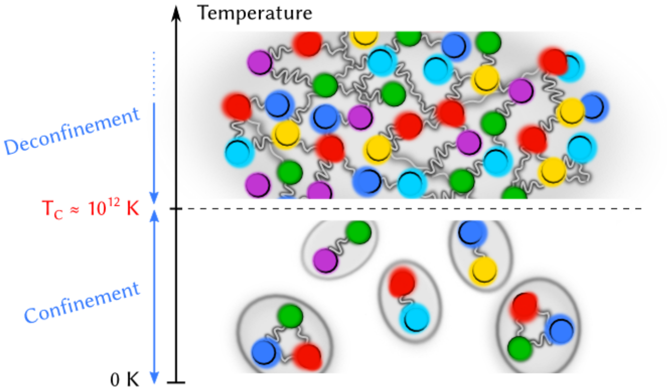

Figure 1.4: A quantum-chromodynamical ensemble can experience asymptotic freedom in conditions of very high temperature (or energy density). The critical temperature at which the transition occurs is currently estimated to be ≈ 155 MeV, equivalent to an order of magnitude of $\sim 10^{12}$ K. Figure adapted from CERN Database: Phase transition to QGP matter: confined vs deconfined matter.

A quantum-chromodynamics asymptotically free ensemble alters the mechanisms of energy exchange of partons traveling across it and thus can have an impact on the production yields of different species of hadrons. This is the case of a plasma of quarks and gluons, where the temperature and/or the energy density are high enough to achieve the deconfinement of partons, as shown in figure 1.4. As a matter of fact, the differential production yields of D mesons as a result of a heavy-ion collision are expected to differ depending on whether the system where they originated experiences asymptotic freedom or not.

Strong Coupling Strength Running

Confinement and asymptotic freedom are tightly tied to the dependence of the strong coupling strength on the energy scale of a given process, $\mathcal{Q}^2$. This is usually referred to as α_s running. In the one-loop approximation, equivalent to $\mathcal{Q}^2 \gg \mu^2$, its dependence on $\mathcal{Q}^2$ reads:

$$\alpha_s(\mathcal{Q}^2) = \frac{\alpha_s(\mu^2)}{1 + [\alpha_s(\mu^2)/12\pi](11n - 2f)\log(\mathcal{Q}^2/\mu^2)}. \tag{1.8}$$

Here, $\alpha_s(\mu^2)$ is a reference value of the coupling that must be measured or inferred at an energy scale μ^2, n is the number of colours of the theory and f is the number of active flavours (3 and 6, respectively, for the Standard Model). It should be observed that, since a reference value of α_s is needed to estimate it at any other scale, QCD does not predict its value; rather, only its trend.

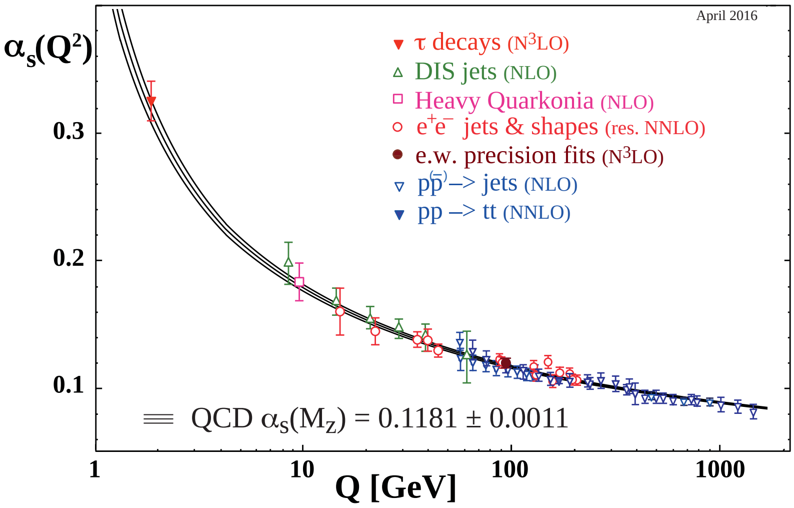

Figure 1.5: Strong coupling strength running as a function of the transferred momentum. Figure adapted from Particle Data Group 2018 Review of Particle Physics.

The $\mathcal{Q}^2$ dependence of the strong coupling strength makes it clear that the higher the energy, the weaker the coupling. So, perturbative expansions – used at low energies for field theories such as QED – can actually be employed at high energies in QCD. On the other hand, in the non-perturbative regime, QCD on the lattice, or LQCD, is presently preferred as an approach. Basically consisting in a hypercubic discretisation of space-time, it locates quark fields inside the a^3 volume cubes, whereas gauge fields at their edges. The spacing assumption brings along systematic and statistical uncertainties that can be estimated. As $a \to 0$, the continuum theory is restored. Lattice theories are systematically improvable and allow the evaluation of non-perturbative quantities in cases of strongly interacting gauge fields, as for QCD [6].

Figure 1.5 illustrates the trend of α_s as a function of $\mathcal{Q}$: experiments confirm the theoretical predictions concerning its behaviour.

1.2.2 Thermodynamics of Hadrons and Quarks

The change of *microscopic* conditions in different energetic regimes has as a consequence a variation in macroscopic or rather collective behaviour. A phase diagram is a way of illustrating such transformations.

The exact structure of the QCD phase diagram is still unknown. As an example, it might have a critical point, that is, a point beyond which (in a direction or the other) phase boundaries vanish. On the other hand, even before the discovery of QCD, the observation of increasing hadronic resonances for increasing temperatures and the basic idea that at high densities hadrons would start to "overlap" paved the way for the theorisation of a phase diagram [5]. Actual and hypothetical domains of strongly-interacting matter phases are shown in figure 1.6.

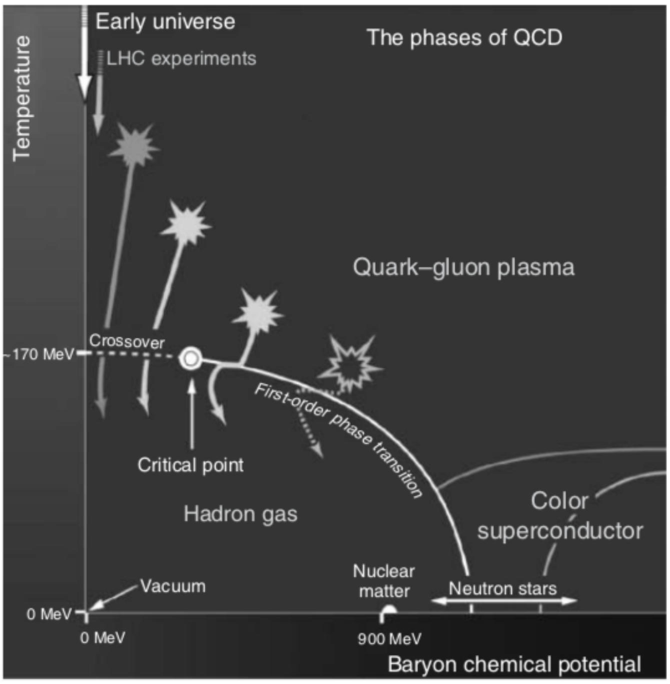

Figure 1.6: QCD phase diagram. Temperature and baryon chemical potential, as intensive quantities characterising a macroscopic, strongly-interacting system, are used to define the different phases it can experience [5].

The QCD phase diagram tracks the evolution of collective behaviour of QCD matter, as determined by temperature and baryon chemical potential. The latter quantity is defined as: $\mu_{\mathrm{B}} = \partial_{\mathrm{N_B}}\mathrm{E}$, and represents the energy needed for a unitary increase of the net number of baryons in the system. The energy density of the system and this quantity are monotonically related, as a larger density of baryons ($\rho_{\mathrm{B}} \propto \mu_{\mathrm{B}}$) actually leads to a growth in energy density.

Within the curve denoted with "First-order phase transition",[6] nuclear matter is described as being in a *hadron gas* state. In reality, for low temperatures and $\mu_{\mathrm{B}} \sim 1$ GeV, strongly-interacting matter is in the nuclear form. It is by raising temperature that a gaseous hadronic phase is reached. This state is usually described employing the Hagedorn model of a Resonant Gas [7]. In practice, the QCD system appears overall as a big excited hadron consisting of hadronic states spanning a wide mass spectrum. This has discrete nature for low mass, in the sense that well-known hadrons can be distinguished from one another, and approaches a continuum for large masses, as the width of the excited states lines and their spacing become comparable.

When (μ_{B}, T) lie in the extended region beyond the first-order transition boundary, QGP exists. As a matter of fact, proving the existence of the quark-gluon plasma is not straightforward. On the other hand, the evidence collected at ALICE and SPS at the LHC, and at the Alternating Gradient Synchrotron (AGS) and Relativistic Heavy-Ion Collider (RHIC) at BNL so far is explained by assuming its existence. For this reason, although it might not behave exactly as predicted, the phase of QCD matter in the discussed (μ_{B}, T) regime is described as a plasma of quarks and gluons. For relatively low values of the baryon chemical potential, the phase transition occurs around $\mathrm{T} \approx 155$ MeV, as computed through lattice calculations. Then, the critical temperature decreases as the baryon density goes up. The $\mu_{\mathrm{B}} \gg 1$ GeV range may be probed to verify speculations about colour superconductivity as caused by the formation of QCD Cooper pairs; yet, it is inaccessible by means of heavy-ion reactions.

When a QCD system transitions to a plasma of quarks and gluons, new degrees of freedom associated to these objects are available. Therefore, intensive thermodynamical quantities such as temperature and pressure can be influenced by their presence. The extreme example of an ideal gas of quarks and gluons can be taken into consideration in the limit of infinite temperature. In such scenario, the pressure is proportional to number of degrees of freedom and to the fourth power of temperature; a behaviour far from the one of an ideal macroscopic gas of atoms.

---

[6] The free energy is usually employed as a classifier of phase transition. The order of a transition is determined by the first order of the free energy derivative that exhibits discontinuities. Those transitions that involve no discontinuity whatsoever are instead called *crossovers*.

1.2.3 QGP "Birth", Evolution and "Death"

The heavy-ion collisions taking place at the LHC probe regions of baryon chemical potential well below the values characteristic for nuclear matter. The initial temperatures of the HIC-resulting medium, on the other hand, are of hundreds of MeV and in particular above the critical boundary.[7] Quark-gluon plasma is expected to form in this scenario.

The evolution of a system of colliding heavy ions is not fully understood at present. At very high energies, the pre-collision gluon densities are expected to saturate, originating a so-called *colour glass condensate*. In other words, gluons predominate this first stage of the collision, closely packed in asymptotic freedom conditions. Afterwards, QGP is thought to form, produced by the traveling CGC gluon sheets (glasma) in an overall thermalisation scenario. The QGP would then expand hydro-dynamically[8] and hadronise towards the Hagedorn phase, where, reached the critical temperature, the relative abundances of different hadrons should stabilise (chemical freeze-out). The momentum distribution would instead keep on evolving until the system gets diluted enough (kinetic freeze-out), with particles leaving the collision whereabouts. A space-time representation of a HIC evolution – from beams to kinetic freeze-out – is reported in figure 1.7.

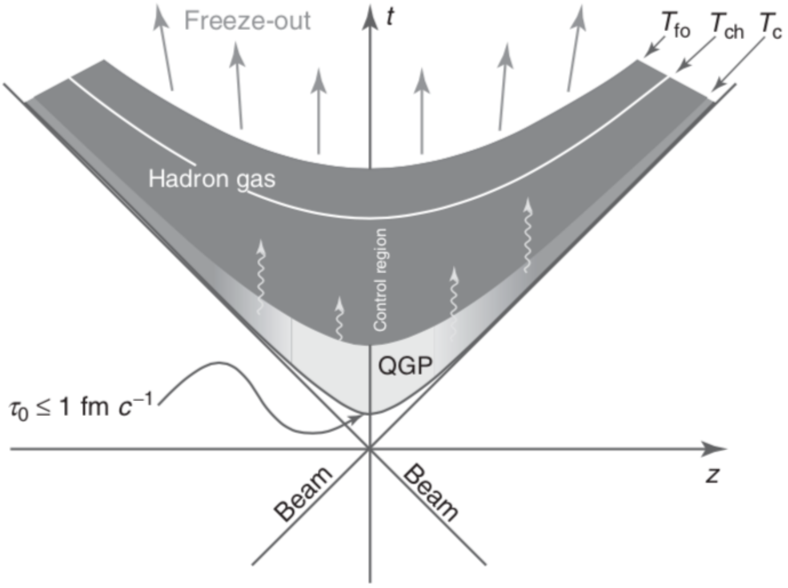

Figure 1.7: Space-time evolution of an ultra-relativistic heavy-ion collision [5].

---

[7] The initial temperature of the QCD medium created as a result of a HIC is inferred employing the low transverse-momentum photon spectrum. At these momenta the spectrum is reproduced by an exponential function whose slope parameter can be interpreted as the inverse of a temperature value representative of the average thermal conditions of the system. As an example, a value around 300 MeV has been measured for the 2.76 TeV per nucleon-pair lead-lead run in 2011 [8].

[8] Since such system is characterised by a low shear strain, it can be described by means of relativistic hydrodynamics.

Fireball Evolution Observables

The evolution of the HIC-system is object of current study and those global features supported by evidence at LHC and RHIC have been reported. In general, its properties are investigated by means of two categories of probes: soft and hard processes, which are characterised by the scales of momentum transfer they involve.

Particle multiplicity and identical boson-boson correlations are studied through soft probes. Particle multiplicity can be used to assess the initial energy density, with the two quantities being monotonically related.[9] The analysis of boson-boson correlation functions through interferometry constrains instead the system space-time distribution, setting the chemical freeze-out volume and how long it occurs after the CGC stage.

Another soft probe is the photon spectrum, which provides thermal information throughout the QGP phase and beyond. As already observed, it can be exploited to compute the average temperature of the system during its evolution, thanks to the fact that the photon mean free path is way larger than QCD scales. Photons produced during early stages of the collision are therefore able to cross the fireball without interacting. An important complication faced experimentally is the considerable photon background due to the decay of hadrons, which takes place from the freeze-out stages on.

Hard processes involve objects with momenta as high as 100 GeV/c. These are most suitable to study the mechanisms of energy loss in asymptotic freedom conditions. With pertinence to the case under study, heavy-flavour production is expected to occur before the formation of quark-gluon plasma. On the other hand, if such medium is created, heavy quarks interact with it via *gluon bremsstrahlung* and collisional processes, thus influencing the momentum distributions of heavy-flavour mesons. Another example of hard probe is the suppression of quarkonium states such as $c\bar{c}$ and $b\bar{b}$, which would occur as a result of in-medium colour screening promoting dissociation.

1.3 Heavy-Quark In-Medium Dynamics

The charm (c), beauty (b) and top (t) quarks are usually referred to as heavy. Their masses are presently estimated to amount to: $m_c = 1.27 \pm 0.02$ GeV, $m_b = 4.18^{+0.03}_{-0.02}$ GeV, and $m_t = 172.9 \pm 0.4$ GeV, respectively.[10] While the top quark is too unstable to hadronise, charmed and beauty-carrying hadronic states can be formed.

At ALICE, the charmed component stemming from hard processes is under study. It substantially encircles the family of D mesons, i.e., D^0, D^+, D^{*+} and D_s^+, the expectedly QGP-suppressed $c\bar{c}$ configuration, and charmed baryons (Λ_c^+, etc.). The D mesons all consist of a charm valence quark and a light valence antiquark (vice versa their antiparticles): $c\bar{u}$

---

[9] Intuitively, this is understandable as higher baryonic number implies higher initial energy density.

[10] The reported values are estimates of so-called "current-quark masses", in a mass independent subtraction scheme such as $\overline{\mathrm{MS}}$ at a scale $\mathcal{Q} \approx 2$ GeV [9].

and $c\bar{d}$ correspond to the electrically neutral and positively charged members, respectively. Resonances representing excited states of the latter are also observed. Moreover, the copious production of strange quarks resulting from gluon-gluon fusion processes – important in heavy-ion collisions – would have as a by-product the enhancement of the strange D meson, D_s^+, characterised by the fact that an antistrange quark, $\bar{s}$, substitutes its lighter antidown counterpart. On the other hand, beauty antiquarks can combine with lighter quarks leading to the members of the B family, or with their antiparticle (the b) thus forming the bottomonium configuration. As will be seen, for instance, it is important to distinguish so-called *prompt* and *feed-down* D^0's in order to investigate the effects that the hot and dense QCD-medium has on charmed meson production through vacuum fragmentation and/or recombination of charm quarks.[11]In fact, by definition prompt mesons belong to the latter category as far as their production is concerned, while feed-downs come from the decay of B mesons, and therefore do not provide any information in this respect.

1.3.1 In-Medium Heavy-Flavour Production

As already mentioned, heavy quarks are expected to be produced before the ~ 1 fm/c characteristic of QGP formation. This is due to the fact that the momentum transfer characterising hard processes – which scales inverse-proportionally to the time interval involved in the interaction – is quite high (large virtuality). As a consequence, post-collision scenarios are to be differentiated by the characteristic interactions partons undergo before re-experiencing confinement.

Proton-proton ultrarelativistic collisions carried out at LHC probe a no-QGP environment. This is the case because a high-temperature, dense medium does not form, nor can any nuclear effect take place. On the contrary, heavy ions are suitable to investigate such a medium. However, in these conditions nuclear collectivity must be taken into account, too.

Binary Scaling

In principle, if a nucleus-nucleus collision could be seen as a superposition of incoherent binary nucleon-nucleon collisions, then the corresponding heavy-flavour production cross section could be obtained simply by re-scaling the one describing the latter by the average number of collisions involved, $\langle \mathrm{N}_{\mathrm{coll}} \rangle$. This is usually called *binary scaling.* However, the fact that two composite systems characterised by their own internal physics – the nuclei – are collided, along with the later presence of a QCD-medium have a non-trivial impact on the heavy-flavour yields. Observables can be defined making use of this idea to extract quantitative information on the influence of these effects on the final hadron relative abundances.

---

[11] This hadronisation mode involves in-medium quarks found close-by in the phase space. It is also referred to as *coalescence.*

Employing the experimental pp and Pb-Pb spectra, binary scaling is equivalent to:

$$\left.\frac{\mathrm{d}^2\mathrm{N}^{hf}}{\mathrm{d}p_\mathrm{T}\mathrm{d}y}\right|_{\text{Pb-Pb}} = \mathrm{N}_\mathrm{coll}\Big|_{\text{Pb-Pb}} \left.\frac{\mathrm{d}^2\mathrm{N}^{hf}}{\mathrm{d}p_\mathrm{T}\mathrm{d}y}\right|_{\text{pp}}, \tag{1.9}$$

where all of the quantities are to be considered for a certain centrality range. The second factor in the right-hand side term is proportional to the heavy-flavour production cross section for a nucleon-nucleon collision and can be extracted combining three quantities:

$$\sigma_{pp}^{hf} \sim \sum_{i,j=q,\bar{q},g} f_i(x_i,\mathcal{Q}^2) \otimes f_j(x_j,\mathcal{Q}^2) \otimes \hat{\sigma}_{ij}^{hq}(x_i,x_j,\mathcal{Q}^2) \otimes D_{hq}^{hf}(z,\mathcal{Q}^2); \tag{1.10}$$

- The parton distribution function(s), $f_i(x_i,\mathcal{Q}^2)$;
  This quantity represents the probability of finding a given parton i inside the proton (at a resolution scale $\sim \mathcal{Q}^2$) with a fraction of its momentum equal to the Bjorken variable: $x_i = p_i/p_\mathrm{p}$.
- The hard partonic scattering cross section, $\hat{\sigma}_{ij}^{hq}(x_i,x_j,\mathcal{Q}^2)$;
  The global pp production of heavy quarks is ascribable to interactions between the constituting partons. The hard partonic scattering cross section quantifies the probability that a heavy-flavour object be produced in such interaction. Thanks to the high-energy scale involved, it can be evaluated through perturbative expansion.
- The fragmentation function(s), $D_{hq}^{hf}(z,\mathcal{Q}^2)$.
  The fragmentation function estimates the likelihood of hadronisation of the heavy parton, hq, into a heavy-flavour hadron, hf, with a fraction of its initial momentum: $z = p_{hf}/p_{hq}$.

In the nuclear case, the parton distribution functions and the fragmentation functions are modified when the extension of the colliding system interferes with the dynamics, while the short-distance part, that is, σ_{ij}^{hq}, is expected to remain unchanged if the virtuality is large enough [2]. These and other effects fall into the *initial-* and *final-state effects* categories. The underlying physics leads to deviations from a fixed scaling factor as a correction, when switching from pp to AA collisions.

Initial- and Final-State Effects

Initial-state effects are those that occur ahead of the QCD medium formation. They are tightly tied with the fact that it is nuclear matter to be collided. Firstly, the configuration of partons as constituents of nucleons is altered by the nuclear landscape. This is because an ensemble of free nucleons fundamentally differs from a nuclear bound system. In the second place, partonic dissipative processes may take place during the beginning of the collision. These can be multiple interactions within the original nucleus itself.

Final-state effects are instead associated to the interaction between heavy partons and the quark-gluon plasma. In-medium parton energy loss, as one of such effects, depends on several features of particles such as energy, mass/flavour and colour. Heavy and light quarks are thus to lose energy differently. The two main in-medium energy loss mechanisms, i.e., collisional and radiative, are represented in figure 1.8. In particular, low-momentum predominant collisional processes are such that heavy quark specific energy loss is always smaller than light quarks'. Gluon bremsstrahlung, on the other hand, being the dominant dissipative process for fast partons, also leads to larger energy loss for light quarks. Therefore, overall, the presence of QGP should have larger influence on light quarks than heavy.

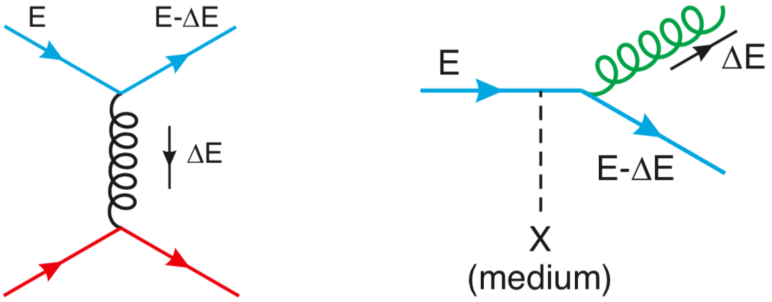

Figure 1.8: Main QCD energy loss mechanisms for a parton with energy E: scattering and gluon bremsstrahlung [3].

Besides dissipation through the medium, azimuthal anisotropy in the post-collision collective expansion is also considered a final-state effect. In particular, it is related to the hydrodynamics of the QGP as a viscous fluid. Low-momentum heavy quarks can take part in such process and their contribution can be studied. This topic is out of the scope of the present thesis and thus will not be further discussed.

1.3.2 The Nuclear Modification Factor

The net effect of interactions through the medium on the heavy flavour spectrum is a "shift" towards lower momenta. In fact, the momentum of heavy partons decreases through the aforementioned mechanisms. It is customary to quantify this effect through the so called *nuclear modification factor*:

$$R_{AA} = \frac{1}{\langle T_{AA} \rangle} \frac{\mathrm{dN}_{AA}/\mathrm{d}p_{\mathrm{T}}}{\mathrm{d}\sigma_{pp}/\mathrm{d}p_{\mathrm{T}}}, \tag{1.11}$$

where $\langle T_{AA} \rangle = \langle \mathrm{N_{coll}} \rangle / \sigma_{pp}^{\mathrm{inel}}$ is the nuclear overlap function averaged over the impact parameter range associated to the considered centrality class. This quantity is completely general in the sense that it can be estimated for all different particle species: mesons, photons, etc. A suppression of high-p_{T} particle production has for the first time been established experimentally at RHIC for neutral pions and charged hadrons. It was found that R_{AA} is significantly below one for $p_{\mathrm{T}} > 2-3$ GeV/c. On the other hand, for high-p_{T} photons, that do not interact strongly, $R_{AA} \approx 1$ was measured, indicating that the scaling approach with the number of binary collisions in fact is valid and that the suppression is due to strong interaction in the medium [5]. A measurement of the D mesons R_{AA} at ALICE is shown in figure 1.9. In 2015 Pb-Pb central collisions a R_{AA} much smaller than unity is measured, implying a strong energy loss of high-p_{T} mesons. Peripheral collisions, conversely, show a much weaker suppression.

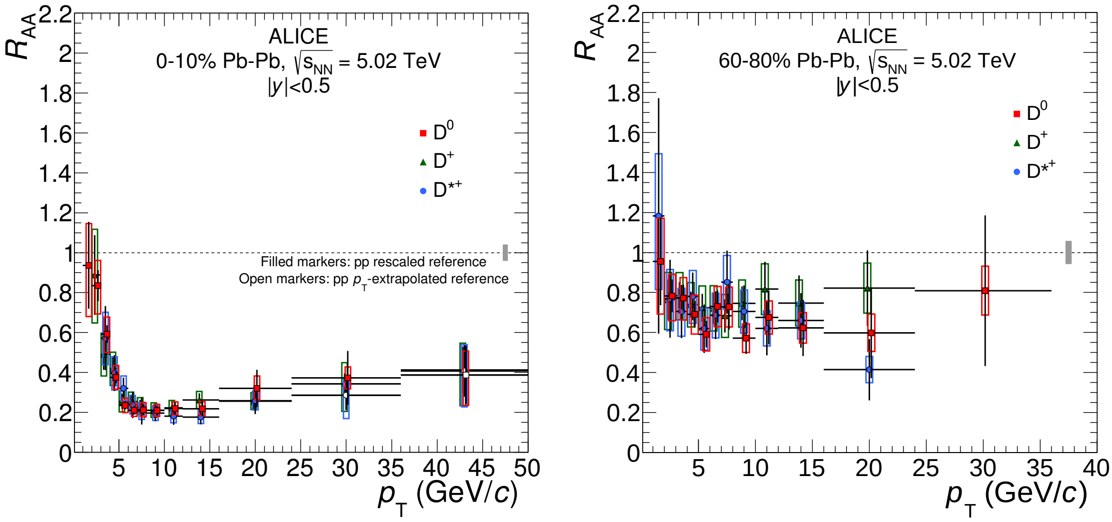

(a) *0-10% Centrality class.*

(b) *60-80% Centrality class.*

Figure 1.9: Nuclear modification factors extracted from the data collected at ALICE in 2015, at $\sqrt{s_{NN}} = 5.02$ TeV [10]. A stronger suppression is observed for more central collisions.

In this thesis, the nuclear modification factor of D^0 mesons is extracted from the experimental data collected during the recent 2018 Pb-Pb run, characterised by higher statistics and finer binning with respect to previous ones. In particular, the focus is chiefly directed on low-p_{T} bins, in the 0-10% centrality class. To such an end, the D^0 raw differential yields[12] are extracted in conditions of optimal *statistical significance*[13] and corrected through a global efficiency factor: the Pb-Pb p_{T}-spectrum is thus obtained. The R_{AA} is then computed employing the pp reference collected during the same run. Both statistical and systematic uncertainties are estimated and implemented in the process.

---

[12] Raw yields are thus called because they are extracted after a fraction of the signal of interest is rejected in the process of purification of the dataset. Once the efficiency of such procedure is known, so-called *corrected* yields are extracted.

[13] The statistical significance of a data sample – thoroughly defined later on in this thesis – is a measure of the purity of the signal extracted in a predominant background environment.

Chapter 2

A Large Ion Collider Experiment: ALICE

ALICE (A Large Ion Collider Experiment) is one of the main high-energy physics experiments taking place at the LHC particle collider, part of the CERN accelerator complex in Geneva, Switzerland. At ALICE, fully stripped lead (Pb) ions and protons are collided in order to study the behaviour of strongly interacting matter at centre-of-mass energies up to $\sqrt{s_{\mathrm{NN}}} = 5.5$ TeV per nucleon pair and $\sqrt{s} = 14$ TeV, respectively. The main goal is assessing the properties of the Quark-Gluon Plasma, which is expected to give important contributions in addressing fundamental questions such as asymptotic freedom and the QCD phase diagram.

In the present chapter a brief discussion of the Large Hadron Collider and its pre-acceleration complex paves the way for the description of ALICE experimental setup. The detectors primarily involved in the measurement of heavy flavour meson production are presented in detail, while the features of others are shortly mentioned. The track reconstruction process leading to the invariant mass distribution of the particle of interest is finally outlined, starting with the clusterisation of information, which ascribes a set of empirical quantities to a given event, to end with the invariant mass analysis of D^0 mesons.

2.1 The LHC

The LHC – acronym for *Large Hadron Collider* – is the largest structures in high-energy physics, boasting a 26.7 km circular perimeter. Based on the synchrotron functioning principles, it is able to collide hadrons at up to $\sqrt{s} = 14$ TeV, employing two proton or heavy-ion beams. The beam bunches circulate in opposite directions inside two different ultrahigh-vacuum pipes running through a ring of superconducting magnets. Accelerating radiofrequency cavities are located in a long straight section of the machine to increase the energy of travelling particles. Currently, the beams inside the LHC are employed for four main experiments: ALICE, ATLAS, CMS, and LHCb. ATLAS and CMS can be considered general-purpose experiments, meaning that they use general-purpose detectors to investigate the largest range of physics possible, while LHCb mainly focuses on the study of CP violation and the search for new physics through heavy-flavour hadron decays.

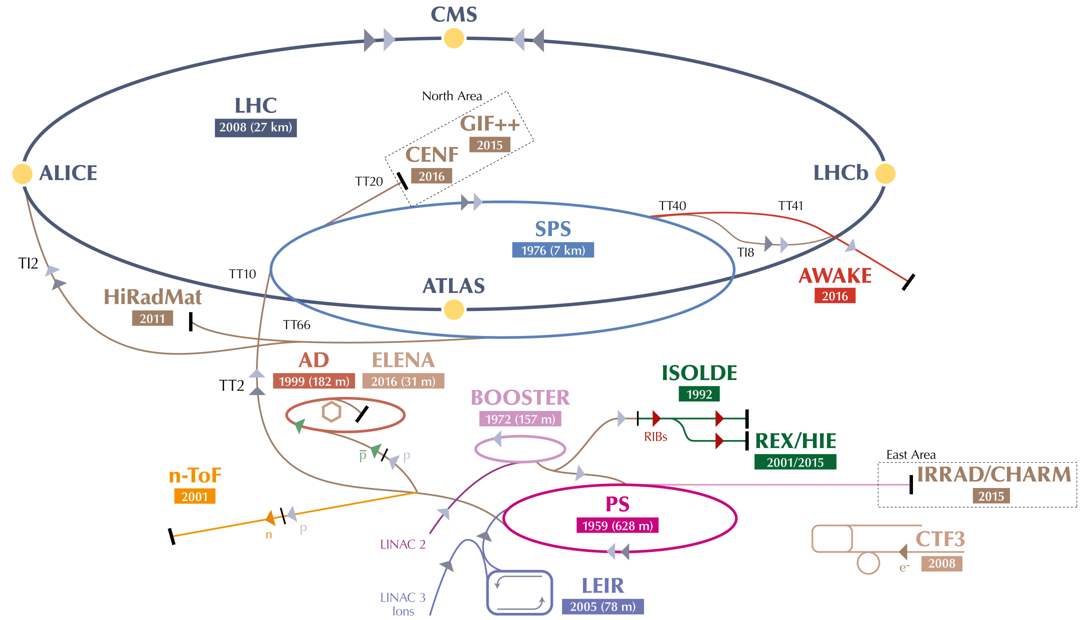

Figure 2.1: The CERN accelerator complex: a manifold injection chain, several secondary experiments and the Large Hadron Collider harbouring the four main experiments: ALICE, ATLAS, CMS and LHCb.

In order to reach the design energies, particles travelling through the LHC pipes first go through a pre-acceleration chain consisting of several accelerators directly connected to their sources. This ensemble of machines, represented in figure 2.1, is referred to as the CERN accelerator complex.

2.1.1 The Injection Chain

Proton and heavy ion bunches get to the LHC with energies of hundreds of GeV (per nucleon, in the ion case), where they are then further boosted at the TeV scale. In order to reach such energies, starting from their sources – a bottle of hydrogen gas and a tank of vaporised lead – they are first stripped of electrons by means of electric fields and absorbers and then go through several different acceleration systems. The machines involved in this process are:

- LINAC 2 – LINAC 3;

  These linear accelerators represent the first energisation stage for protons and heavy ions, respectively. LINAC 2 gets the protons to an energy of 50 MeV. The Pb ions, on the other hand, are brought to 4.2 MeV per nucleon by LINAC 3, and then stored in the LEIR [11].

- PS-BOOSTER – LEIR;
  The Proton Synchrotron Booster is the next step for hydrogen nuclei. Here, their energy is increased to 1.4 GeV. They are then sent to the PS. Heavy ions, instead, traverse the LEIR (Low Energy Ion Ring), where they are *bunched* before proceeding to the PS stage as well.

- PS;
  PS stands for Proton Synchrotron. From this point on, both H and Pb nuclei go through the same journey to arrive at the LHC. The final proton energy at this stage corresponds to 25 GeV.

- SPS;
  The Super Proton Synchrotron corresponds to the last pre-acceleration phase. Protons leave this device at 450 GeV, lead ions at 177.4 GeV per nucleon [11], being thus injected into the LHC two-fold pipe system.

2.1.2 LHC Layout and Design Goals

The goal of observing new phenomena in particle physics poses certain requirements on the features of a particle accelerator. Two among them are the centre-of-mass energy per nucleon, $\sqrt{s_{\mathrm{NN}}}$, and the number of collisions occurring per unit-time, that is, the event rate:

$$\sqrt{s_{\mathrm{NN}}} = \sqrt{\frac{Z_{\mathrm{X}}Z_{\mathrm{Y}}}{A_{\mathrm{X}}A_{\mathrm{Y}}}} \cdot \sqrt{s}; \tag{2.1}$$

$$\mathrm{R} = \sigma_{\mathrm{event}}(\hat{n}, \mathrm{E}_{cm})\mathcal{L}. \tag{2.2}$$

In these expressions, X and Y represent two nuclear species whose atomic number, Z, and mass number, A, are considered, $\sqrt{s}$ is the total centre-of-mass energy, σ_{event} is the cross section of the studied process and $\mathcal{L}$ is the *luminosity* of the collider. The luminosity measures its ability to produce the required number of interactions [12], and depends only on the beams characteristics. Its expression in the case of Gaussian beam axial distribution stems from the convolution of the colliding beam distributions and reads:

$$\mathcal{L} = \frac{n_b^2 \mathrm{N}_b f_{\mathrm{rv}} \gamma}{4\pi\epsilon_n\beta^*}\mathrm{F}, \tag{2.3}$$

where n_b is the number of particles per bunch, N_b, the number of bunches per beam, f_{rv}, the revolution frequency, γ, the relativistic gamma factor, ϵ_n, the normalised transverse

System	Year(s)	$\sqrt{s_{\mathrm{NN}}}$ (TeV)	Integrated Luminosity
Pb-Pb	2010-2011	2.76	$\sim 75\ \mu\mathrm{b}^{-1}$
	2015	5.02	$\sim 250\ \mu\mathrm{b}^{-1}$
	2018	5.02	$\sim 1\ \mathrm{nb}^{-1}$

Table 2.1: Overview of the energies and the integrated luminosity L_{int} that was collected by the ALICE experiment in several years of running [13].

emittance[1], β^*, the beta function[2] at the collision point and F, the geometric luminosity reduction factor due to the crossing angle at the interaction position:

$$\mathrm{F} = 1 \Bigg/ \sqrt{1 + \left(\frac{\vartheta_c \sigma_z}{2\sigma^*}\right)^2}, \tag{2.4}$$

ϑ_c being the full crossing angle at the interaction point, σ_z, the RMS bunch length, and σ^*, the transverse RMS beam size at the interaction point.

At the Large Hadron Collider, the highest luminosity experiments are ATLAS and CMS, aiming at $\mathcal{L} = 10^{34}\ \mathrm{cm}^{-2}\mathrm{s}^{-1}$ in pp collisions. ALICE, and more generally heavy-ion runs, are expected to go as high as $\mathcal{L} = 10^{27}\ \mathrm{cm}^{-2}\mathrm{s}^{-1}$, corresponding to an interaction rate of 8 kHz.

On 25 November 2018, a new peak luminosity record of $6 \cdot 10^{27}\ \mathrm{cm}^{-2}\mathrm{s}^{-1}$ (i.e. six times the original LHC heavy ions design value!) was set in both ATLAS and CMS, [14]. However, during a run collisions themselves reduce the beams intensity and emittance, thus determining a decrease of the luminosity. For this reason, the value of luminosity integrated over time, $\mathcal{L}_{int}$, measured in barn^{-1}, is also considered. In table 2.1, the centre of mass energy for nucleon pair and the integrated luminosity collected by ALICE during the two main LHC runs[3] for Pb-Pb collisions are reported.

2.2 The ALICE Detection System

ALICE is a 10,000-ton experimental setup – 26 m long, 16 m high, and 16 m wide. It is located in a cavern 56 m below the ground. The detector is designed to measure the particles produced in the collisions which take place at the interaction point (IP), and their kinematical properties, so that the evolution of the system produced during these collisions can be reconstructed and studied [ALICE Experiment]. To do so, a variety of sub-detectors is used, each providing a different piece of information.

---

[1] The emittance quantifies the average dispersion of particles in position and momentum space. The normalised emittance, $\epsilon_n = \beta\gamma\epsilon$, is convenient to use because it does not depend on energy.

[2] The amplitude function $\beta(z)$ takes into account the single-particle motion, describing the dependence of the beam envelope on the beam axis coordinate, z. β^* represents its value at the interaction position.

[3] At present, the LHC has been running with research purpose twice. The first run took place from late 2009 to early 2013, followed by LS1, a two-year long shutdown period. The second run started in the first half of 2015 and concluded recently, in the end of 2018.

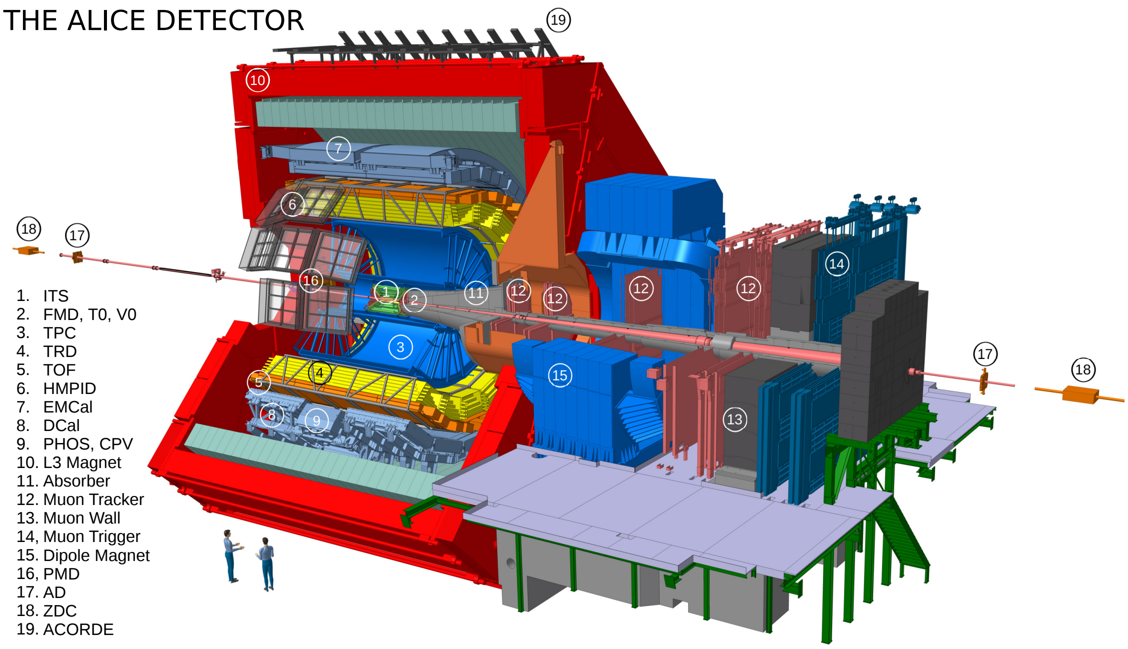

Figure 2.2: The ALICE setup and its 19 subdetectors. Figure adapted from CERN Database: ALICE Schematics.

The ALICE 19 sub-detectors, represented in figure 2.2, can be categorised in three main groups: the central-barrel detectors, the forward detectors and the muon spectrometer. At present, exploiting the LS2 long shutdown, some of them are being renovated or completely replaced. However, in this work, the configuration used to collect data during 2018 Pb-Pb run is going to be described. Before briefing on the setup features, the ALICE coordinate system is introduced. Also, the concept of pseudorapidity is presented.

The ALICE coordinate system is right-handed, orthogonal and Cartesian: the origin lies at the corresponding LHC interaction point, the z axis coincides with the average beam position and is directed LHC-anticlockwise. The x axis is chosen to point inwards, to the centre of the LHC, so that the y axis is approximately vertical, its positive half lying above the xz plane. Keeping this reference in mind, the pseudorapidity and the azimuthal angle characterise the emission direction of particles.

The pseudorapidity, η, is a measure of the angle between the xy plane and the direction of emission of a product of the collision. In reality, it stems from a more general quantity, the rapidity, usually denoted with y. The main difference between the two lies in the fact that the former is obtained in the limit of highly relativistic particles, starting from the latter.

$$y = \frac{1}{2}\ln\left(\frac{\mathrm{E}+p_z c}{\mathrm{E}-p_z c}\right); \tag{2.5}$$

$$\eta = -\ln\tan\frac{\vartheta}{2}; \tag{2.6}$$

where E is the total energy of the particle, p_z, its momentum z-component and ϑ, the corresponding polar angle. The necessity for the definition of the pseudorapidity arises due to the composite nature of the colliding particles and to the ease with which η can be obtained, compared to y, given that it is not always straightforward to identify particles and measure their energy. Additionally, the two quantities are in practice identical as long as ultra-relativistic objects are considered.

2.2.1 The Central-Barrel Detectors

The central-barrel detectors are thus named because they constitute the large central core of the experiment. Embedded in the solenoid magnet which produces a 0.5 T magnetic field parallel to the beam axis, these detectors basically carry out the tracking and contribute to the direct or indirect[4] identification of a large fraction of the particles produced in the collision. They are: the Inner Tracking System (ITS), the Time Projection Chamber (TPC), the Transition Radiation Detector (TRD), the Electromagnetic Calorimeter (EMCal), the Time of Flight (TOF), the Photon Spectrometer (PHOS) and the High Momentum Particle Identification Detector (HMPID). A brief description of each of these sub-detectors follows. For matters of simplicity, each of them is classified based on its main contribution to the experiment, although, as will be seen, some of them actually perform more than one task.

Tracking and Energy Measurement

The first three devices listed above are devoted to the tracking of electrically charged particles, also providing a measurement of their specific energy loss.

The ITS is the innermost object of the central-barrel ensemble. It consists of six coaxial cylindrical layers of silicon detectors surrounding the beam pipe: pixels (SPDs), drift (SDDs) and strips (SSDs), in ascending order of radius, which spans the 3.9-to-43 cm range. For all events located within $1\sigma = 5.3$ cm from the mean interaction point, it covers the $|\eta| < 0.9$ pseudorapidity interval. The ITS is responsible for the location of the *primary vertex* of the interaction, that is, where the collision occurs, with a resolution better than 100 μm. Furthermore, it is also strongly involved in the reconstruction of the *secondary vertex* of decaying unstable mesons such as D and B. In fact, the number of layers, along with their arrangement and segmentation were designed to optimise the track reconstruction efficiency. In particular, the outer radius is determined by the necessity to match tracks with those from the TPC, and the inner radius is the minimum allowed by the radius of the beam pipe [15]. A representation of the ITS detection layers is reported in figure 2.3.

---

[4] Neutral mesons or baryons such as the D^0 are not directly observed by means of these devices. Instead, they can be identified exploiting the tracks their electrically charged daughters leave across detectors.

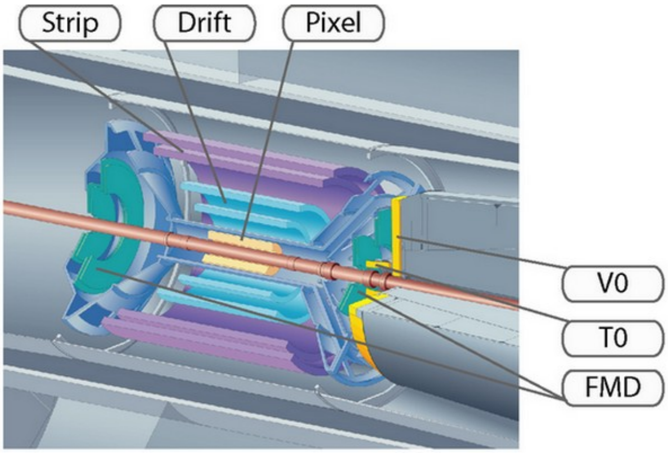

Figure 2.3: Close-up of the ALICE Inner Tracking System used to perform the measurements analysed in this work [3].

The ALICE time projection chamber is designed to provide charged-particle momentum measurements through tracking. Along with the SDDs and SSDs of the ITS, it also performs energy loss measurements for identification purpose. A schematic representation appears in figure 2.4. Its outer (1) and inner (5) cages comprehend a 88 m^3 drift volume filled with a 88:12-mixture of argon and carbon dioxide (Ar-CO$_2$). The central high-voltage cathode (6) is fixed at -100 kV with respect to the end plates (4), which are equipped with readout multi-wire proportional chambers (MWPC) (3). The TPC is also provided with a protective CO$_2$ gas envelope (2) installed for personnel and operational safety. The phase space covered by the TPC in pseudorapidity is $|\eta| < 0.9$ for tracks with full radial track length (matches in ITS, TRD, and TOF detectors); for reduced track length (at reduced momentum resolution), an acceptance up to about $|\eta| = 1.5$ is accessible. The TPC has full acceptance over the azimuth. A large transverse momentum range is covered from low

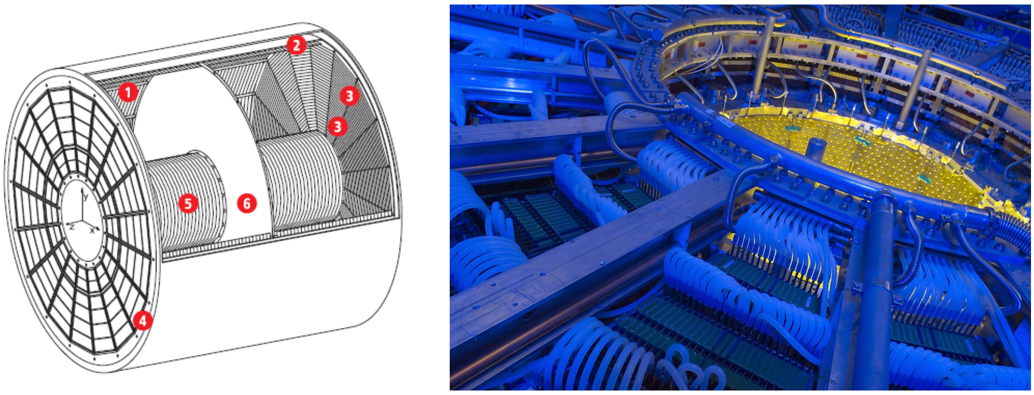

(a) *Schematisation of ALICE TPC.*

(b) *On-the-spot picture of the TPC*

Figure 2.4: ALICE Time Projection Chamber. Figures adapted from ALICE: Time Projection Chamber.

values of about 0.1 GeV/c up to 100 GeV/c with good resolution. Charged-particle tracks are thus reconstructed with up to 159 points in space [15].

The TRD detector, a six-fold stratification of Xe–CO_2-filled multi-wire proportional chambers, with a fibre/foam radiator in front of each chamber, is used for tracking and for electron identification via transition radiation and specific energy loss.

Particle Identification

In addition to the ITS and TPC contribution, the TOF plays a fundamental role in identification providing an indirect measurement of the particle speed through the evaluation of its time of flight. The precision of this measurement is better than 0.1 ns. In particular, for pions and kaons around 1 GeV/c, it is about 80 ps. The TOF has a surface area of 140 m^2 subdivided in 160 000 individual readout pads distributed over 53 Multi-gap Resistive-Plate Chamber (MRPC) strips. It is approximately located at a 4 m radius, and optimised for large acceptance and intermediate momenta. Its high granularity is dictated by the requirement of identifying, on an event-by-event basis, as many charged particles as possible. Particles are identified by comparing the measured time of flight to its expectation value, computed for each mass hypothesis from the track momentum and length [3].

The HMPID detector is a single-arm, 10 m^2 array of proximity-focusing ring imaging Cherenkov counters with liquid radiator and solid CsI photocathode evaporated on the segmented cathode of multi-wire proportional chambers. It extends the hadron identification capabilities toward higher momenta in about 10% of the barrel acceptance.

Finally, as already stated, the TRD is also employed for electron identification in the central barrel for momenta above 1 GeV/c. Below this momentum electrons can be identified via specific energy loss measurement in the TPC [15].

Photons and Jets

ALICE features two electromagnetic calorimeters. Their main goal is the detection of photons and jets.

PHOS is a high-resolution, high-granularity spectrometer covering a limited acceptance domain at central rapidity ($|\eta| < 0.12$). Its lead-tungstate ($PbWO_4$) scintillating crystals measure photons spanning the thermal-to-hard-QCD range.

EMCal was not present in the original design and has been installed in 2008 to enhance the jet[5] properties measurement capabilities such as production rates and fragmentation functions conjointly with the charged particle tracking in the other barrel detectors. A

---

[5] A high energy parton can turn into a shower of hadrons through multiple fragmentation processes. This is what is referred to as jet.

Pb-scintillator calorimeter with longitudinal WLS[6] fibres, read out via avalanche photo diodes, it is much more extended than PHOS, but has lower spatial and energetic resolution.

2.2.2 The Forward Detectors

ALICE Forward Detectors are thus called because of the relatively high-η regions they cover. Employed for triggering and multiplicity measurements, they are: the Photon Multiplicity Detector (PMD), the Forward Multiplicity Detector (FMD), the Cherenkov detector, T0, V0, a plastic scintillator, and the Zero Degree Calorimeter (ZDC).

The PMD features two planes of proportional counters whose goal is measuring the multiplicity and spatial distributions of photons.

The same kind of measurement for charged particles is carried out by the FMD, consisting of rings of strip detectors located along the beam pipe.

The pipe-surrounding T0 Cherenkov counters locate the longitudinal position of the event and perform a measurement of its occurrence time, which is used in the TOF time-of-flight measurement.

The V0 comprises two arrays of 32 scintillators positioned at both sides of the interaction point: V0A and V0C. It is mainly used to provide trigger signals and to estimate the centrality and event-plane angle[7] in Pb–Pb collisions.

Finally, a combination of proton (ZP) and neutron (ZN) calorimeters, the ZDC is arranged z-symmetrically with respect to the IP, and has as a goal that of counting the event spectator nucleons; a measurement of the centrality of the collision. It also includes two small electromagnetic calorimeters (ZEM) located only on one side of the IP, which detect the energy of particles emitted in a specific polar range.

2.2.3 The Muon spectrometer

In ALICE, in order to isolate the muon component, the high penetration capability of these particles is exploited, shielding most of the remaining radiation. The forward muon arm is primarily designed to measure the production of quarkonia (e.g., J/Ψ) by employing the $\mu^-\mu^+$ decay channel, and semi-mesonic decays of D and B mesons. Located at small angles to provide good acceptance down to zero transverse momentum, it consists of a composite absorber ($\approx 10\lambda_{\text{int}}$), made with layers of both high- and low-Z materials starting 90 cm from the vertex, a large dipole magnet with a 3 T·m field integral placed outside the solenoid magnet, and ten planes of very thin, high-granularity, cathode strip tracking stations. A second muon filter ($\approx 7\lambda_{\text{int}}$ of iron) at the end of the spectrometer and four planes of Resistive Plate Chambers are used for muon identification and triggering. The

---

[6] Wavelength-shifting fibres are made of materials that absorb and re-emit photons, thereby lowering their frequency.

[7] The event-plane angle is the angle at which nuclei collide in the transverse plane.

spectrometer is shielded by a dense conical absorber tube, of about 60 cm outer diameter, which protects the chambers from secondary particles created in the beam pipe [15].

2.3 Decay Reconstruction

Particles decaying within the detector geometry can be tracked and identified along with their daughters by means of the numerous ALICE detectors. The analysis of D-meson production involves primarily the ITS, the TPC and the TOF central-barrel detectors. The forward T0, V0 and ZDC also contribute with timing and triggering functions, and multiplicity and centrality assessment. A summary of their features can be found in table 2.2.

2.3.1 Track Reconstruction Strategy

The raw data collected by means of ALICE central-barrel detectors undergoes several processing steps. Schematically, these can be listed as follows [16]:

- Clusterisation;
  Information such as positions, signal amplitudes, signal times and cluster shapes of a group of adjacent firing cells is gathered, along with the associated error. This procedure takes place separately for each detector.

- Primary vertex reconstruction with SPD;
  Initially, the primary vertex z coordinate is reconstructed using pair of points that interacted with the SPD.

- Track reconstruction;
  The tracking procedure is subdivided into track finding and track fitting. The finding is done through an inward-outward algorithm coupled to the so-called Kalman filter [3, 17]. Tracks *seeds* are extracted using the primary vertex (reconstructed with SPD) and pairs of TPC clusters in adjacent pad rows, then propagated inward to the ITS. Through the ITS, a new track is found using sets of points not attached to the TPC prolongations. Then, it is propagated outwards using all the points found thus far and prolongated to the TRD, the TOF etc. Finally, a fitting of the track in the inward direction is performed, using all the clusters extracted previously. Each of the propagations is regulated by the Kalman filter. The track and associated covariance matrix are thus determined. The resolution of each track as a function of the transverse momentum evolves throughout the stages of the reconstruction. Usually, the so-called inverse-p_{T} resolution is considered:

  $$\frac{\sigma_{p_{\mathrm{T}}}}{p_{\mathrm{T}}} = p_{\mathrm{T}}\sigma_{1/p_{\mathrm{T}}}, \tag{2.7}$$

  its trend at the different reconstruction stages is shown in figure 2.5.

Detector	Polar Acceptance	Azimuthal Acceptance	Position	Technology	Purpose
SPD*	$\|\eta\| < 2.0$	full	$r = 3.9$ cm	Si pixel	tracking, vertex
	$\|\eta\| < 1.4$	full	$r = 7.6$ cm	Si pixel	tracking, vertex
SDD	$\|\eta\| < 0.9$	full	$r = 15$ cm	Si drift	tracking, PID
	$\|\eta\| < 0.9$	full	$r = 23.9$ cm	Si drift	tracking, PID
SSD	$\|\eta\| < 1.0$	full	$r = 38$ cm	Si strip	tracking, PID
	$\|\eta\| < 1.0$	full	$r = 43$ cm	Si strip	tracking, PID
TPC	$\|\eta\| < 0.9$	full	$85 < r/\text{cm} < 247$	Ar drift+MWPC	tracking, PID
TOF*	$\|\eta\| < 0.9$	full	$370 < r/\text{cm} < 399$	MRPC	PID
V0$*$	$2.8 < \eta < 5.1$	full	$z = 329$ cm	scintillation	charged particles
	$-3.7 < \eta < -1.7$	full	$z = -88$ cm	scintillation	charged particles
ZDC*	$\|\eta\| > 8.8$	full	$z = \pm 113$ m	W+quartz	forward neutrons
	$6.5 < \|\eta\| < 7.5$	$\phi < 10^\circ$	$z = \pm 113$ m	brass+quartz	forward protons
ZEM	$4.8 < \eta < 5.7$	$\|2\phi\| < 32^\circ$	$z = 7.3$ m	Pb+quartz	photons

Table 2.2: The main ALICE detectors involved in the D^0 meson production measurement. The transverse and longitudinal coordinates, r and z, respectively, are measured with respect to the ALICE interaction point [18]. The detectors marked with an asterisk (*) are used for triggering.

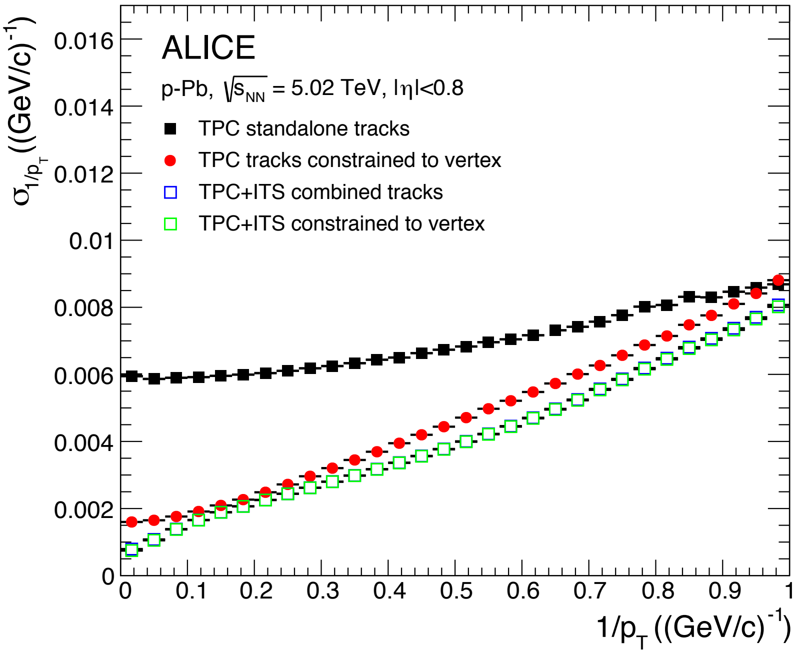

Figure 2.5: The p_T resolution for standalone TPC and ITS–TPC matched tracks with and without constraint to the vertex. The vertex constrain significantly improves the resolution of TPC standalone tracks. For ITS–TPC tracks, it has no effect (green and blue squares overlap) [18].

- Primary vertex reconstruction with tracks;

  Once tracks corresponding to a given event are found, the primary vertex of the collision is extracted anew. This leads to better resolution than SPD vertex.

- Secondary vertex reconstruction.

  In the tracking process, secondary vertices are also to be found. These are associated to decays of unstable particles into charged objects. The D^0 meson represents one such case as the charged pion and kaon it decays into leave two tracks across the detectors starting from a common secondary vertex. The selection of these tracks is based on their *distance of closest approach* (dca) to the primary vertex, as a first criterion. They are then joined into secondary vertex candidates and matched with the information obtained at the identification stage.

2.3.2 PID

The identity of particles of interest in the context of this thesis is assessed primarily with the TPC and the TOF. In the first case, a measurement of the momentum, the charge and the specific energy loss of the particle through the gaseous chamber provides such information. More specifically, the last quantity has a well-known trend described by Bethe-Bloch expression and different species with the same charge can be distinguished by means of the region they occupy in the (p/Z, dE/dx) space. An example of such curves

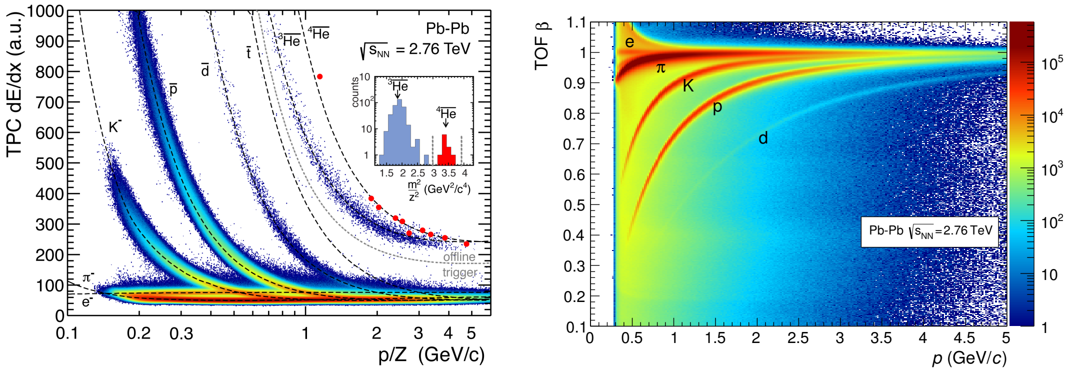

(a) *Measured dE/dx signal in the ALICE TPC versus magnetic rigidity, together with the expected curves for negatively-charged particles. The inset panel shows the TOF mass measurement which provides additional separation between* ^{3}*He and* ^{4}*He for tracks with* $p/Z >$ 2.3 *GeV/c.*

(b) *Distribution of* β *as measured by the TOF detector as a function of momentum for particles reaching the TOF in Pb–Pb interactions.*

Figure 2.6: Instances of identification plots for TPC and TOF in Pb-Pb interactions [18].

is shown in 2.6 (a). Due to a dE/dx resolution of about 6.5% in the 0–5% most central Pb–Pb collisions, particle ratios can be measured at a p_{T} of up to 20 GeV/c [3].

Identification through the time-of-flight detector is performed using the relativistic parameter β (i.e., the speed of the particle) and the momentum value estimated with the TPC. The former is measured using a start signal from the T0 detector and the TOF stop signal. This leads to separate regions associated to different particles in the plane spanned by the mentioned variables, as seen in figure 2.6 (b). The resolution of such time measurement in the centrality range 0–70% is about 80 ps for pions with a momentum around 1 GeV/c. This value includes the intrinsic detector resolution, the contribution from electronics and calibration, the uncertainty on the start time of the event, and the tracking and momentum resolution. TOF provides PID in the intermediate momentum range, up to 2.5 GeV/c for pions and kaons, and up to 4 GeV/c for protons [3].

2.3.3 Cut Optimisation. Invariant-Mass Analysis

The last stage leading to the extraction of D-meson raw yields consists in an optimisation of the selection conditions on the decay topology. It is an optimisation in the sense that those *cuts* that maximise the statistical significance of the signal are sought. Once these are found, the resulting invariant mass spectrum is analysed, thereby computing the raw yields. These will then be used to compute quantities of interest such as the nuclear modification factor, after the proper corrections are implemented. Further details in this respect are reported in the following chapter 3.

Chapter 3

D^0 Topological Selection

The D^0 meson is an electrically neutral particle. As such, it cannot be directly observed in ALICE detectors (and anyway decays before reaching them); rather, its main hadronic decay channel is exploited to measure it:

$$\begin{aligned} \mathrm{D}^0 &\rightarrow \mathrm{K}^- + \pi^+; \\ c\bar{u} &\rightarrow \bar{u}s + u\bar{d}. \end{aligned}$$

This is a weak decay as the flavour of the valence quarks of the involved hadrons changes. It has a branching fraction of 3.89 % [9]. The selection of D mesons is initially based on the distance between the primary and secondary vertices, namely, the decay length.[1] However, further topological variables are to be introduced in order to reject the abundant *combinatorial background*,[2] and extract the p_T-differential yields in the best signal-background classification conditions.[3] Such configuration can be found using a Monte Carlo (MC) signal sample produced by means of PYTHIA and HIJING event generators [19, 20] and a GEANT [21] model of the detection system. The background, on the other hand, is extracted as an interpolation of actual data sidebands. This strategy also allows to circumvent the possibility of a background fluctuation in the signal region, which would jeopardise the outcome of the optimisation analysis. However, it also is evidently sensitive to the accuracy of the simulation in reproducing the properties of the signal sample.

In the context of this analysis, it is also fundamental to differentiate between prompt and feed-down D mesons. In fact, given that the goal is measuring the nuclear modification factor of these particles to link it to charm energy loss through the quark-gluon plasma, the fraction of D^0's stemming from hadronisation only must be taken into account.

This chapter is subdivided in two main parts. Firstly, topological variables characterising the decay geometry are introduced, distinguishing single-track and track-pair variables.

---

[1] The D^0 mean lifetime is such that $c\tau \approx 123$ μm. This quantity is usually referred to as *mean proper decay length*.

[2] The background mostly consists of low-p_T primary tracks. The term combinatorial refers to the huge amount of combinations of vertices and tracks extracted throughout the reconstruction stage.

[3] In principle, the background trend could also be extracted by taking into account all the expected contaminating processes. However, this is not feasible in practice in the HIC high-multiplicity environment.

Correlations between these quantities as signal-background classifiers are also explored. Secondly, the procedure conducted to optimise the classification is explained in detail, introducing fundamental concepts such as the statistical significance and the fraction of prompt mesons. In the context of this section, the best-classifying configuration for topological variable is also reported, along with a detailed analysis of the lowest-momentum interval, where the subsequent signal extraction procedure is most complicated.

Hereon, the word signal is always used signifying prompt D^0 mesons, except in those cases where specified differently.

3.1 Decay Geometry

The negative kaon and positive pion the D^0 decays into leave two curled paths across ALICE trackers which is customary to characterise according to so-called topological variables. A schematisation of a D^0 decay is provided in figure 3.1.

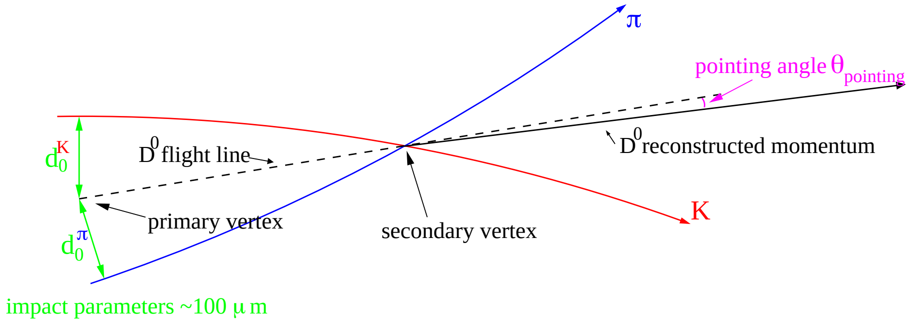

Figure 3.1: $\mathrm{D}^0 \rightarrow \mathrm{K}^- + \pi^+$ decay geometry. Topological variables pointing angle, ϑ_{pt}, and impact parameters, $\mathrm{d}_0^{\mathrm{K}}$ and d_0^{π}, are shown in the figure. Others can be built starting from vertices, D^0 reconstructed momentum, single-particle momenta and the D^0 flight line [22].

Basically, most of the lengths and angles used to classify signal and background can be built starting from the few denoted in image 3.1. All of them, it should be noted, carry a specific uncertainty which depends on the detectors spatial, temporal and energy resolutions. In general, the quantities used to perform the selection can be subdivided in single-track variables and pair variables, although in this study the latter are mainly taken into consideration. These are now described in detail, also focusing on possible correlations among them, which are one of the factors that make the optimisation procedure non-trivial.

Decay Length

The decay length is the distance between the primary and secondary vertices associated to a pair of tracks. It is the most impactful variable in the cut procedure. This is because the mean proper decay length of the D^0 is known. The signal sample will have a characteristic decay length distribution also due to its momentum dependence.

In the optimisation procedure, a quantity tightly related to the decay length is employed. This is the *normalised transverse decay length*:[4]

$$\mathbb{L}_{xy} = \frac{\mathrm{L}_{xy}}{\sigma_{xy}}. \tag{3.1}$$

The normalised decay length is the transverse projection of the decay length divided by its uncertainty. Thus, it is the inverse of the relative uncertainty of the transverse decay length. For such reason, on average, it is expected to have a smaller value in the case of the background. This is because the latter mostly consists of low-p_T primary tracks and the spatial resolution of ALICE ITS deteriorates at such transverse momenta due to multiple scattering.

An instance of the normalised decay length signal and background distributions is reported in image 3.2:

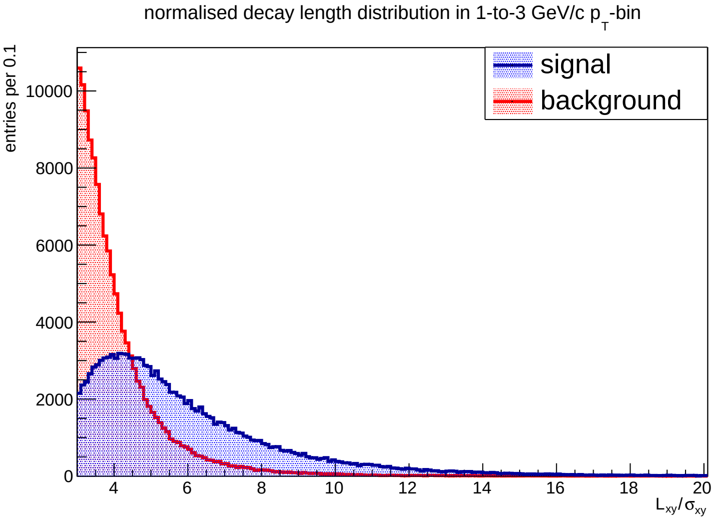

Figure 3.2: MC signal and actual data background normalised transverse decay length distributions for $1 < \frac{p_{\mathrm{T}}}{\mathrm{GeV}/c} < 3$.

Evidently, considering only those candidates with $\mathbb{L}_{xy}$ larger than a positive value leads to a larger reduction in background than in signal, which is the main goal of implementing cuts.

Cosine of Pointing Angle

The pointing angle geometrical construction is quite clear in image 3.1. By measuring the daughters momenta, one can vectorially reconstruct the D^0 line of flight. This is then compared with the direction extracted joining the primary and secondary vertices. The angular discrepancy between these two directions is the pointing angle, ϑ_{pt}.

---

[4] Hereon called normalised decay length.

Once again, in the assumption that the background consist chiefly of primary tracks, several candidates belonging to such category can be discarded by noting that the angle between the constructed lines will be on average wider if they do not have common origin. In other words, the secondary vertex found by using two unrelated tracks will be unphysical, just as the vectorial sum of their momenta. On the other hand, the two lines are supposed to coincide if they both pertain to the same process, so that the signal candidates should have a close-to-zero pointing angle, that is, a quasi-unitary cosine.

The *pointing angle cosine* distributions for signal and background are shown in figure 3.3.

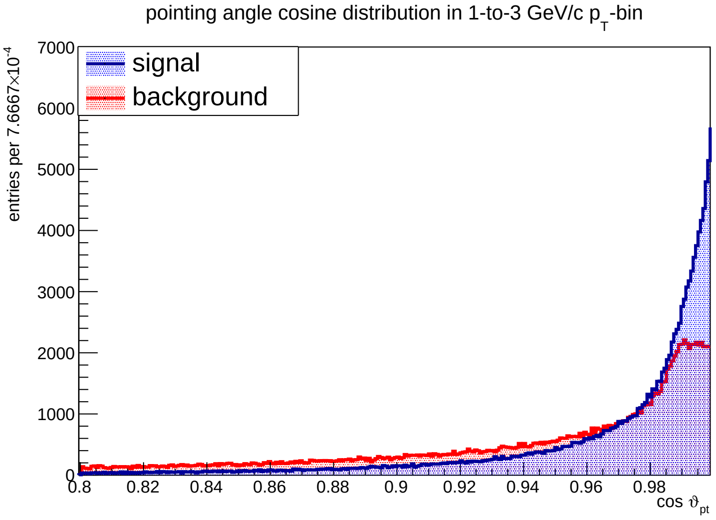

Figure 3.3: MC signal and actual data background cosine of pointing angle distributions for $1 < \frac{p_{\mathrm{T}}}{\mathrm{GeV}/c} < 3$.

In this case, similarly to the decay length, the cut applied on $\cos\vartheta_{\mathrm{pt}}$ should define a lower bound, below which it is apparent that mostly background candidates would be rejected.

Besides the cosine of the pointing angle, the cosine of the angle formed by the transverse projections of the two D^0 lines of flight is also considered (primary to secondary and sum of momenta). This quantity is denoted $\cos\vartheta_{\mathrm{pt}xy}$. In practice, a much stricter cut can be applied on it, as in the signal case the contribution to the discrepancy due to the z components of momenta is removed.

Product of Track Impact Parameters

In this context, the word "impact parameter" has a different meaning from the usual one describing the centrality of a nuclear reaction. As shown in figure 3.1, the track impact parameters are the distances between the prolongations of the tracks towards the primary vertex and the D^0 flight line taken neglecting the magnetic-field-induced curvature. The average impact parameter for pions and kaons coming from the decay of a D^0 can be shown to be about 100 μm [23]. This can be seen in figure 3.4. It means that the spatial resolution must be of the order ~ 10 μm to resolve primary and secondary tracks and the corresponding vertices.

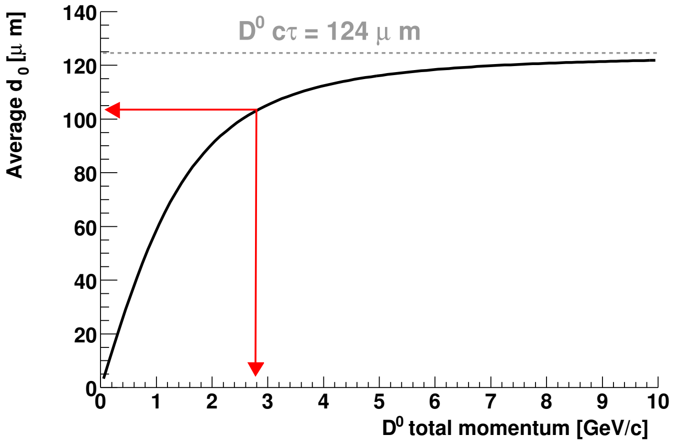

Figure 3.4: Average single-track impact parameter as a function of D^0 momentum [23].

The *product of impact parameters* is an important track pair variable. Ideally, in the event of two tracks originating at common point, its value is constrained to be negative, taking the primary vertex as a symbolic origin and assigning opposite signs to these distances when they lie on both of its sides. Background candidates, in general, will not fulfil this property. It makes thus sense to discard candidates whose $d_0^K \times d_0^\pi$ is larger than a properly selected negative value. The distribution of the product of impact parameters in the relevant negative range is reported in figure 3.5.

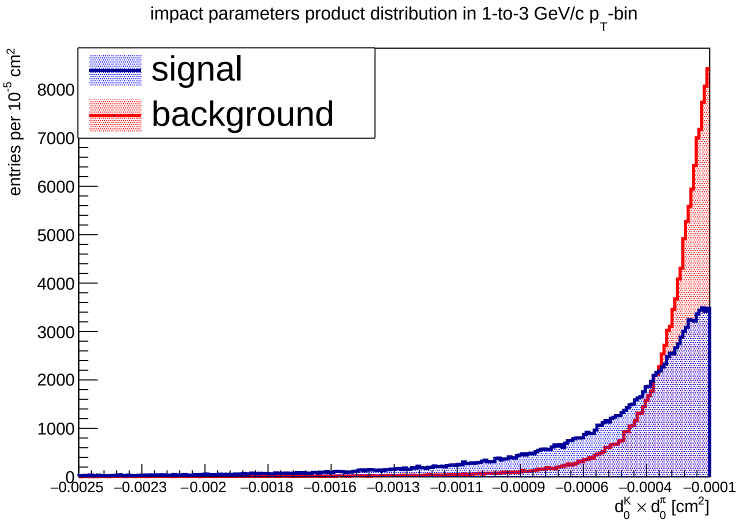

Figure 3.5: MC signal and actual data background product of impact parameters distributions for $1 < \frac{p_T}{\mathrm{GeV}/c} < 3$.

The signal and background distributions cross approximately at -4×10^{-4} cm^2. As will be seen, this is the largest value selected as cut in the analysis of low-p_{T} bins: $(1.0, 1.5), (1.5, 2.0), (2.0, 2.5), (2.5, 3.0)$ GeV/c, which is one among the main tasks carried out in the context of this thesis work.

Distance of Closest Approach

The *distance of closest approach* is the minimum distance between the daughters helical paths. In fact, despite stemming from the decay of a single object, the tracks left through detectors by the pion and kaons (for the D^0) cannot empirically coincide at any point along the mother line of flight. This is due to the finite spatial resolution of the trackers. On the other hand, they are characterised by values close to zero for such quantity. This does not hold for the background candidates, which is why a cut on the *dca* is included in the present analysis. The way signal and background are distributed with respect to such quantity is shown in figure 3.6

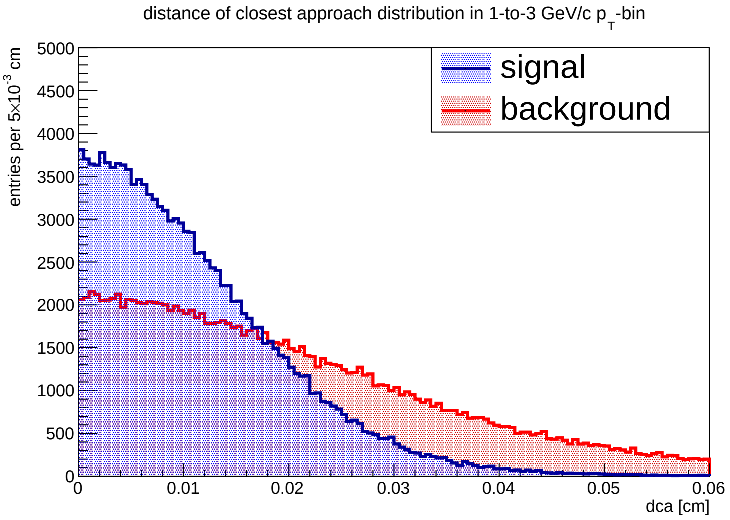

Figure 3.6: MC signal and actual data background distance of closest approach distributions for $1 < \frac{p_{\mathrm{T}}}{\mathrm{GeV}/c} < 3$.

The dismissal of background candidates takes place by cutting those whose value of the distance of closest approach lies increasingly beyond a fixed bound.

Given the described quantities, an n-dimensional hyperspace can be built by considering the ranges spanned by each of them. Each candidate will thus occupy a given point (a bin) in it. As will be seen, the discussed quantities are correlated as background-signal classifiers. Moreover, candidates often lie in regions of the hyperspace such that their nature is not clear-cut. This is of course expected, given the hugeness of the heavy ion collisions combinatorial background. It is therefore necessary to select accurately the set of cuts that will conduce to the signal extraction. In the next subsections the concept of statistical significance will be introduced as the key ingredient in the performance of such analysis.

Further Topological Variables

The main topological variables considered in the optimisation of signal extraction have been described in the previous subsections. However, some other geometrical quantities are used in such procedure. Less attention is paid to them in the context of this thesis as their optimal cut values were not studied. The reason for such choice lies either in the fact that they have lower classification power or in the fact that they have already been studied thoroughly [24].[5] These further topological variables are:

- The cosine of the decay angle, $\cos\vartheta^*$;

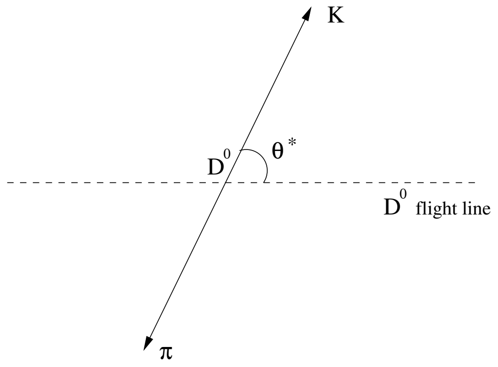

Figure 3.7: Geometrical representation of D^0 decay in the centre of mass frame of reference. The decay angle is defined as the angle between the flight lines of the D^0 and one of its daughters in such frame.

The decay angle is defined as the angle between the flight lines of the D^0 and one of its daughters (usually the kaon) in the D^0 rest frame (see image 3.7). From the isotropy in solid angle in such frame, it stems that $\cos\vartheta^*$ is distributed isotropically for the signal, too:

$$\frac{\mathrm{dN}}{\mathrm{d}\Omega} = \frac{\mathrm{dN}}{\mathrm{d}\phi^*\mathrm{d}\cos\vartheta^*} = k; \tag{3.2}$$

$$\frac{\mathrm{dN}}{\mathrm{d}\cos\vartheta^*} = 2\pi k. \tag{3.3}$$

On the other hand, background candidates, having different origins, will not be thus distributed. A cut can therefore be selected for this quantity as well based on the

---

[5] In the latter case, a lower statistical correlation between these variables and the ones considered in this study is a necessary condition to set the previously found cut values.

observed distributions. These are reported in figure 3.8. The signal $\cos\vartheta^*$ probability density is suppressed at both ends, i.e., $\cos\vartheta^* = \pm 1$, because of preliminary cuts at reconstruction stage and the following kinematical effect: when the decay angle is close to $\pm\pi$ in the rest frame, then the other daughter is likely to go out of the detector acceptance due to momentum conservation.

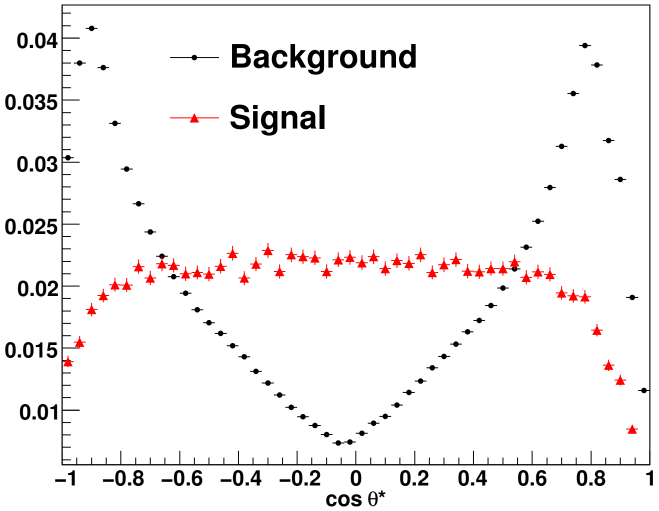

Figure 3.8: Integral (entire momentum range is considered) decay angle cosine distributions for background (black circles) and signal (red triangles) candidates. The different error bar sizes are due to the smaller number of signal than background candidates [23].

- The transverse momenta of the daughters, $p_{\mathrm{T}}^{\mathrm{K}}$ and p_{T}^{π};
  Background particles, as remarked, are softer than the D^0 daughters. This fact suggests cutting low values of transverse momentum ($p_{\mathrm{T}} \sim 0.5$ GeV/c) can lead towards higher purity.
- The single-track impact parameters of the daughters, $\mathrm{d}_0^{\mathrm{K}}$ and d_0^{π};
  It is reasonable to assume that, given the finiteness of the decay length, the absolute values of this quantities should lie within a certain upper bound. Such limit is usually chosen to be about one tenth of a centimetre.

3.1.1 Prompt and Feed-Down Mesons

D^0 mesons can be produced via direct hadronisation or stem from decay of B mesons. The latter are usually called feed-down particles (FD). Throughout this thesis work, the focus is aimed at obtaining evidence on the interaction between charm quarks and the quark-gluon plasma. Hence, the D^0's coming from B decays are not of interest. It is thus essential to to devise ways to quantify the relative abundance of prompt mesons, in particular keeping it above a given threshold in order to maximise the significance of the prompt signal.

The fraction of prompt D^0 meson out of the total observed raw signal, $\mathrm{N}_{\text{raw;TOT}}$, can be estimated using the proposed formula:

$$f_{\text{prompt}} = 1 - \frac{\mathrm{N}_{\text{raw;FD}}}{\mathrm{N}_{\text{raw;TOT}}}; \tag{3.4}$$

$$\mathrm{N}_{\text{raw;FD}} = \langle T_{AA} \rangle \times 2 \times \left. \frac{\mathrm{d}^2\sigma^{\mathrm{FD}}}{\mathrm{d}p_{\mathrm{T}}\mathrm{d}y} \right|_{\text{pQCD}}^{\text{FONLL}} \times R_{AA;\mathrm{FD}} \times \varepsilon_{\mathrm{FD}} \times b_r \times \Delta y \times \Delta p_{\mathrm{T}} \times \mathrm{N}_{\text{events}}. \tag{3.5}$$

where the doubly differential feed-down production cross-section (from the FONLL perturbative QCD calculation [25, 26]) and the feed-down nuclear modification factor appear; $\varepsilon_{\mathrm{FD}}$ is the total efficiency obtained combining intrinsic efficiency and acceptance, b_r is the branching ratio of the concerned decay channel, Δy and Δp_{T} are the considered rapidity and transverse momentum intervals and $\mathrm{N}_{\text{events}}$ is the number of lead-lead collisions of the dataset. The factor 2 is included to correct for the FONLL cross section for the $\bar{\mathrm{D}}^0$, included in this analysis.[6] The transverse momentum dependence is omitted in various factors for the sake of simplicity.

This expression has been used to evaluate the prompt fractions characterising the samples corresponding to various transverse momentum intervals. It is made use of in the calculation of the nuclear modification factor, too, as will be seen. On the other hand, working with the signal MC sample to optimise cuts, an approximate "anchoring" procedure has been employed to scale the fictitious abundance ratios provided by event generators in the low-p_{T} range involved in this work, exploiting the fractions already obtained in higher p_{T}-bins. More details in this regard will be presented when discussing the optimisation stage.

In the following, a powerful cut variable as far as the control of the dataset prompt fraction is concerned is introduced, the so-called *topomatic*.

The Topomatic

Single track impact parameters can be directly measured, but also reconstructed using simple trigonometry:

$$\mathrm{d}_0 = \mathrm{L} \sin \alpha. \tag{3.6}$$

As shown in figure 3.9, L is the distance between the primary and secondary vertices and α the angle comprised between the track prolongation and the D^0 line of flight in the lab-frame. Since both quantities are measurable, d_0 can be estimated through the proposed expression.

---

[6] In the chemical potential conditions characterising LHC lead-lead collisions, the net baryonic number is expected to be zero, which implies same production yields for D^0 and $\bar{\mathrm{D}}^0$ mesons.

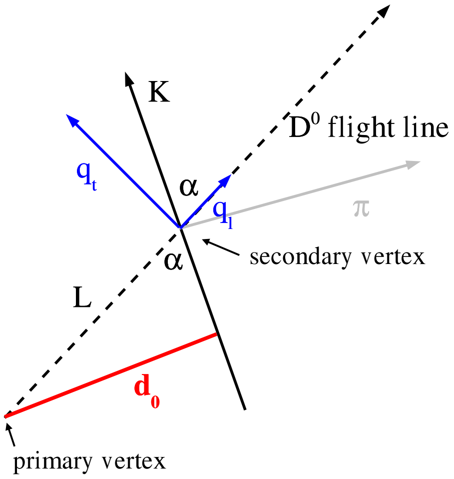

Figure 3.9: Schematic view of a D^0 decay in the kaon-pion channel in the detector frame of reference. q_l and q_t are the momentum projections along the D^0 flight line and in the plane transverse to it [23].

Considering the discrepancy between the measured and reconstructed impact parameters is a way to achieve partial separation between prompt and feed-down D^0 mesons. This is basically how the topomatic is defined for a single track (usually, in units of its own uncertainty):

$$\mathcal{T} = |d_0 - d_0^{\mathrm{exp}}|. \tag{3.7}$$

As a matter of fact, feed-down charmed meson involve a two-fold decay chain, as can be seen in figure 3.10 (for the D^0 charge conjugate). The discrepancy will therefore be larger on average, so that selecting candidates for which both tracks have $\mathcal{T}$ below an upper bound generally enhances the prompt fraction of the retained sample of signal.

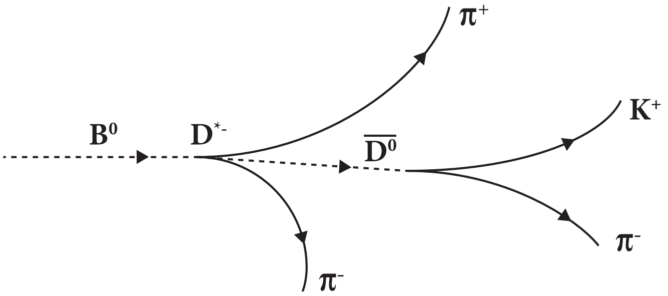

Figure 3.10: A feed-down $\bar{D}^0$ stemming from a B^0 decay chain [27].

The MC distribution of prompt and feed-down mesons along with the actual data background are reported in figure 3.11. While the significance would not largely benefit from a cut in the topomatic (background and prompt objects are similarly distributed), the usefulness of an upper cut to distinguish prompt and FD mesons is apparent.

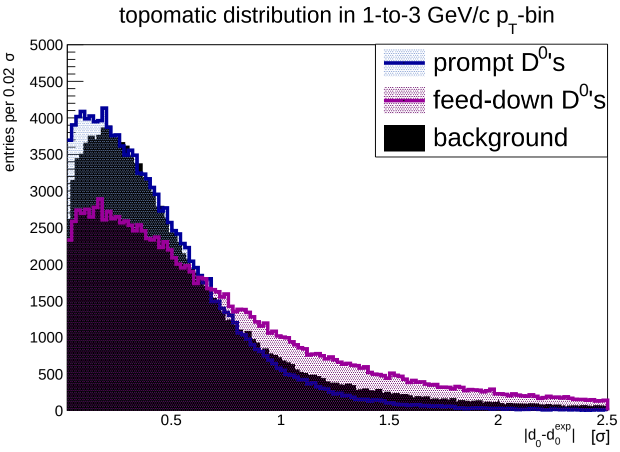

Figure 3.11: MC prompt and feed-down D^0's and actual data background topomatic distributions for $1 < \frac{p_T}{\mathrm{GeV}/c} < 3$. The topomatic is measured in units of its uncertainty, σ.

3.1.2 Correlations

Topological variables are correlated with each other. Linear correlation matrices obtained for signal and background are now presented. The meaning of each possible correlation among a pair of variables is discussed next.

The signal and background linear correlation matrices are reported in figure 3.12.

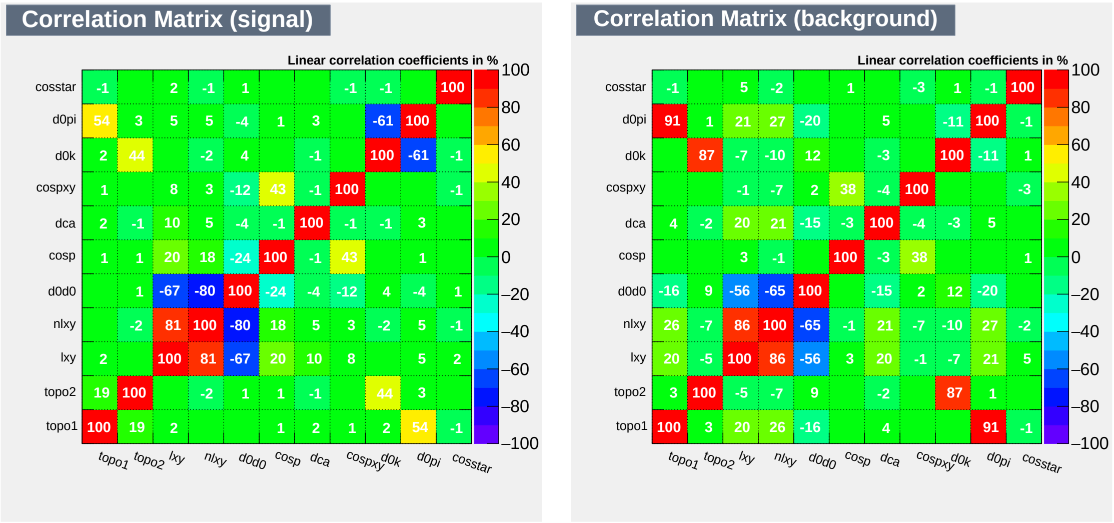
Correlation Matrix (signal)

Linear correlation coefficients in %

	topo1	topo2	lxy	nlxy	d0d0	cosp	dca	cospxy	d0k	d0pi	cosstar
cosstar	-1		2	-1	1			-1	-1		100
d0pi	54	3	5	5	-4	1	3		-61	100	
d0k	2	44		-2	4		-1		100	-61	-1
cospxy	1		8	3	-12	43	-1	100			-1
dca	2	-1	10	5	-4	-1	100	-1	-1	3	
cosp	1	1	20	18	-24	100	-1	43		1	
d0d0		1	-67	-80	100	-24	-4	-12	4	-4	1
nlxy		-2	81	100	-80	18	5	3	-2	5	-1
lxy	2		100	81	-67	20	10	8		5	2
topo2	19	100		-2	1	1	-1		44	3	
topo1	100	19	2			1	2	1	2	54	-1

Correlation Matrix (background)

Linear correlation coefficients in %

	topo1	topo2	lxy	nlxy	d0d0	cosp	dca	cospxy	d0k	d0pi	cosstar
cosstar	-1		5	-2		1		-3	1	-1	100
d0pi	91	1	21	27	-20		5		-11	100	-1
d0k		87	-7	-10	12		-3		100	-11	1
cospxy			-1	-7	2	38	-4	100			-3
dca	4	-2	20	21	-15	-3	100	-4	-3	5	
cosp			3	-1		100	-3	38			1
d0d0	-16	9	-56	-65	100		-15	2	12	-20	
nlxy	26	-7	86	100	-65	-1	21	-7	-10	27	-2
lxy	20	-5	100	86	-56	3	20	-1	-7	21	5
topo2	3	100	-5	-7	9		-2		87	1	
topo1	100	3	20	26	-16		4			91	-1

(a) *Signal correlation matrix.*

(b) *Background correlation matrix.*

Figure 3.12: Data samples correlation matrices. The name assigned to variables are abbreviations/variations of the usual ones. "topo1" and "topo2" respectively indicate the kaon and the pion tracks topomatics.

The discussion proceeds considering one by one the variables as arranged vertically (rows), and their degree of correlation with the column variables arranged horizontally until the antidiagonal value (an antisymmetrical arrangement is here preferred to the common symmetrical definition of the correlation matrix) is reached, so as to cover all possible pairs. Obviously, the elements of the antidiagonal show full linear correlation given that pairs comprising the same variable twice are considered in such instances.

The cosine of the decay angle does not show any important correlation in the signal case, nor does it for the background. Considering its definition as a particle rest frame quantity, this fact appears reasonable. In fact, all the remaining topological variables are defined and measured in the lab frame. For this reason, although such quantities as the single track impact parameter corresponding to the kaon (given the choice for the decay angle) and this angle are to show some degree of correlation when considered in the same frame, not even for the signal a simple correlation is expected.

The single track impact parameters are both correlated with the corresponding particle topomatic. This is the case for both the signal and the background. However, the correlation is quite considerable in the latter instance. A possible explanation lies partly in the shape of the prompt D^0 and background spectra shown previously in image 3.11. The prompt spectrum does not decay as fast as the background's when approaching zero, meaning that regardless of the magnitude of the impact parameter (which is not necessarily small for actual candidates having a momentum dependence) more candidates show a small value for such quantity. On the other hand, the background topomatic could be more strongly influenced by the value of the corresponding impact parameter, especially in those cases where the track is initially parallel to the flight line, leading to a very small reconstructed impact parameter.

The variable $\cos\vartheta_{\mathrm{pt}xy}$ has a soft correlation coefficient with the cosine of the pointing angle. This is expected for both prompt D^0's and background, although the actual relationship is far from linear.

The distance of closest approach is mildly linked to the decay length(s) in the two cases, too. Of course, being that larger lengths imply larger dca's for a fixed track configuration, such effect is acceptable. On the other hand, other aspects influence the value of the dca, thus leading to a low degree of correlation.

The signal pointing angle cosine is weakly anticorrelated with the product of impact parameters, meaning that using a linear approximation to relate the two quantities the cosine should grow for tracks with lower and lower products. This picture is fine for the signal, of course. The background, instead, does not show any particular behaviour.

Conclusively, the somewhat strong anticorrelation between the decay length and $\mathrm{d}_0^{\mathrm{K}} \times \mathrm{d}_0^{\pi}$ is again explained considering both the argument of the previous case and the fact that impact parameters are mildly correlated with the decay length, that is, they grow as it increases. This effect is reasonably stronger for the signal but shows in the background instance, too.

The strong correlation between decay length and its normalised counterpart is trivial in any case and thus will not be discussed.

3.2 Significance Constrained Maximisation

In view of the previous discussion concerning correlations, it appears evident that a reasonable criterion must be used to optimise the set of cuts. Such criterion is the maximisation of the statistical significance. The significance of a signal is defined for a data sample including both background and signal. Basically, it is a function of the raw yield (i.e., the yield extracted after the selection procedure and the following background subtraction), S, and the background, B, both evaluated in the region of interest.[7] In particular, it is defined as follows:

$$\mathcal{S} = \frac{\mathrm{S}}{\sqrt{\mathrm{S}+\mathrm{B}}}. \tag{3.8}$$

As the reciprocal of the relative uncertainty on the raw yield, S,[8] the significance can be maximised to achieve the minimisation of the latter.

The maximisation procedure can be carried out by sifting a set of cuts on the sample, gradually excluding those that lead to lower significances. The higher the resolution of this procedure, the more likely an optimal configuration is to be found. In this context, the resolution is tightly tied with the number of values probed in a fixed interval for each cut variable. While in principle all possible configurations could be probed, in practice the achievability of this task strongly depends on the computational power of the machine used.

3.2.1 Signal and Background Samples Usage

In this thesis work, the significance optimisation has been performed by employing a Monte Carlo sample of the signal and the actual data sidebands in order to extract the background yield in the ROI. This is because, as mentioned in this chapter introduction, a background fluctuation in the signal region is possible when working with experimental data, resulting in a compromised optimisation procedure. The signal is produced through event generators and a model of the detector geometry. The background, instead, is extracted by taking advantage of the data sidebands, i.e., the invariant mass spectrum out of the region of interest. Such procedure has been carried out for the various p_{T}-bins. In figure 3.13 an instance of signal and background samples and the relative fit curves used to compute the yields is proposed.[9] The gaussian of figure 3.13 a) aimed at reproducing

---

[7] The region of interest (ROI) is usually set equal to the $\pm 3\sigma$ interval around the mass of the concerned particle.

[8] It can be shown using well-known uncertainty propagation laws that starting from: $\mathrm{S} = \mathrm{yield}^{\mathrm{tot}}_{\mathrm{ROI}} - \mathrm{B}$, $u(\mathrm{S}) = \sqrt{\mathrm{S}+\mathrm{B}} = \mathrm{S}/\mathcal{S}$ is obtained.

[9] Actually, the fit function is used in the yield extraction only in the background case. For the signal, the entries in the ROI range are more simply counted.

the signal shape is defined in a region that excludes both of its tails. These, in fact, show non-gaussian behaviour for at least two reasons: firstly, the different momentum resolutions characterising the daughter tracks (having different momenta); secondly, the fact that it is not the transverse momentum as an experimental quantity to be distributed normally; rather, its reciprocal. This is why the inverse-momentum resolution shown in figure 2.5 is defined. It should also be noted that although the fit curve does not appear in the ROI of figure 3.13 b), it is the yield stemming from this function in the corresponding range that is used. The choice of not showing it is due to the fact that the fit is performed ignoring such range.

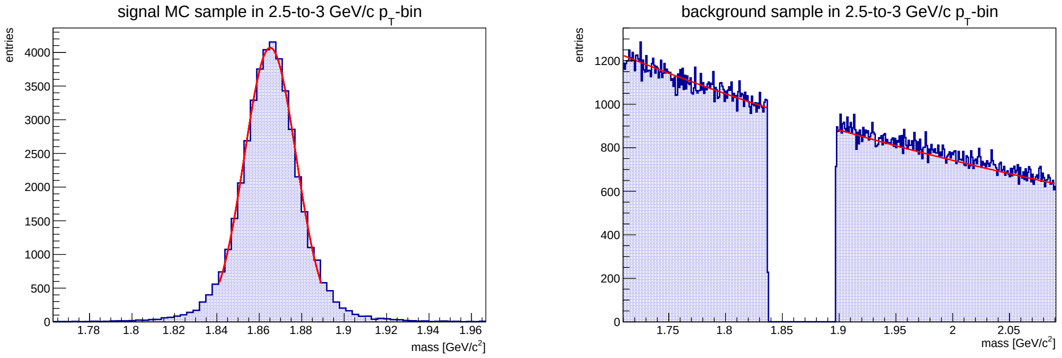

(a) *Signal MC sample.*

(b) *Background sidebands experimental data sample.*

Figure 3.13: MC signal and data background sidebands in $2.5 < \frac{p_{\mathrm{T}}}{\mathrm{GeV}/c} < 3$. Fit curves are shown in red for the two distributions.

Since the lead-lead collisions (events) leading to the two samples are different, the values of signal and background raw yields have been normalised by considering their ratio with the numbers of events. For this reason the significance is evaluated in arbitrary units.

3.2.2 Prompt Fraction Estimate

The fraction of prompt D^0 mesons should be kept as high as possible in the process of cut optimisation. More particularly, a lower bound on its value should be set to ensure maximisation of prompt significance:

$$f_{\mathrm{prompt}} = \frac{\mathrm{N}_{\mathrm{raw;PR}}}{\mathrm{N}_{\mathrm{raw;TOT}}} \gtrsim 0.8. \tag{3.9}$$

As already mentioned, the relative abundance of prompt and feed-down mesons is enhanced in favour of the latter in the MC production, thus leading to suppressed values of the prompt fraction. Therefore, to the end of fulfilling the above condition, the MC prompt fraction must first be re-scaled. For the four transverse momentum intervals primarily considered in this work, an “anchoring” strategy has been used, taking advantage of the fact that f_{prompt} values obtained for the same bins of the MC samples were available, although for cuts not necessarily equal to those selected as optimum.

Anchoring

If the MC production retained the correct relative prompt and feed-down abundances, then, once the selection were carried out, the value of the prompt fraction in a given p_{T}-bin could be expressed as:

$$f_{\text{prompt}} = \frac{\mathrm{N}_{\text{raw;PR}}}{\mathrm{N}_{\text{raw;PR}} + \mathrm{N}_{\text{raw;FD}}} = \frac{\epsilon_{\mathrm{PR}}\mathrm{N}_{\mathrm{PR}}}{\epsilon_{\mathrm{PR}}\mathrm{N}_{\mathrm{PR}} + \epsilon_{\mathrm{FD}}\mathrm{N}_{\mathrm{FD}}}, \tag{3.10}$$

where ϵ represents the cut efficiency for either prompt or feed-down mesons.[10] On the other hand, a fictitious enhancement and/or suppression can be described introducing some factors (k_{PR} and k_{FD}) in the expression:

$$f'_{\text{prompt}} = \frac{\mathrm{N}'_{\text{raw;PR}}}{\mathrm{N}'_{\text{raw;PR}} + \mathrm{N}'_{\text{raw;FD}}} = \frac{\epsilon_{\mathrm{PR}}k_{\mathrm{PR}}\mathrm{N}_{\mathrm{PR}}}{\epsilon_{\mathrm{PR}}k_{\mathrm{PR}}\mathrm{N}_{\mathrm{PR}} + \epsilon_{\mathrm{FD}}k_{\mathrm{FD}}\mathrm{N}_{\mathrm{FD}}}. \tag{3.11}$$

A system can thus be built with the aim of extracting the enhancement/suppression factors k_{PR} and k_{FD}:

$$\begin{cases} \frac{1}{f_{\text{prompt}}} & = 1 + a \\ \frac{1}{f'_{\text{prompt}}} & = 1 + a\frac{k_{\mathrm{FD}}}{k_{\mathrm{PR}}} \end{cases}, \tag{3.12}$$

where $a = \epsilon_{\mathrm{FD}}\mathrm{N}_{\mathrm{FD}}/\epsilon_{\mathrm{PR}}\mathrm{N}_{\mathrm{PR}}$. Here, the ratio a can be extracted as follows:

$$a = \frac{1}{f_{\text{prompt}}} - 1. \tag{3.13}$$

In fact, the correct value of the prompt fraction in the interested bin, f_{prompt}, is known for certain cuts. These are the same for which the value of the fictitious prompt fraction is to be extracted,[11] then leading to an estimate of the p_{T}- and cut-independent k factors ratio (which is enough in the present case, as the charm production is not enhanced):

$$\frac{k_{\mathrm{FD}}}{k_{\mathrm{PR}}} = \frac{1}{a}\left(\frac{1}{f'_{\text{prompt}}} - 1\right). \tag{3.14}$$

In turn, that is finally used to re-scale the fictitious prompt fraction when working with different cuts by employing:

$$\hat{f}_{\text{prompt}} = \left[\frac{1}{\hat{f}'_{\text{prompt}}} - \hat{a}\left(\frac{k_{\mathrm{FD}}}{k_{\mathrm{PR}}} - 1\right)\right]^{-1}, \tag{3.15}$$

which is equivalent to:

$$\hat{f}_{\text{prompt}} = \left[1 + \frac{k_{\mathrm{PR}}}{k_{\mathrm{FD}}}\left(\frac{1}{\hat{f}'_{\text{prompt}}} - 1\right)\right]^{-1}. \tag{3.16}$$

where the hat denotes that a different cut from the one used for anchoring is being considered.

---

[10] The cut efficiency is the fraction of candidates of a certain species retained after cutting on the topological variables.

[11] Hence the name anchoring for this procedure.

It should be noted that in order to obtain the k factors separately, a similar procedure considering some other cuts is to be conducted. As remarked, this was not necessary in the present case as no enhancement or suppression is implemented for charm production.

It should also be explained in more detail why an anchoring procedure is necessary in the first place, considering that information on the MC production is available. The explanation is the following: the enhancement of beauty production has a well-defined dependence on the momentum. It is not possible to extrapolate a fixed enhancement on the production of B meson. Therefore, the quantity extracted serves as an average scaling factor, in order to keep track of the prompt fraction, thus constraining the optimisation of cuts.

The enhancement ratios found for the studied four low transverse momentum bins are reported in table 3.1.

p_{T}-bin (GeV/c)	$k_{\mathrm{FD}}/k_{\mathrm{PR}}$
(1.0, 1.5)	9.7011
(1.5, 2.0)	8.1395
(2.0, 2.5)	8.6231
(2.5, 3.0)	8.1488

Table 3.1: Feed-down to prompt enhancement ratios obtained for the considered four low-p_{T} bins in range $1 < \frac{p_{\mathrm{T}}}{\mathrm{GeV}/c} < 3$.

3.2.3 Optimal Cuts Extraction. Results

The cut optimisation has been carried out following the proposed scheme for each different p_{T}-bin:

- Topological variables, intervals and steps setting;
  The variables involved in this analysis have already been described. They are the following: normalised decay length, cosine of pointing angle, product of impact parameters, distance of closest approach and topomatic. The pointing angle projection cosine has been considered separately, due to its low correlation with the other variables.[12] For each variable a range of possible bounds must be chosen. This is done by considering the various distributions in the corresponding bins, setting the extreme values of the interval so that the best cut in the single variable case is obtained. The step throughout such intervals is chosen so as to obtain the total

---

[12] The only exception is the cosine of the pointing angle it stems from. However, geometrical arguments assure a positive correlation between the two variable so that a lower-bound cut on the value of either one will reject a large number of candidates that show low value for the other, too.

amplitude by multiplying it for an integer number. The smaller the step, the higher the resolution of this procedure. Thus, it has been attempted to keep it small, at the same time preventing the total computation time from exceeding a few hours.[13]

- Nested loops;
  Starting from the loosest cut a variable value is changed towards the strictest. This is repeated for all variables in such a way that every possible combination is probed, computing the resulting significance and prompt fraction. The signal raw yield is extracted in the $\pm 3\sigma$ ROI. The background raw yield is estimated by fitting the sidebands of the distribution, and then computing the integral of the best fitting function in the ROI. The best fitting function has been chosen to be a decreasing exponential, due to its suitability throughout the transverse momentum range. However, as will be seen, in the low-p_{T} range the actual data background is best fitted using polynomial functions.

- Exclusion of low-f_{prompt} cuts;
  All those cuts that lead to prompt fraction lower than 0.8 are rejected.

- Selection of maximum significance cuts among the remaining;
  The cuts fulfilling the prompt fraction constraint and showing high significance are selected. The procedure is repeated until the best configuration is found.

In figures 3.14, 3.15, 3.16 and 3.17 instances of output of the presented algorithm are shown for the four low-p_{T} bins. In all of them, two vertical axes are visible on both sides of the plot, measuring the significance and the prompt fraction. The nested loop structure is two-fold for graphical purposes: a higher number of points/variables would have hardly conveyed more information than is needed at this stage. This means that in each case two cut quantities assuming eight different values are considered, for a total of 64 points/cuts. Starting from cut index = 0, groups of eight sequential points can be seen to follow similar trends. Eight of these structures are present in each image. These two features represent the changes in the inner-loop variable and in the outer-loop variable, respectively.

---

[13] The nested loop strategy explained subsequently implies exponential growth of the number of loops that are undergone. Adding a step has as a net effect the repetition of all the other steps of the further variables.

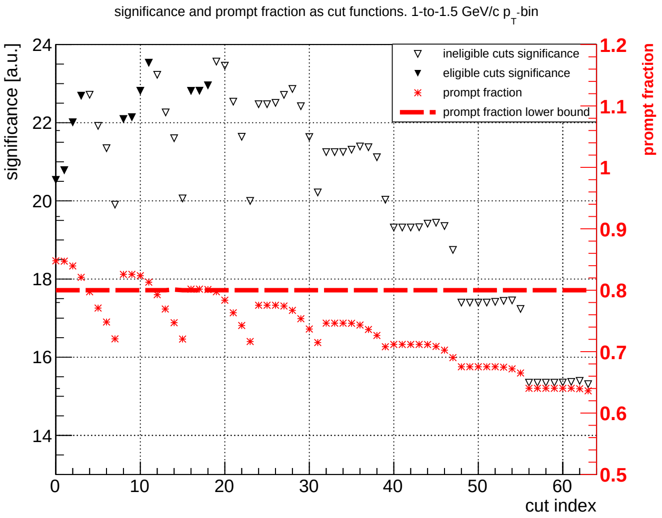

Figure 3.14: Significance and prompt fraction nested-loop evolution. Impact parameters product and decay length are the inner-loop and outer-loop variables, ranging from -1 to -8 $\times 10^{-4}$ cm^2, and from 3.5 to 7, respectively. Maximum significance is obtained for $d_0^K \times d_0^\pi < -4 \times 10^{-4}$ cm^2, and $L_{xy}/\sigma_{xy} > 4$. Only cuts leading to a value of prompt fraction larger than 0.8 are considered eligible as optimal.

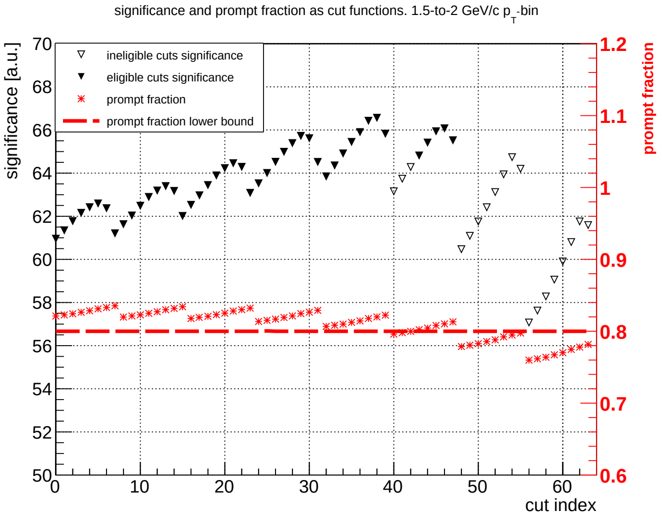

Figure 3.15: Significance and prompt fraction nested-loop evolution. Cosine of pointing angle and decay length are the inner-loop and outer-loop variables, ranging from 0.9 to 0.97, and from 3.5 to 7, respectively. Maximum significance is obtained for $\cos\vartheta_{\mathrm{pt}} > 0.96$, and $L_{xy}/\sigma_{xy} > 5.5$. Only cuts leading to a value of prompt fraction larger than 0.8 are considered eligible as optimal.

Since the two variables considered in each instance have been chosen to be different in order to give an overview of the encountered trends, these are not expected to be similar when switching from one image to the other. Among the other things, it is evident how the constraint on the prompt fraction is more and more fulfilled as the transverse momentum grows. This effect can be understood considering the resolution deterioration in such p_{T} range.

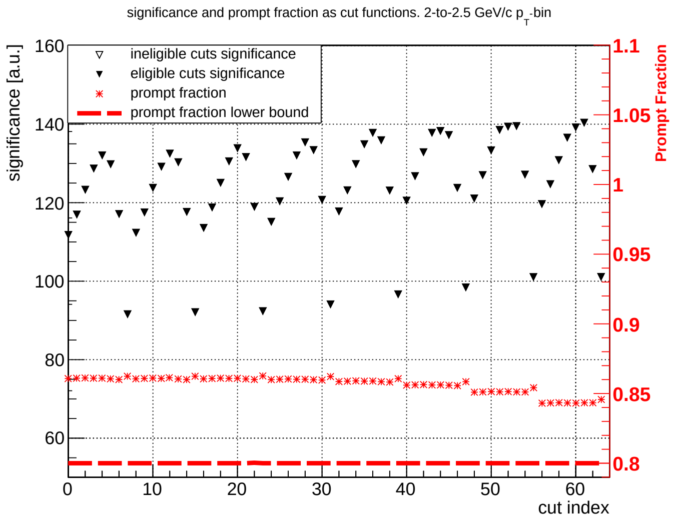

Figure 3.16: Significance and prompt fraction nested-loop evolution. Distance of closest approach and decay length are the inner-loop and outer-loop variables, ranging from 0.04 to 0.005 cm, and from 3.5 to 7, respectively. Maximum significance is obtained for *dca* < 0.015 cm, and $\mathrm{L}_{xy}/\sigma_{xy} > 7$. Only cuts leading to a value of prompt fraction larger than 0.8 are considered eligible as optimal.

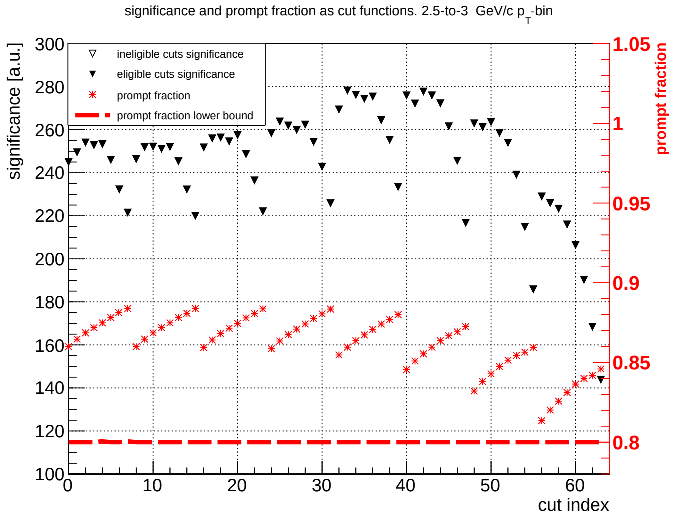

Figure 3.17: Significance and prompt fraction nested-loop evolution. Topomatics and decay length are the inner-loop and outer-loop variables, ranging from 1.1 to 0.4, and from 3 to 10, respectively. Maximum significance is obtained for $\mathcal{T} < 1$, and $\mathrm{L}_{xy}/\sigma_{xy} > 7$. Only cuts leading to a value of prompt fraction larger than 0.8 are considered eligible as optimal.

The cuts maximising significance have been extracted making use of the described procedure. They are reported subsequently in table 3.2.

$p_{\rm T}$-bin (GeV/c)	$\mathrm{L}_{xy}/\sigma_{xy} >$	$\cos\vartheta_{\rm pt} >$	$\cos\vartheta_{{\rm pt}xy} >$	$\mathrm{d}_0^{\rm K}\times\mathrm{d}_0^{\pi} <$ (cm^2)	$dca <$ (cm)	$\mathcal{T} <$ (nσ)
(1.0, 1.5)	4.0	0.91	0.966	-0.0004	0.025	0.9
(1.5, 2.0)	5.0	0.95	0.951	-0.0005	0.020	0.8
(2.0, 2.5)	6.5	0.98	0.991	-0.0005	0.020	0.8
(2.5, 3.0)	7.0	0.98	0.972	-0.0005	0.020	0.7

Table 3.2: Maximum significance topological cuts in the $1 < \frac{p_{\rm T}}{{\rm GeV}/c} < 3$. These values have been optimised in the context of this thesis work.

As remarked previously, some other variables are used to extract the signal from the experimental data. The cuts applied on such quantities are presented in table 3.3.

$p_{\rm T}$-bin (GeV/c)	$\lvert\cos\vartheta^*\rvert <$	$p_{\rm T}^{\rm K} >$ (GeV/c)	$p_{\rm T}^{\pi} >$ (GeV/c)	$\lvert\mathrm{d}_0^{\rm K}\rvert <$ (cm)	$\lvert\mathrm{d}_0^{\pi}\rvert <$ (cm)
(1.0, 1.5)	0.8	0.5	0.5	0.1	0.1
(1.5, 2.0)	0.8	0.5	0.5	0.1	0.1
(2.0, 2.5)	0.8	0.6	0.6	0.1	0.1
(2.5, 3.0)	0.8	0.6	0.6	0.1	0.1

Table 3.3: High significance topological cuts for secondary variables. These values have been optimised in the context of works other than this thesis [24].

3.2.4 Discussion on Lowest $p_{\rm T}$-bin

Transverse momentum interval (1.0, 1.5) GeV/c is undoubtedly the toughest as far as signal extraction is concerned. Such fact can be explained considering a variety of aspects. The low resolution at low $p_{\rm T}$ plays a major role, indeed. Moreover, the chief nature of combinatorial background, i.e., low-$p_{\rm T}$ primary tracks, makes the selection harder, as it jeopardises the classification effectiveness of the most impactful cut variables: first among all, the decay length. In fact, when the distance between the primary and secondary vertices is shorter, it is necessary to perform a looser cut in order to retain most of the signal. This, in turn, results in the conservation of a larger amount of background with respect to the higher transverse momentum bins. The significance in such range is thus notably lower; i.e., a factor of ∼ 3 with respect to the next bin at the analysis stage.[14] Incidentally, this is also due to the fact that in this range the constraint on the prompt fraction has a much stricter effect than it has in the other bins (see figure 3.14).

To better understand the behaviour of the significance and the prompt fraction in this interval, a detailed study has been performed for pairs of variables, among which the

---

[14] As will be seen, a factor of ∼ 3 suppression with respect to the (1.5, 2.0) GeV/c is also found when working with actual data

normalised decay length, the cosine of the pointing angle and the topomatic. The first two are the leading cut variables as far as the significance is concerned, the third is a powerful regulator of the fraction of prompt mesons. Figure 3.18 shows the dependence of significance and prompt fraction as functions of cuts on the decay length and on the cosine of the pointing angle.

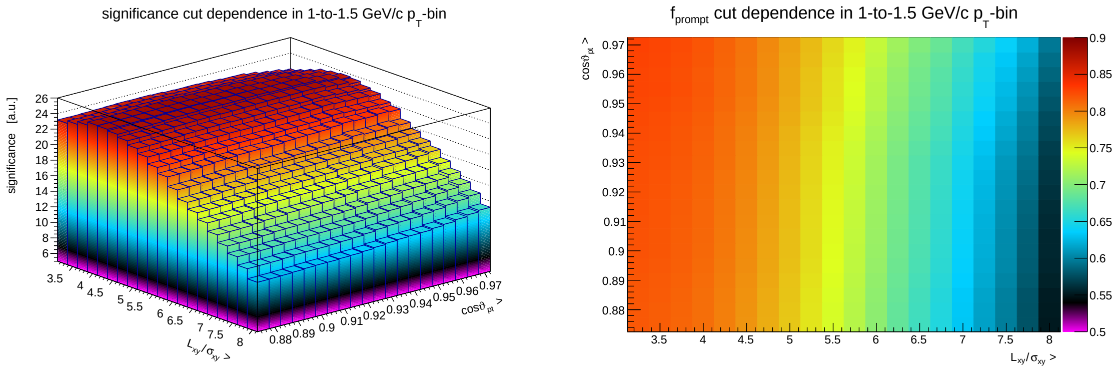

(a) *Significance 3D histogram. Cut dependence.* (b) *Prompt fraction colour map. Cut dependence.*

Figure 3.18: Significance and prompt fraction as decay length and pointing angle cosine functions.

Evidently, the decay length has a stronger influence on both quantities. In both cases, optimal values are obtained for $\mathrm{L}_{xy}/\sigma_{xy} \gtrsim 4$. However, while the significance is actually maximised thereat, the prompt fraction could be further increased by decreasing the cut value. This is not essential, however, since the constraint ($f_{\text{prompt}} \gtrsim 0.8$) is fulfilled up to $\mathrm{L}_{xy}/\sigma_{xy} \gtrsim 4.5$.

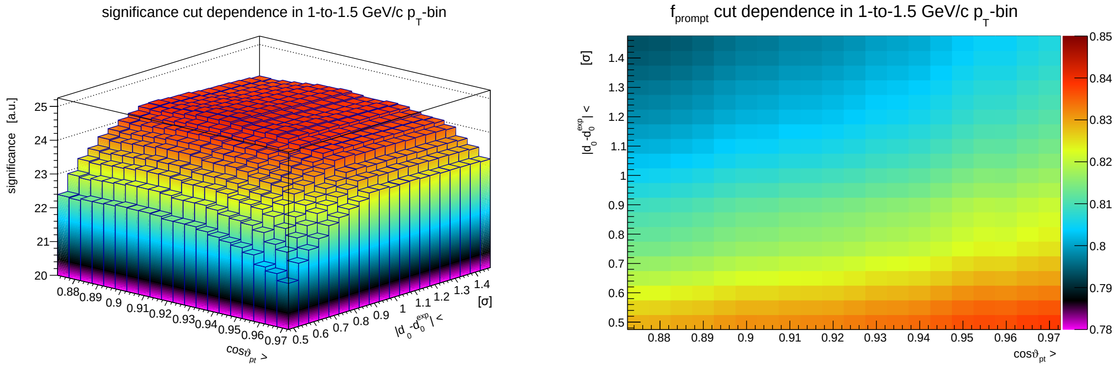

(a) *Significance 3D histogram. Cut dependence.* (b) *Prompt fraction colour map. Cut dependence.*

Figure 3.19: Significance and prompt fraction as pointing angle cosine and topomatics functions.

The same check for the topomatic and the cosine of the pointing angle is shown in figure 3.19. The maximum significance is barely visible at coordinates ($\cos\vartheta_{\text{pt}} > 0.91$, $\mathcal{T} < 0.9$). These are actually the values extracted during the optimisation analysis. In general, the peculiar behaviour of $\mathcal{S}$ in this range of momentum is apparent. In the considered cut intervals, the cosine of the pointing angle and the topomatic both seem to have low relative impact on it. This is not the case for the other bins, as can be deduced by comparing figures 3.3 and 3.11. The value of the prompt fraction, instead, besides being tightly tied to the cut on the topomatic, is also slightly influenced by $\cos\vartheta_{\mathrm{pt}}$. A strong influence of the decay length on it is thus also expected when compared to the topomatic.[15]

The significance and prompt fraction dependence as functions of the cuts on the normalised decay length and on the cosine of the pointing angle is reported in figure 3.20.

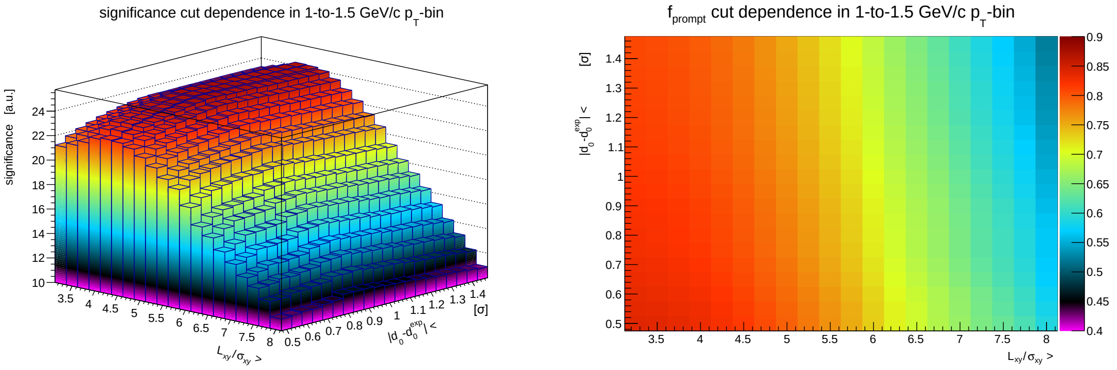

(a) *Significance 3D histogram. Cut dependence.* (b) *Prompt fraction colour map. Cut dependence.*

Figure 3.20: Significance and prompt fraction as decay length and topomatics functions.

The expectations concerning the power of the normalised decay length as a prompt fraction regulator are actually outmatched. The vertical (quasi) monochromatic stripes indicate that variations of the prompt fraction are much more strongly induced by a change in the cut on the decay length than by a change in the cut on the topomatic. It is thus chiefly important to select cautiously a cut on the former as far as the lowest p_{T}-bin analysis is concerned.

---

[15] Of course, being prompt and feed-down mesons characterised by different decay topologies, cutting on the decay length will expectedly have an impact on the prompt fraction.

Chapter 4

D^0 Production Measurement

The measurement of the production of prompt D^0 mesons in the ultra-relativistic heavy ion collisions studied by ALICE at the CERN Large Hadron Collider is a data analysis endeavour. From the discussed significance optimisation to the evaluation of the nuclear modification factor, a considerable variety of computational tools and techniques is employed. Furthermore, a few assumptions are made throughout the whole process and must be taken into account in the form of systematic uncertainties. A thorough estimation of these is essential to provide accurate information when presenting results.

In this thesis work, the production of D^0 mesons is measured from the 10% most central lead-lead collisions data collected during the $\sqrt{s_{\mathrm{NN}}} = 5.02$ TeV 2018 run, in the second period of operation of the LHC. Events (collisions) have been collected by triggering on signals coming from the V0 detector, requiring coincidence at forward and backward pseudorapidities. Only events whose primary vertex was located within $\Delta z \sim$10 cm from the origin of the coordinate system have been taken into account. Particle identification has been used in order to single out kaons and exclude pion pair tracks. In particular, the time projection chamber and the time of flight detectors, characterised by high separation power as far as these objects are concerned, have been employed. With these, each track is identified making use of the difference in resolution units (σ) between the measured signal and the expectation for the concerned species. Tracks lying out of the 3σ region are generally discarded.

To analyse this data the AliRoot analysis framework is used [28]. AliRoot is the ALICE offline framework and inherits all the classes of the Root data analysis framework. Several devoted classes specific to the analysis conducted at ALICE are implemented. Their uses involve both the MonteCarlo production and experimental data and are manifold: detector description, event generation, particle transport, reconstruction, particle identification, and generation of event summary data [29]. Figure 4.1 shows a qualitative trend of the degree of information at each processing stage when working with simulated and real data. For each MonteCarlo simulated hit, the corresponding digital output of the detector is stored as a summable digit, taking into account the detector response function. Possible noise is then added to the summable digit, which is then stored as a digit. The last step consists of the storing of the data in the specific hardware format of the detector, the raw data. The raw data, representing the response of the detector, constitutes the minimum of the physical information parabola. It is the starting point of the reconstruction process discussed in subsection 2.3.1, which is identical for both simulated and real events, and it is divided in the steps listed below (figure 4.1) [23].

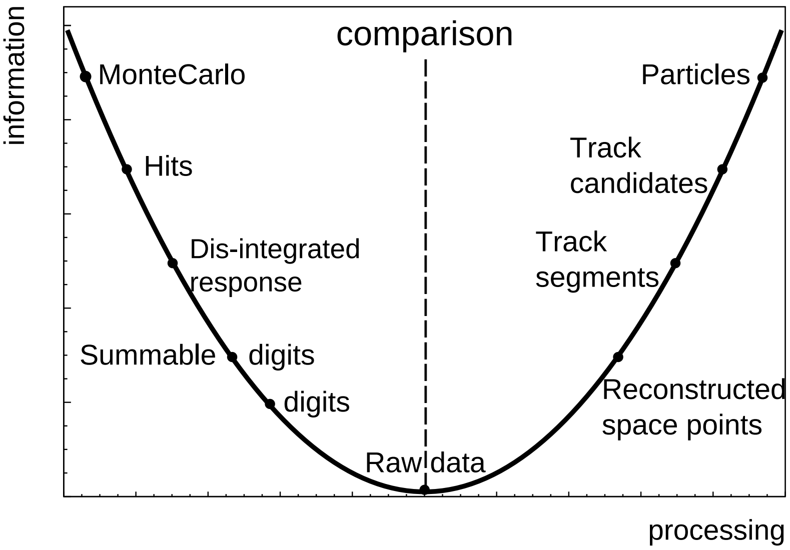

Figure 4.1: Data processing stages and the corresponding degree of information, from MonteCarlo simulations to particles species yield extraction.

The present chapter illustrates the signal extraction process, the systematic sources of uncertainties and the final analysis results. In the first part, the fit of (post-cut) signal gaussians is discussed in detail. This allows to compute the differential D^0 raw yields, which, however, are to be feed-down-subtracted. The technique used to such end is explained in the second part of the chapter. The object of the third section is the estimation of systematic uncertainties. Several assumptions are involved in the computation of raw yields, the nuclear modification factor, etc., and all of them are taken into account as sources of systematic effects. Conclusively, the transverse momentum spectrum of D^0 mesons and their nuclear modification factor are presented. The latter is broadly discussed, and compared with theoretical as well as experimental trends.

4.1 Signal Extraction

As extensively discussed in chapter 3, the optimal separation between the combinatorial background and the signal is accomplished by means of topological cuts. In such chapter, the focus has been directed on topological selection quantities, for low-p_{T} intervals. The set of cuts instead adopted in p_T-bins from 3 GeV/c to 50 GeV/c are reported in following tables 4.1 and 4.2:

p_T-bin (GeV/c)	$\mathrm{L}_{xy}/\sigma_{xy} >$	$\cos\vartheta_\mathrm{pt} >$	$\cos\vartheta_{\mathrm{pt}xy} >$	$\mathrm{d}_0^\mathrm{K} \times \mathrm{d}_0^\pi <$ (cm^2)	$dca <$ (cm)	$\mathcal{T} <$ (cm)
(3.0, 4.0)	7.0	0.92	0.997	−0.00036	0.030	1.0
(4.0, 5.0)	7.0	0.92	0.997	−0.00036	0.030	1.5
(5.0, 6.0)	6.0	0.90	0.998	−0.00023	0.030	1.5
(6.0, 7.0)	6.0	0.90	0.998	−0.00023	0.030	1.5
(7.0, 8.0)	6.0	0.90	0.998	−0.00023	0.030	1.5
(8.0, 10.0)	5.0	0.90	0.998	−0.00010	0.030	1.5
(10.0, 12.0)	5.0	0.90	0.998	−0.00010	0.030	1.5
(12.0, 16.0)	5.0	0.90	0.998	−0.00010	0.040	2.0
(16.0, 24.0)	5.0	0.90	0.995	−0.00010	0.040	2.0
(24.0, 36.0)	5.0	0.90	0.995	−0.00010	0.040	2.0
(36.0, 50.0)	5.0	0.90	0.995	−0.00010	0.040	2.0

Table 4.1: Track-pair cuts for p_T intervals between 3 and 50 GeV/c [24].

p_T-bin (GeV/c)	$\lvert\cos\vartheta^*\rvert <$	$p_\mathrm{T}^\mathrm{K} >$ (GeV/c)	$p_\mathrm{T}^\pi >$ (GeV/c)	$\lvert\mathrm{d}_0^\mathrm{K}\rvert <$ (cm)	$\lvert\mathrm{d}_0^\pi\rvert <$ (cm)
(3.0, 4.0)	0.8	0.6	0.6	0.1	0.1
(4.0, 5.0)	0.8	0.6	0.6	0.1	0.1
(5.0, 6.0)	0.8	0.7	0.7	0.1	0.1
(6.0, 7.0)	0.8	0.7	0.7	0.1	0.1
(7.0, 8.0)	0.8	0.7	0.7	0.1	0.1
(8.0, 10.0)	0.8	0.7	0.7	0.1	0.1
(10.0, 12.0)	0.8	0.7	0.7	0.1	0.1
(12.0, 16.0)	1.0	0.7	0.7	0.1	0.1
(16.0, 24.0)	1.0	0.7	0.7	0.1	0.1
(24.0, 36.0)	1.0	0.7	0.7	0.1	0.1
(36.0, 50.0)	1.0	0.7	0.7	0.1	0.1

Table 4.2: Single-track cuts for p_T intervals between 3 and 50 GeV/c [24].

On the other hand, it is reasonable to also implement a cut on the invariant mass stemming from the two daughter tracks,[1] given that the mass of the measured particle is known. This has been done, excluding all the candidates showing a discrepancy larger than 40 MeV/c^2 with the world average D^0 mass: $m_{\mathrm{D}^0} = 1864.84 \pm 0.07$ MeV/c^2 [9].

---

[1] The invariant mass of each candidate is computed as: $m(K\pi) = c^{-2}\sqrt{(\mathrm{E}_K + \mathrm{E}_\pi)^2 - (\mathrm{p}_K c + \mathrm{p}_\pi c)^2}$.

4.1.1 Invariant Mass Distributions

Once those candidates that do not fulfil the chosen cuts are excluded, invariant mass distributions characterised by a prominent peak at about the D^0 mass value are obtained.[2] These distributions are shown in figure 4.2. Remarks are due at very low and very high transverse momenta. Signal extraction in the low-p_T bins is evidently difficult, with the (1.0, 1.5) GeV/c bin barely showing any peak at first sight. This is due to the reasons explained in subsection 3.2.4. At the opposite extreme, low statistics makes the task hard as well.

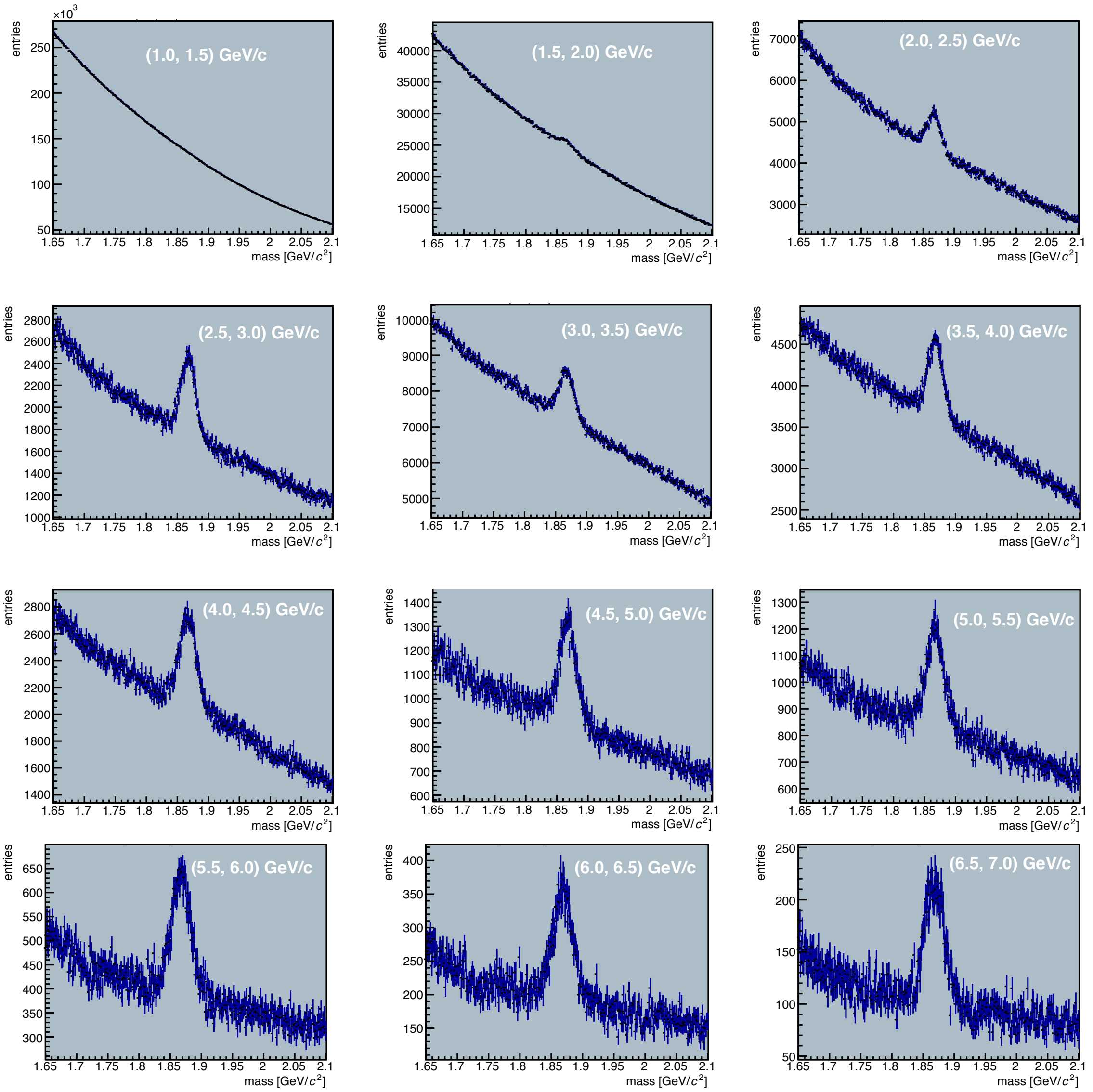

---

[2] At ALICE, the gaussian invariant mass peaks are centred around 1.867 GeV/c^2: there appears to be a source of slight deviation from the world average value, that is likely due to a small bias in the measured momentum scale.

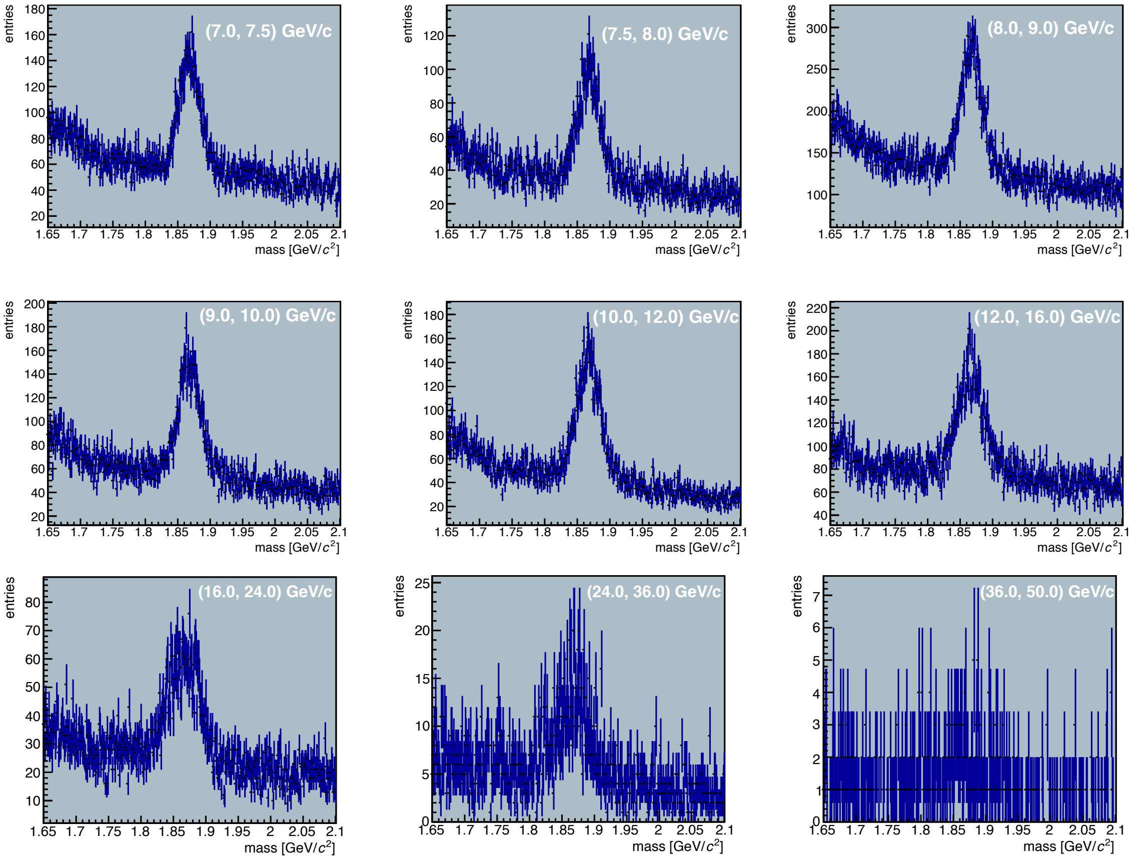

Figure 4.2: Invariant mass histograms obtained as a result of the topological selection. Lowest and highest intervals very low D^0 purity and statistics, respectively, make signal extraction more complicated in such cases.

The signal extraction is performed as follows: spectra are first rebinned (i.e, a number of contiguous bins is regrouped into one single bin) and the optimal background fitting function is assessed by considering a residual plot and the chi-squared of each fit. Then, the signal raw yield is obtained as a fit parameter to be normalised by the bin-width; the background yields are integrated within 3σ from the mean of the gaussian fit. In such way, the significance of the D^0 measurement in the concerned bin can be evaluated. The global fit function can be expressed as:

$$f(m) = f_b(m; \vec{P}_b) + f_s(m; \vec{P}_s), \tag{4.1}$$

where $f_b(m; \vec{P}_b)$ and $f_s(m; \vec{P}_s)$ represent the background and the signal fit functions of the invariant mass of the candidate, as dependent on different vectors of parameters, $\vec{P}_b$ and $\vec{P}_s$, respectively. While $f_s(m)$ is always chosen to be a gaussian function whose amplitude is factorised as its area divided by $\sqrt{2\pi}$ times its standard deviation (σ), three different cases have been studied for the background function: a decreasing exponential and second and third degree polynomials. An exponential function is suitable for all the transverse momentum range above 3 GeV/c. On the other hand, the first four bins have been fitted with polynomials after observing how these best reproduced the background shape in the signal sidebands. More specifically, the background shape in bins (1.0, 1.5) GeV/c and (1.5, 2.0) GeV/c is best described by a second degree polynomial, whereas for (2.0, 2.5) GeV/c and (2.5, 3.0) GeV/c a third degree polynomial is preferable. In figure 4.3, a representation of the fitting of the first four transverse momentum bins is provided.

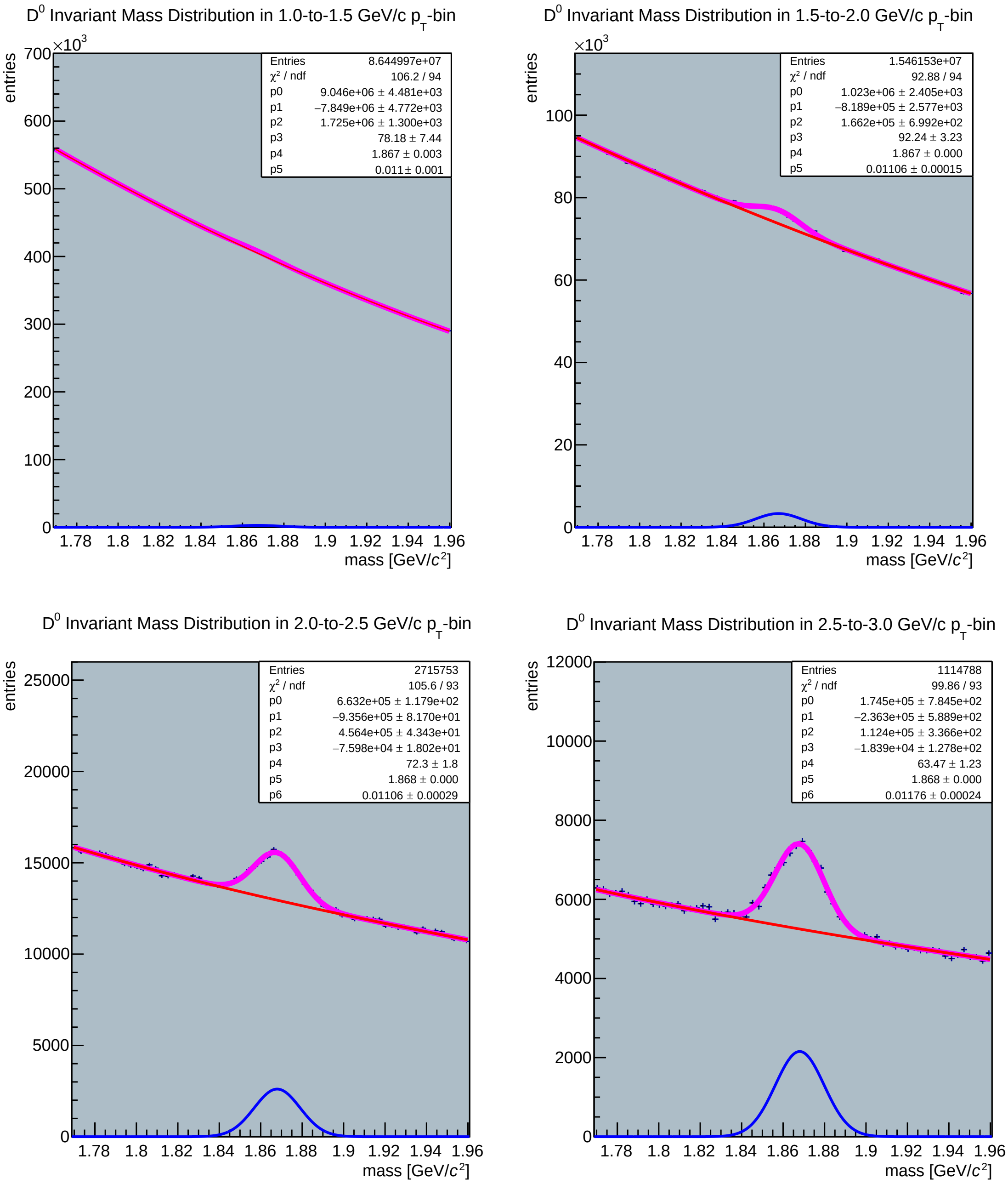

Figure 4.3: Fitting of low-p_T invariant mass distributions. A second order polynomial is used for intervals (1.0, 1.5) GeV/c and (1.5, 2.0) GeV/c, while third order is employed in (2.0, 2.5) GeV/c and (2.5, 3.0) GeV/c.

4.1.2 Optimal Fit Conditions

During the signal extraction procedure, some precautions are taken to ensure the best analysis of the data. In particular, the fitting process requires several conditions to be set; these are: the (background) fit functions, the fit invariant mass range and the selected rebinning. Moreover, the values of the mean and the standard deviation of the signal gaussian, as its fundamental parameters, are important to determine the corresponding shape of the signal. In some cases, it is actually better to fix their values according to the available information, rather than letting them vary without any constraint. Of course, this is most advisable when dealing with low significance instances. In particular, in the present work it has been necessary to fix means and standard deviations in the case of the first and the last intervals: (1.0, 1.5) GeV/c and (36.0, 50.0) GeV/c, which, incidentally, are characterised by the lowest significances. In particular, values $\mu = 1.867$ GeV/c^2 and $\sigma = 0.011$ GeV/c^2 have been set in the first case. For the last bin, instead, $\mu = 1.868$ GeV/c^2 and $\sigma = 0.029$ GeV/c^2 have been chosen. These choices are justified considering both physical and analysis-related arguments. Concerning the mean, on the one hand, the signal gaussian peak is to be centred reasonably close to the actual value of the neutral D meson mass (taking into account the mentioned discrepancy). On the other, since besides these two intervals analysis the fit is always accomplished smoothly, if a trend is observed for such quantities, it is plausible to argue that the unsettled values be fixed keeping into account such behaviour as well. As for the standard deviation, the transverse momentum resolution dependence along with other factors contribute to a roughly increasing behaviour as a function of p_{T}, so that (in this specific case) extrapolating its value on the basis of the pattern shown in the further intervals can be regarded as a reasonable option. As a matter of fact, failing to constrain these quantities, does result in a worse estimation of the corresponding differential yields, which then propagates across the later stages of the analysis. The trends of mean, standard deviation and signal yields as functions of the transverse momentum are reported in figure 4.5.

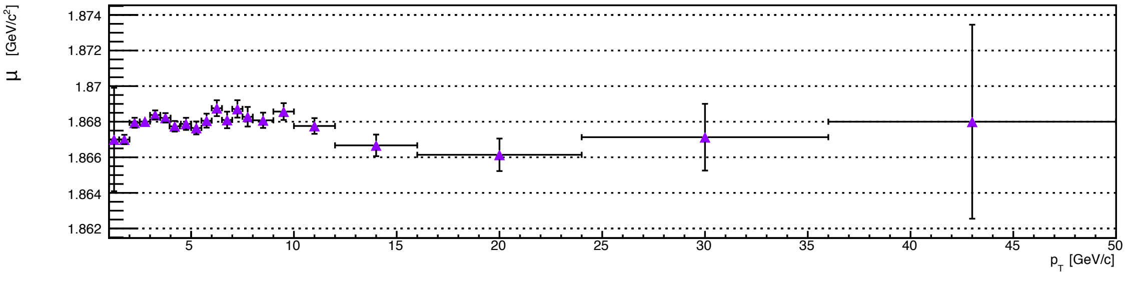

Figure 4.4: Gaussian centroid value in studied intervals. Statistical uncertainties on its value (vertical) are extracted as the uncertainty on fit parameter.

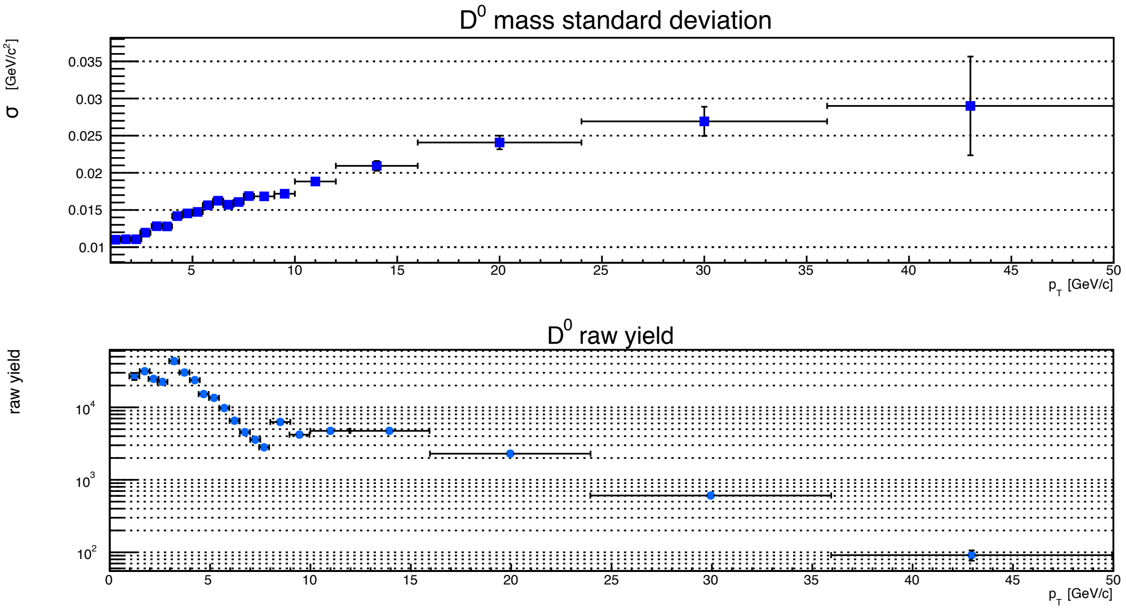

Figure 4.5: Gaussian standard deviation and raw yields in studied intervals. Statistical uncertainties (vertical) on width are extracted as the uncertainty on fit parameter. A p_T-increasing trend is observed for the width, as a result of the worsening transverse momentum resolution at larger p_T's. Raw yields are extracted as the gaussian area divided by the histogram bin width. Their statistical uncertainties stem from the amplitude of the fit gaussian. A decreasing trend shows at high p_T due to lower likelihood of hard D^0's.

From the proposed plots, it is evident that the discussed extrapolation is not always straightforward. In fact, while the standard deviation tends to increase with transverse momentum (meaning worse mass resolution), the mean values do not show a regular behaviour. Therefore, the values have been eventually set seeking a compromise of preliminary fit results and extrapolation. As for the raw yields, since their value depends on the statistics collected in each different p_T interval and the corresponding efficiencies, no smooth trend is expected; a depletion is justifiably observed at increasing momentum due to the progressively lower likelihood of observing harder and harder mesons.

4.1.3 D^0 Raw Yields

The residual plots stemming from the subtraction of the background function from the distributions are shown in figures 4.6, 4.7, 4.8 and 4.9. The corresponding D^0 inclusive (prompt and feed-down) raw yields and statistical significances are thereby reported as well. The presence of a D^0 peak is undoubtable for all the bins, however low the significance may be. Incidentally, it can be shown that both the first and the last p_T-bins (as the lowest significance cases) yields are above the so-called *observation threshold* set with a (upper) 95% confidence level.[3]

---

[3] The observation threshold characterising a given region of interest is an upper bound above which one can speak of observation of a signal, which is to be conceived of as a contamination with respect to the

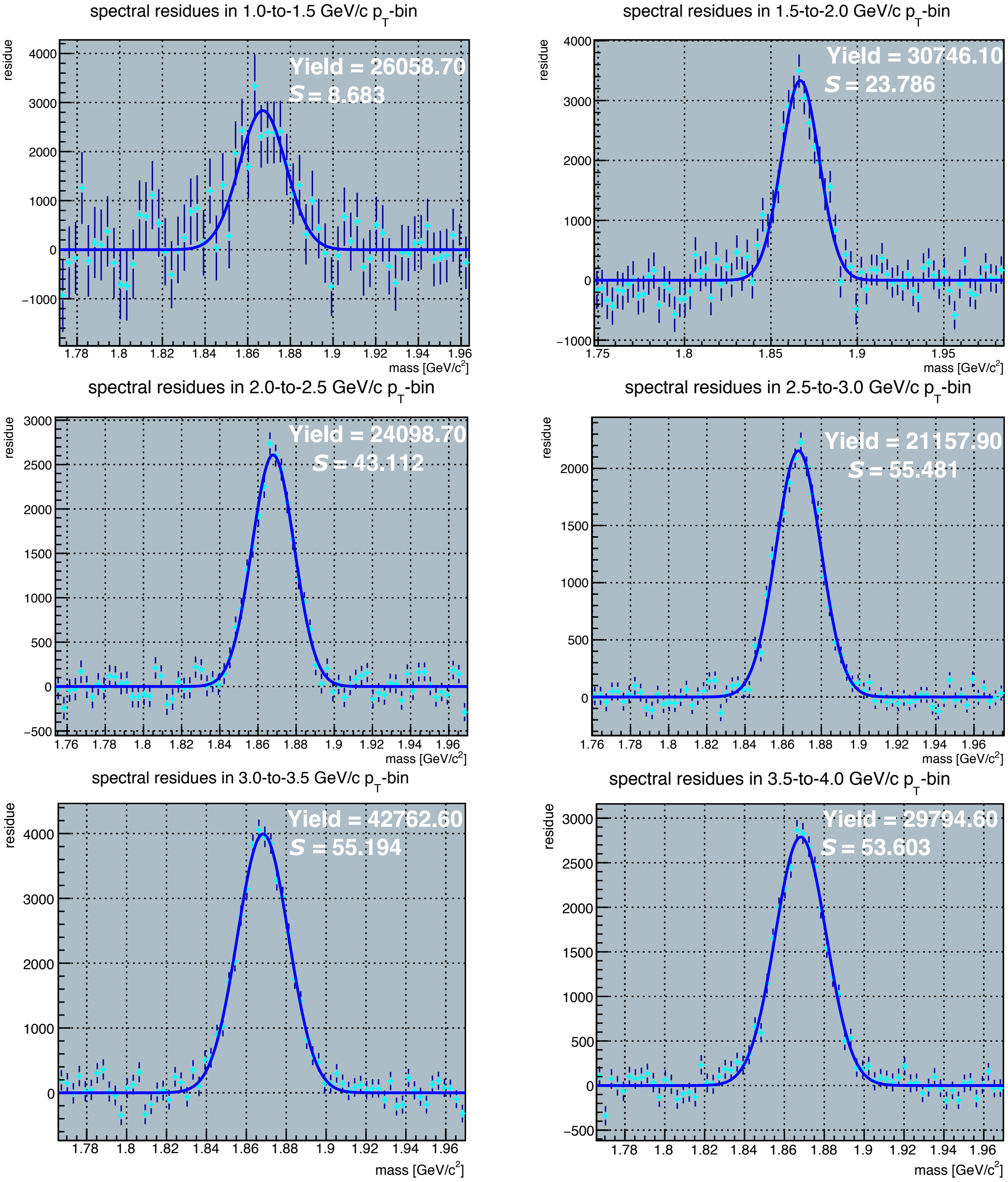

Figure 4.6: Post-background-subtraction residual plots in transverse momentum range (1.0, 4.0) GeV/c. The fit gaussian is shown in blue as a reproduction of the trend of experimental points, appearing in cyan. Raw yield and corresponding significance are also reported in plots. A prominent peak is visible in all p_{T} bins.

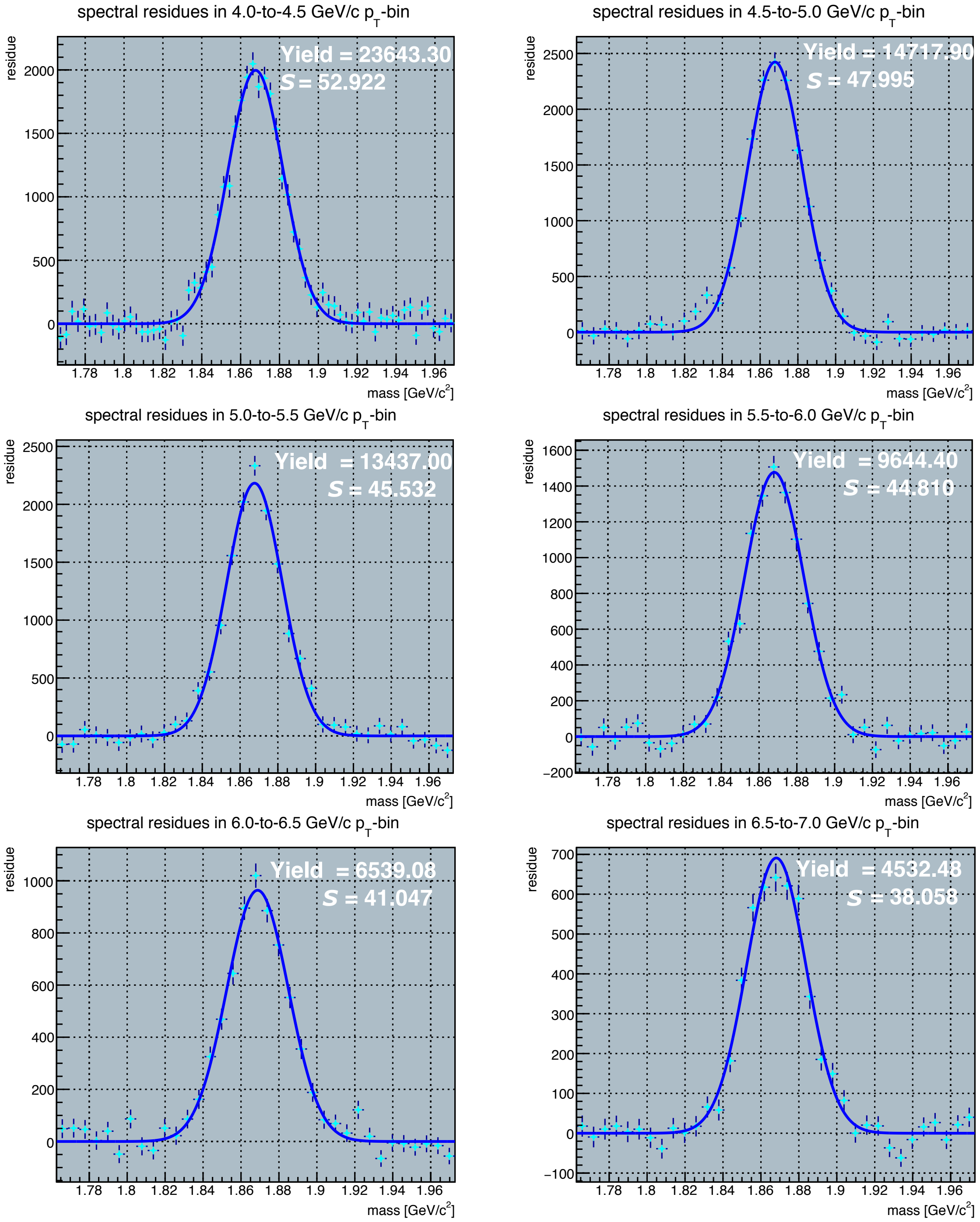

Figure 4.7: Post-background-subtraction residual plots in transverse momentum range (4.0, 7.0) GeV/c. The fit gaussian is shown in blue as a reproduction of the trend of experimental points, appearing in cyan. Raw yield and corresponding significance are also reported in plots. A prominent peak is visible in all p_{T} bins.

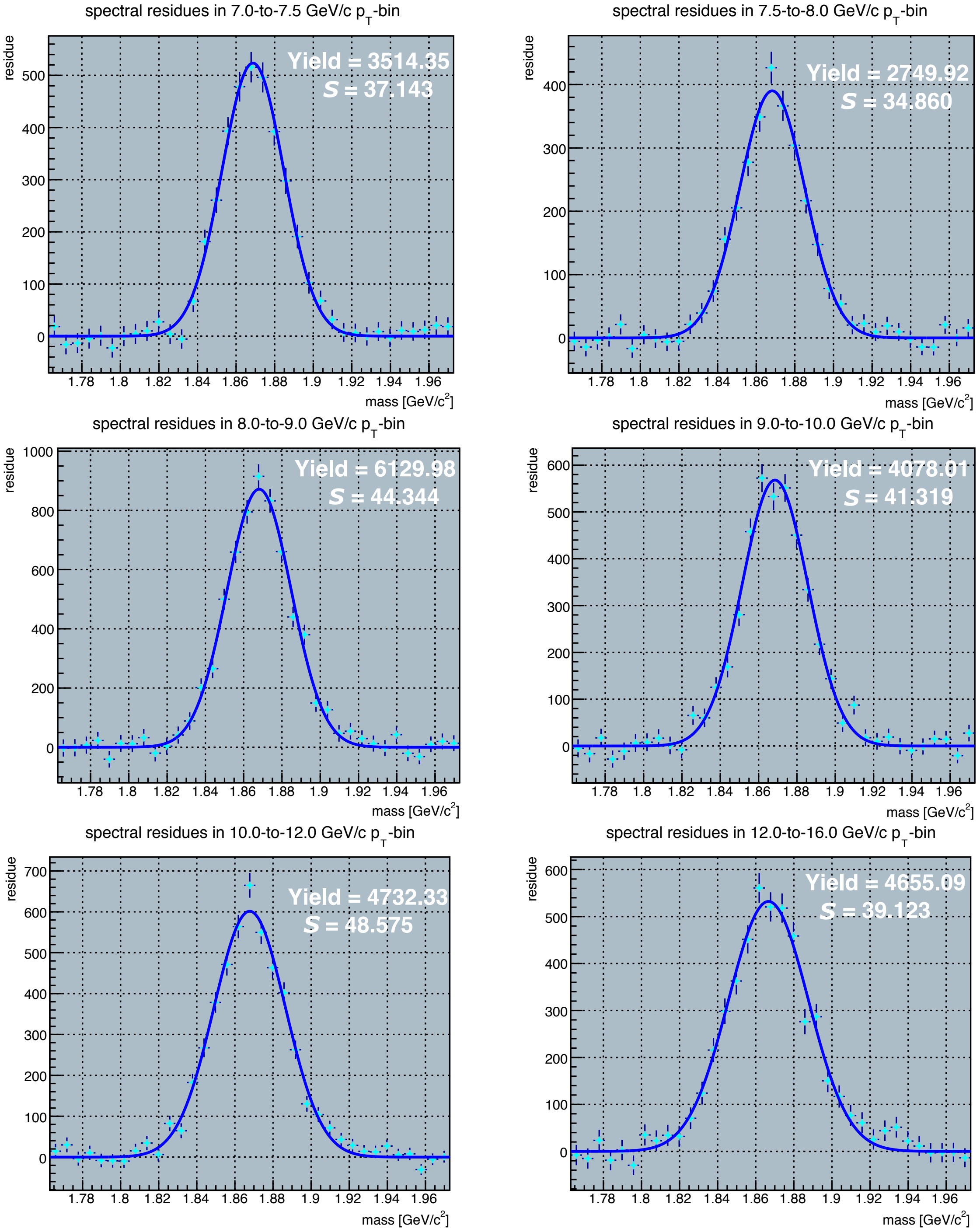

Figure 4.8: Post-background-subtraction residual plots in transverse momentum range (7.0, 16.0) GeV/c. The fit gaussian is shown in blue as a reproduction of the trend of experimental points, appearing in cyan. Raw yield and corresponding significance are also reported in plots. A prominent peak is visible in all p_T bins.

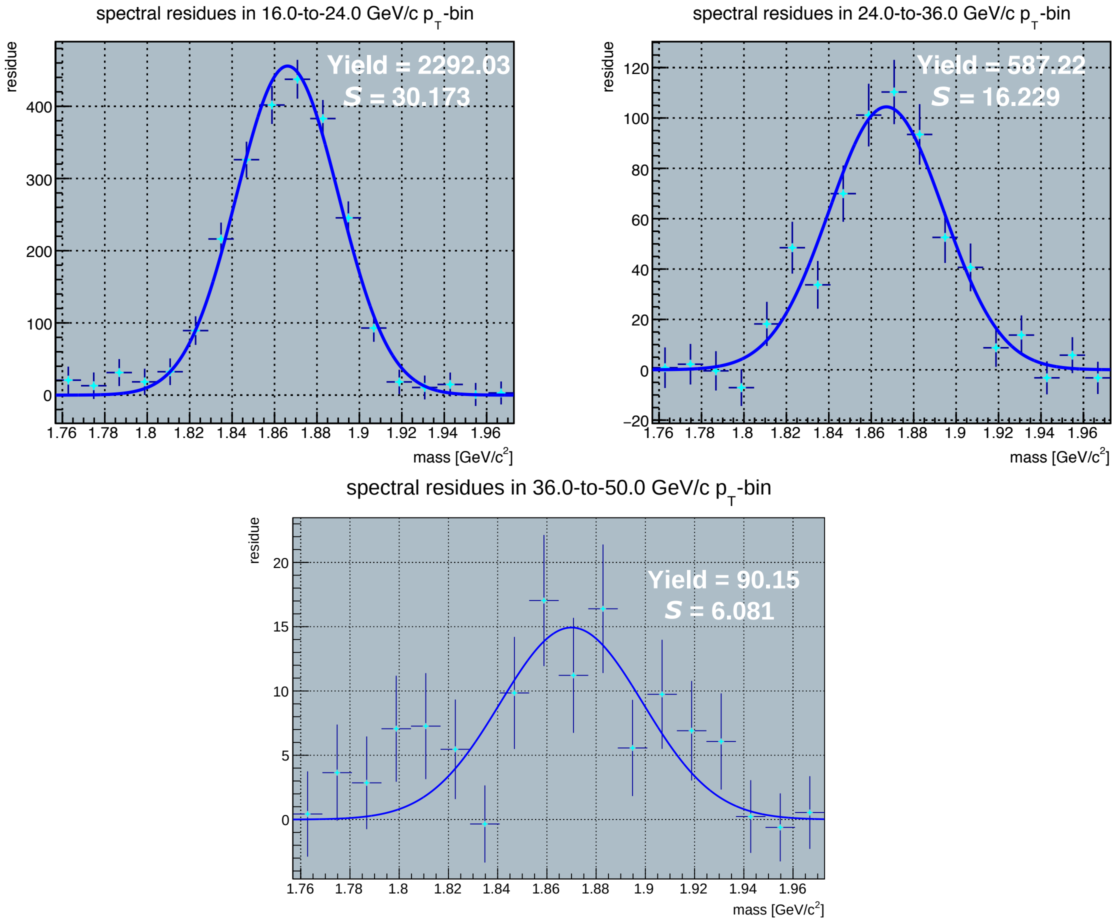

Figure 4.9: Post-background-subtraction residual plots in transverse momentum range (16.0, 50.0) GeV/c. The fit gaussian is shown in blue as a reproduction of the trend of experimental points, appearing in cyan. Raw yield and corresponding significance are also reported in plots. A prominent peak is visible in all p_{T} bins.

Of course, the fit conditions selected bin by bin affect the values of yields and significances. For this reason, any reasonable variation on them is accounted for by estimating a global systematic uncertainty, as will be presented later.

Reflections

The selected candidates have been classified either as a D^0 or a $\bar{\mathrm{D}}^0$ by employing the kaon-pion decay channel. In some cases, candidates are compatible with both hypotheses. These are included in the analysis twice, thus mistaking their identity in one case.

When kaon and pion tracks of opposite sign candidates are misidentified, mistaking the pion for the kaon and viceversa, the term *reflection* is used. This phenomenon alters the shape of the invariant mass distributions. As a matter of fact, since the mass and momentum values are mismatched, these candidates are not distributed according to a

---

background. In the hypothesis of a Poisson statistics, it is formally defined as follows: DT$= k\sqrt{2(n_{\mathrm{bkg}}+1)}$, where k is a coverage factor depending on the confidence interval set.

gaussian. They instead show a broader distribution. A comparison is shown in figure 4.10, where the higher importance of such effect at high transverse momentum is also evident.

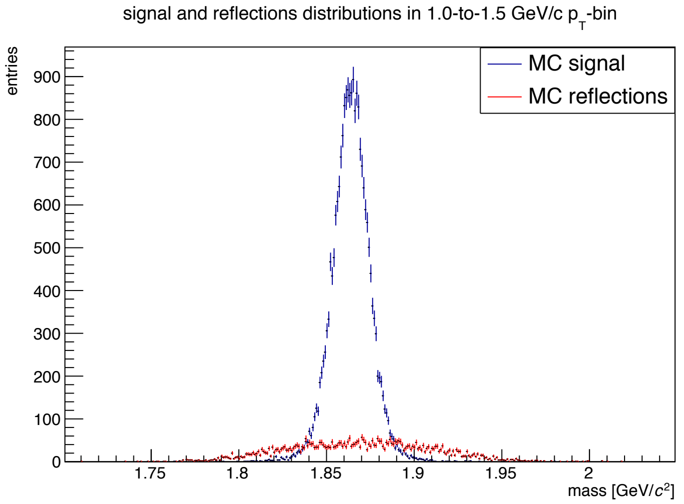

(a) *MC signal and reflections distributions in (1.0, 1.5) GeV/c.*

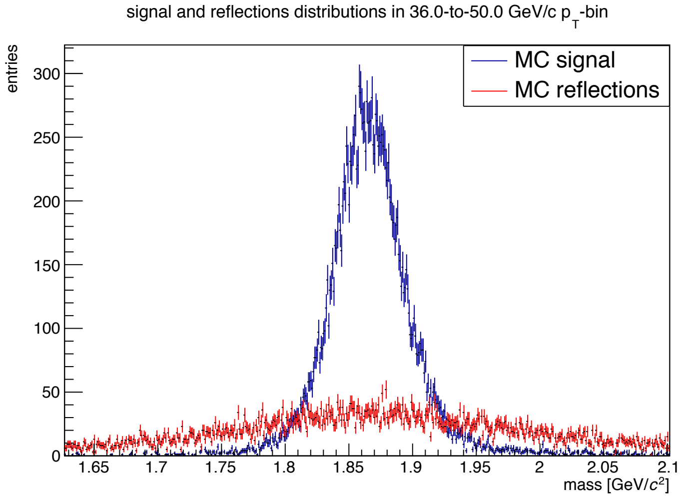

(b) *MC signal and reflections distributions in (36.0, 50.0) GeV/c.*

Figure 4.10: MC reflections templates superposed on respective signal distributions in lowest and highest transverse momentum intervals. The importance of the effect is evidently higher at larger p_{T}'s.

In this thesis work, the contribution of reflections has not been accounted for, based on the fact that they contribute mostly at high transverse momentum, where particles specific energy loss and time of flight are similar, which makes identification harder.

4.2 Feed-down Subtraction

Topological cuts have been optimised with the goal of retaining a large fraction of prompt D^0's. On the other hand, the raw yields extracted from actual data are inclusive, that is, both prompt and feed-down mesons are counted. In order to isolate prompt particles, thus, it is necessary to compute an estimate of the prompt fraction in each bin. To do so, expressions 3.4 and 3.5 are employed. However, since computing the raw yield of feed-down objects requires the knowledge of the feed-down nuclear modification factor, the strategy explained subsequently is employed:

- Prompt Nuclear Modification Factor Extraction;
  Starting from its definition, the prompt D^0 R_{AA} can be computed:

$$R_{AA;\mathrm{PR}} = \frac{1}{\langle T_{AA}\rangle}\frac{\mathrm{dN}_{AA;\mathrm{PR}}}{\mathrm{d}p_{\mathrm{T}}}\Bigg/\frac{\mathrm{d}\sigma_{pp;\mathrm{PR}}}{\mathrm{d}p_{\mathrm{T}}}, \tag{4.2}$$

  where the prompt D^0 corrected yield per unit collision reads:[4]

$$N_{AA;\mathrm{PR}} = \frac{\mathrm{N_{raw;PR}}}{2\varepsilon_{\mathrm{PR}} b_r \mathrm{N_{events}}} = \frac{\mathrm{N_{raw;TOT}} - \mathrm{N_{raw;FD}}}{2\varepsilon_{\mathrm{PR}} b_r \mathrm{N_{events}}}, \tag{4.3}$$

  thus:

$$R_{AA;\mathrm{PR}} = \frac{1}{\langle T_{AA}\rangle}\left[\frac{1}{2\varepsilon_{\mathrm{PR}} b_r \mathrm{N_{events}}}\frac{\mathrm{d}\big(\mathrm{N_{raw;TOT}} - \mathrm{N_{raw;FD}}\big)}{\mathrm{d}p_{\mathrm{T}}}\right]\Bigg/\frac{\mathrm{d}\sigma_{pp;\mathrm{PR}}}{\mathrm{d}p_{\mathrm{T}}}. \tag{4.4}$$

  Incidentally, the right-hand side second term of equation 4.4 can be expressed in an advantageous way:

$$\frac{1}{2\varepsilon_{\mathrm{PR}} b_r \mathrm{N_{events}}}\frac{\mathrm{dN_{raw;FD}}}{\mathrm{d}p_{\mathrm{T}}} = \frac{\varepsilon_{\mathrm{FD}}}{\varepsilon_{\mathrm{PR}}}\frac{\mathrm{dN_{AA;FD}}}{\mathrm{d}p_{\mathrm{T}}} \tag{4.5}$$

  and since:

$$\frac{\mathrm{dN_{AA;FD}}}{\mathrm{d}p_{\mathrm{T}}} = \langle T_{AA}\rangle \times \frac{\mathrm{d}\sigma_{pp;\mathrm{FD}}}{\mathrm{d}p_{\mathrm{T}}} \times R_{AA;\mathrm{FD}}, \tag{4.6}$$

  holds, too, the following formula is obtained for the prompt nuclear modification factor:

$$R_{AA;\mathrm{PR}} = \frac{1}{\langle T_{AA}\rangle}\left[\frac{\mathrm{dN_{raw;TOT}}/\mathrm{d}p_{\mathrm{T}}}{2\varepsilon_{\mathrm{PR}} b_r \mathrm{N_{events}}} - \left(\frac{\varepsilon_{\mathrm{FD}}}{\varepsilon_{\mathrm{PR}}}\langle T_{AA}\rangle \times \frac{\mathrm{d}\sigma_{pp;\mathrm{FD}}}{\mathrm{d}p_{\mathrm{T}}} \times R_{AA;\mathrm{FD}}\right)\right]\Bigg/\frac{\mathrm{d}\sigma_{pp;\mathrm{PR}}}{\mathrm{d}p_{\mathrm{T}}} \tag{4.7}$$

  At this point, to be able to evaluate the prompt R_{AA}, it is necessary to know all the ingredients appearing in equation 4.7. That is the case for all the factors apart from the feed-down nuclear modification factor, which is currently unknown. In particular, the pp prompt and feed-down cross sections are measured [30] and computed (FONLL), respectively. As for the incognita, recent CMS non-prompt J/Ψ results [31] are exploited to extract such quantity, leading to the following hypotheses:[5]

$$R_{AA;\mathrm{FD}} = \begin{cases} 1.5R_{AA;\mathrm{PR}} & \text{for: } 1 \leq p_{\mathrm{T}}/(\mathrm{GeV}/c) < 3, \\ 2R_{AA;\mathrm{PR}} & \text{for: } p_{\mathrm{T}}/(\mathrm{GeV}/c) \geq 3, \end{cases} \tag{4.8}$$

---

[4] Hereon, more simply corrected yield.

[5] These hypotheses will be studied as possible sources of systematic uncertainty by changing the value of the proportionality constant.

in agreement with hypothesis of lower energy loss for b quarks through the plasma.

The prompt nuclear modification factor is thus extracted employing the subsequent equation:[6]

$$R_{AA;\mathrm{PR}} = \frac{1}{\langle T_{AA}\rangle} \frac{\frac{\mathrm{dN_{raw;TOT}}/\mathrm{d}p_{\mathrm{T}}}{2\varepsilon_{\mathrm{PR}} b_r \mathrm{N_{events}}}}{\mathrm{d}\sigma_{pp;\mathrm{PR}}/\mathrm{d}p_{\mathrm{T}}} \left[1 + \left(\alpha \times \frac{\varepsilon_{\mathrm{FD}}}{\varepsilon_{\mathrm{PR}}} \times \frac{\mathrm{d}\sigma_{pp;\mathrm{FD}}}{\mathrm{d}p_{\mathrm{T}}} \Big/ \frac{\mathrm{d}\sigma_{pp;\mathrm{PR}}}{\mathrm{d}p_{\mathrm{T}}}\right)\right]^{-1}. \tag{4.9}$$

- Prompt Fraction Estimate;

  At this stage, the fraction of prompt D^0 mesons can be estimated using equations 3.4 and 3.5. Assumption 4.8 is used again to compute the feed-down nuclear modification factor starting from the prompt.

- Feed-down Subtracted Spectrum Extraction.

  The prompt fraction is ultimately implemented as the factor correcting the inclusive raw yield, retaining only its prompt component. The D^0 transverse momentum differential spectrum is obtained as follows:

  $$\frac{\mathrm{dN_{AA;PR}}}{\mathrm{d}p_{\mathrm{T}}} = \frac{f_{prompt}}{2\varepsilon_{\mathrm{PR}} b_r \mathrm{N_{events}}} \frac{\mathrm{dN_{raw;TOT}}}{\mathrm{d}p_{\mathrm{T}}}. \tag{4.10}$$

  The p_{T} dependence of all factors (except for the total number of events, $\mathrm{N_{events}}$) is omitted for brevity.

In figure 4.11, the prompt and feed-down efficiencies (contribution from various reconstruction efficiency times detector acceptance) employed to compute results are shown. The correction is seen in both cases to grow as a function of transverse momentum. This is partly due to the tighter cuts applied in the low-p_{T} range.

4.3 Systematic Uncertainties

Before reporting the prompt D^0 differential p_{T}-spectrum and nuclear modification factor, the possible sources of systematic deviations are listed and the procedure leading to the estimation of a global systematic uncertainty is described.

Most important systematic effects are due to discrepancies between physical reality and the assumptions made in the context of the following stages of the analysis:

- Yield extraction;
- Cut efficiency;
- Monte-Carlo p_{T}-shape;
- Tracking efficiency.

---

[6] The proportionality constant between the prompt and feed-down nuclear modification factors introduced in assumption 4.8 is denoted as α in the rest of the derivation for the sake of generality.

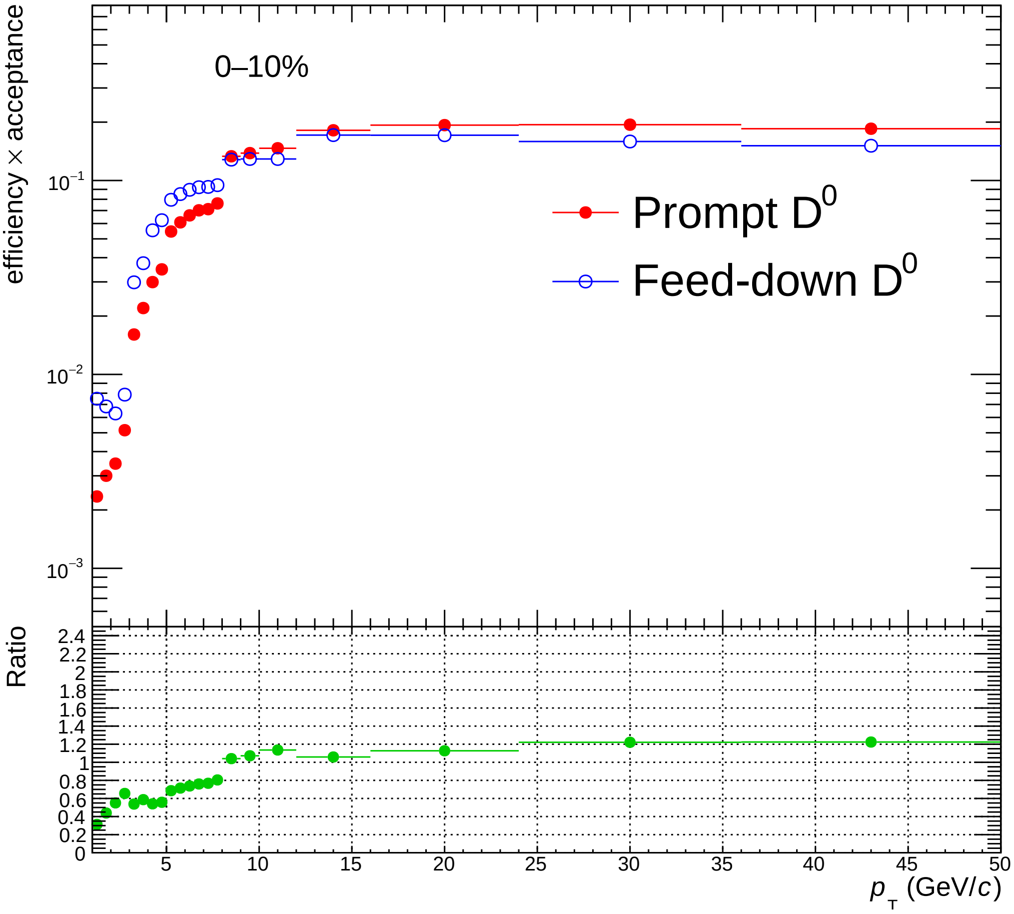

Figure 4.11: Full prompt and feed-down efficiencies (efficiency × acceptance) for the transverse momentum intervals under study. The two quantities ratio is reported in the lower part of the figure.

The deviations between results obtained for central and non-central conditions (i.e., different from those selected as best) allow an estimation of the uncertainty bin per bin. In particular, where applicable, the standard deviation of such differences has been considered as the final estimate deriving from a given source, except for those cases where stated differently. Different sources are assumed as independent and for each transverse momentum interval the global estimate is evaluated by computing the squared root of the quadratic sum of the corresponding uncertainties. Each of these is actually made to vary more uniformly than observed throughout the studied transverse momentum range, in the assumption that in the event of a systematic effect, this cannot oscillate considerably from a bin to the one next to it. Also, possible outliers, i.e., values of the discrepancy coming from the same source relatively far from the others computed in the same bin, are not considered when estimating the smoothened uncertainty value.

4.3.1 Yield Extraction

The fit range, background function, histogram rebinning and values of parameters finally determine the inclusive raw yield of neutral D mesons. In order to estimate the systematic uncertainty contribution as due to the yield extraction, these conditions are varied across intervals or sets of alternatives deemed reasonable, at the same time retaining the quality of the fit. In some instances, specific variations are not acceptable, leading to unrealistic yields and/or low-quality fits. Therefore, such cases have been discarded. The relative systematic uncertainties associated to the yield extraction (and thus, affecting raw yields) are reported in table 4.3.

p_{T}-bin (GeV/c)	$u_{\mathrm{ye}}(p_{\mathrm{T}})$ (%)	p_{T}-bin (GeV/c)	$u_{\mathrm{ye}}(p_{\mathrm{T}})$ (%)	p_{T}-bin (GeV/c)	$u_{\mathrm{ye}}(p_{\mathrm{T}})$ (%)
(1.0, 1.5)	9	(4.5, 5.0)	4	(8.0, 9.0)	4
(1.5, 2.0)	9	(5.0, 5.5)	4	(9.0, 10.0)	5
(2.0, 2.5)	3	(5.5, 6.0)	4	(10.0, 12.0)	5
(2.5, 3.0)	3	(6.0, 6.5)	4	(12.0, 16.0)	5
(3.0, 3.5)	3	(6.5, 7.0)	4	(16.0, 24.0)	6
(3.5, 4.0)	4	(7.0, 7.5)	4	(24.0, 36.0)	6
(4.0, 4.5)	4	(7.5, 8.0)	4	(36.0, 50.0)	6

Table 4.3: Smoothened yield extraction relative systematic uncertainty for p_{T} intervals between 1 and 50 GeV/c.

4.3.2 Cut Efficiency

The implementation of different topological cuts implies the rejection of a varying fraction of prompt and feed-down D mesons besides the background. The conserved fractions are called cut efficiencies and are included in the total efficiencies used to correct the raw yields. Of course, an accurate evaluation of such numbers is not feasible by making use of experimental data. Instead, MC samples are used to this end. This way, one should in principle be able to always recover the actual number of particles decaying in a specific channel, regardless of the chosen cuts. However, the discrepancy between simulations and experimental reality brings about a deviation from the ideal (and the baseline) corrected yield value. Given these arguments and following the order of the feed-down subtraction procedure described in section 4.2, the systematic uncertainty arising from the cut variation is estimated on the prompt R_{AA} by assessing the difference between non-central and central values

A set of six different cuts has been considered. More specifically, starting from the central cuts proposed in tables 3.2, 3.3, 4.1 and 4.2, progressively looser and tighter cuts have been implemented. Decay length and impact parameters product are first varied, then the cosine of the pointing angle projection and the topomatic, and finally $\cos\vartheta_{\mathrm{pt}}$, while restoring the central value of $\cos\vartheta_{\mathrm{pt}xy}$. The order of such variations is mostly descending in the cut variable impact, except for the cosines case, where the precedence is given to the projection to probe the converse case with respect to the cut optimisation study subject of chapter 3.

The cut variation (relative) systematic uncertainty estimates are presented in table 4.4. Their values are proposed on the basis of figure 4.12, shown below, after being subjected to a smoothening procedure to make their overall variation more uniform.

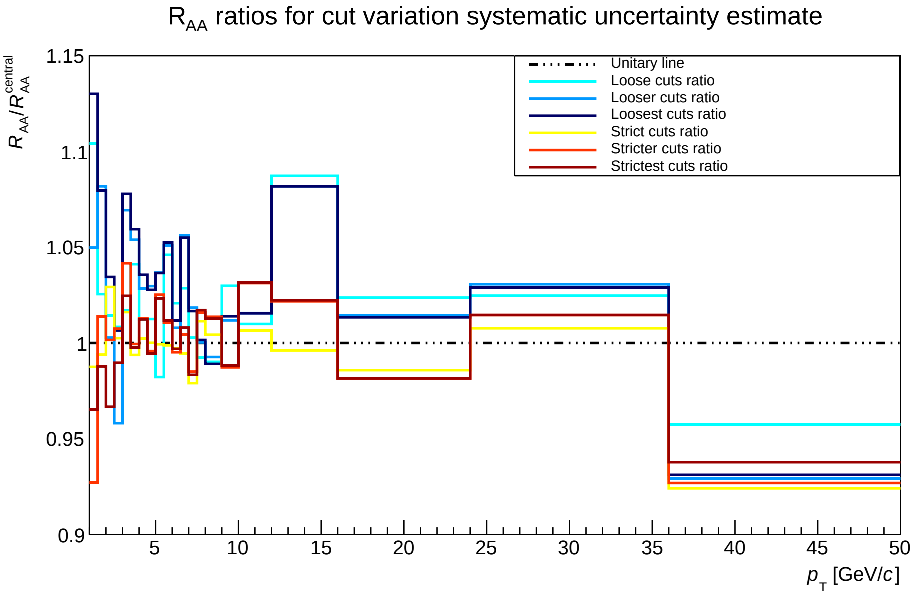

Figure 4.12: Varied cuts to central cuts nuclear modification factors ratio as the relevant quantity for the estimation of corresponding systematic uncertainty cut variation contribution.

p_{T}-bin (GeV/c)	$u_{\mathrm{cv}}(p_{\mathrm{T}})$ (%)	p_{T}-bin (GeV/c)	$u_{\mathrm{cv}}(p_{\mathrm{T}})$ (%)	p_{T}-bin (GeV/c)	$u_{\mathrm{cv}}(p_{\mathrm{T}})$ (%)
(1.0, 1.5)	7	(4.5, 5.0)	5	(8.0, 9.0)	5
(1.5, 2.0)	7	(5.0, 5.5)	5	(9.0, 10.0)	5
(2.0, 2.5)	7	(5.5, 6.0)	5	(10.0, 12.0)	5
(2.5, 3.0)	7	(6.0, 6.5)	5	(12.0, 16.0)	5
(3.0, 3.5)	7	(6.5, 7.0)	5	(16.0, 24.0)	5
(3.5, 4.0)	7	(7.0, 7.5)	5	(24.0, 36.0)	5
(4.0, 4.5)	5	(7.5, 8.0)	5	(36.0, 50.0)	5

Table 4.4: Smoothened cut variation relative systematic uncertainty on R_{AA} for p_{T} intervals between 1 and 50 GeV/c.

4.3.3 Monte-Carlo p_{T}-Shape

Another factor affecting efficiencies is the discrepancy between the simulated and actual D^0 momentum distributions. Starting from the cut efficiency as a function of p_{T}, its bin-wise value can be thought of as a mean of punctual values considered at the extremes of the interval, weighed on the D^0 momentum spectrum. From this viewpoint, it is easy to see how a systematic effect is introduced in using a simulated spectrum. The magnitude of such effect depends on the momentum binning and on the variation of the efficiency inside each interval: narrower bins lead to better estimates because the efficiency variation decreases if the bin width does. The contribution of this effect to the systematic uncertainty can be quantified through the spread between the central R_{AA} and that computed using efficiencies stemming from a different momentum spectrum for the MC samples. In particular, the p_{T} distribution from a FONLL calculation multiplied by the R_{AA} value from one of the models that closely describe the central value of the measurement [3, 32] is used.

The p_{T}-shape relative systematic uncertainties on the R_{AA} are reported in table 4.5.

p_{T}-bin (GeV/c)	$u_{\mathrm{ps}}(p_{\mathrm{T}})$ (%)	p_{T}-bin (GeV/c)	$u_{\mathrm{ps}}(p_{\mathrm{T}})$ (%)	p_{T}-bin (GeV/c)	$u_{\mathrm{ps}}(p_{\mathrm{T}})$ (%)
(1.0, 1.5)	1.50	(4.5, 5.0)	0.10	(8.0, 9.0)	0.05
(1.5, 2.0)	1.50	(5.0, 5.5)	0.10	(9.0, 10.0)	0.05
(2.0, 2.5)	1.50	(5.5, 6.0)	0.10	(10.0, 12.0)	0.05
(2.5, 3.0)	0.50	(6.0, 6.5)	0.05	(12.0, 16.0)	0.00
(3.0, 3.5)	0.50	(6.5, 7.0)	0.05	(16.0, 24.0)	0.00
(3.5, 4.0)	0.50	(7.0, 7.5)	0.05	(24.0, 36.0)	0.00
(4.0, 4.5)	0.50	(7.5, 8.0)	0.05	(36.0, 50.0)	0.00

Table 4.5: Smoothened p_{T}-shape relative systematic uncertainty on R_{AA} for p_{T} intervals between 1 and 50 GeV/c.

4.3.4 Tracking Efficiency

The tracking efficiency is the capability of track reconstruction algorithms to correctly associate the points belonging to the same track and at the same time discard those that do not. Of course, this quantity is not expected to be unitary since the reconstruction strategy is based on a χ^2-like procedure involving the clusters positions and thus has finite reconstruction power. In particular, it can be affected by several factors, among which, for instance, a misalignment of tracking detectors or the presence of inactive regions. The systematic uncertainties components arising from effects influencing the tracking efficiency, extracted for the nuclear modification factor are reported in table 4.6.

p_T-bin (GeV/c)	$u_\mathrm{te}(p_\mathrm{T})$ (%)	p_T-bin (GeV/c)	$u_\mathrm{te}(p_\mathrm{T})$ (%)	p_T-bin (GeV/c)	$u_\mathrm{te}(p_\mathrm{T})$ (%)
(1.0, 1.5)	10	(4.5, 5.0)	11	(8.0, 9.0)	8
(1.5, 2.0)	10	(5.0, 5.5)	10	(9.0, 10.0)	8
(2.0, 2.5)	10	(5.5, 6.0)	10	(10.0, 12.0)	8
(2.5, 3.0)	10	(6.0, 6.5)	9	(12.0, 16.0)	7
(3.0, 3.5)	11	(6.5, 7.0)	9	(16.0, 24.0)	7
(3.5, 4.0)	11	(7.0, 7.5)	9	(24.0, 36.0)	6
(4.0, 4.5)	11	(7.5, 8.0)	9	(36.0, 50.0)	6

Table 4.6: Smoothened tracking efficiency relative systematic uncertainty on R_{AA} for p_T intervals between 1 and 50 GeV/c.

The reported systematic contribution is estimated via the ratios of corrected momentum distributions considered varying the so-called track quality selection. This basically means imposing further constraints on single-track properties in addition to the topological cuts, mostly on the features of the signal recorded by the TPC.

4.4 Final Results

The prompt D^0 spectrum and nuclear modification factor obtained in this analysis work are reported in the following subsections. A discussion of the observed trend is proposed for the R_{AA}, comparing it to theoretical curves, thereby providing a physical interpretation, and also to previous experimental evidence. Particular attention is directed towards results in low-p_T interval between 1 and 3 GeV/c, as the region of main focus of the present work.

4.4.1 Prompt D^0 Transverse Momentum Spectrum

The prompt D^0 transverse momentum spectrum is obtained by employing equation 4.10. It is normalised by the number of lead-lead collisions considered in the analysis. The trend obtained for such observable is proposed in figure 4.13, with numerical values and corresponding uncertainties reported in table 4.7.

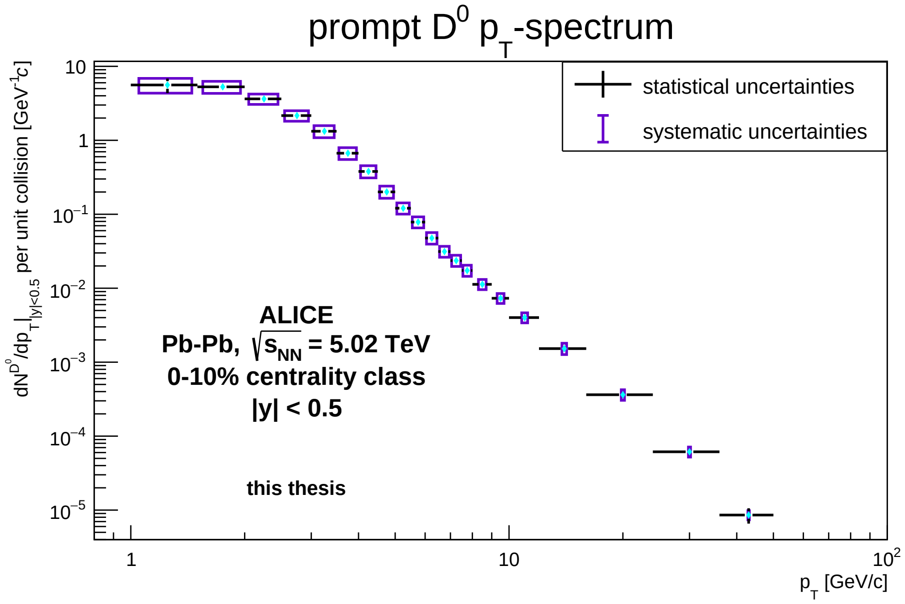

Figure 4.13: Prompt D^0 transverse momentum spectrum in (1.0, 50.0) GeV/c. Logarithmic scales are employed on both axes to highlight low-p_T behaviour and vertical variation across several orders of magnitude.

p_T-bin (GeV/c)	$\frac{1}{\mathrm{N_{events}}}\frac{\mathrm{dN^{D^0}}}{\mathrm{d}p_\mathrm{T}}$ (GeV/c)$^{-1}$	p_T-bin (GeV/c)	$\frac{1}{\mathrm{N_{events}}}\frac{\mathrm{dN^{D^0}}}{\mathrm{d}p_\mathrm{T}}$ (GeV/c)$^{-1}$
(1.0, 1.5)	$5.6 \pm 1.2^{+1.3}_{-1.3}$	(6.5, 7.0)	$0.031 \pm 0.001^{+0.006}_{-0.005}$
(1.5, 2.0)	$5.3 \pm 0.5^{+1.0}_{-1.0}$	(7.0, 7.5)	$0.024 \pm 0.001^{+0.04}_{-0.004}$
(2.0, 2.5)	$3.6 \pm 0.2^{+0.6}_{-0.6}$	(7.5, 8.0)	$(173 \pm 7^{+31}_{-28}) \times 10^{-4}$
(2.5, 3.0)	$2.2 \pm 0.1^{+0.4}_{-0.3}$	(8.0, 9.0)	$(113 \pm 4^{+18}_{-17}) \times 10^{-4}$
(3.0, 3.5)	$1.33 \pm 0.06^{+0.25}_{-0.24}$	(9.0, 10.0)	$(73 \pm 3^{+12}_{-11}) \times 10^{-4}$
(3.5, 4.0)	$0.67 \pm 0.03^{+0.13}_{-0.12}$	(10.0, 12.0)	$(40 \pm 1^{+6}_{-6}) \times 10^{-4}$
(4.0, 4.5)	$0.38 \pm 0.01^{+0.07}_{-0.07}$	(12.0, 16.0)	$(152 \pm 6^{+28}_{-26}) \times 10^{-5}$
(4.5, 5.0)	$0.201 \pm 0.007^{+0.040}_{-0.036}$	(16.0, 24.0)	$(362 \pm 2^{+6}_{-6}) \times 10^{-5}$
(5.0, 5.5)	$0.121 \pm 0.004^{+0.021}_{-0.020}$	(24.0, 36.0)	$(61 \pm 5^{+10}_{-9}) \times 10^{-6}$
(5.5, 6.0)	$0.078 \pm 0.003^{+0.014}_{-0.013}$	(36.0, 50.0)	$(9 \pm 2^{+1}_{-1}) \times 10^{-6}$
(6.0, 6.5)	$0.048 \pm 0.002^{+0.009}_{-0.008}$		

Table 4.7: Prompt D^0 transverse momentum spectrum in (1.0, 50.0) GeV/c with corresponding symmetrical statistical uncertainties and asymmetrical systematic uncertainties.

Statistical and systematic uncertainties are kept separate, being represented with different error bars. The systematic uncertainties contributions have already been discussed. The statistical sources of uncertainty are the inclusive raw yields and the prompt fraction. In turn, the statistical uncertainty of the latter arises from the nuclear modification factor and the inclusive raw yields. The two contributions are thus correlated. Such correlation has not been accounted for in the uncertainty calculation, thus leading to an overestimation of the latter. However, since raw yield contributions are observed to be negligible with respect to the prompt fraction's, the correlation contribution to be subtracted is expected to be even more negligible, which is why it is not considered in the present analysis.

4.4.2 Prompt D^0 Nuclear Modification Factor

The prompt D^0 nuclear modification factor is shown in figure 4.14. Corresponding values accompanied by statistical and systematic uncertainties are presented in table 4.8. Systematic and statistical uncertainties are shown separately. Most contributions to the former have been listed in section 4.3. Additionally, the contributions coming from the FONLL feed-down cross sections and the proportionality hypothesis between R_{AA}'s are included.[7] The statistical uncertainties, instead, stem from the corresponding contributions of raw yields and pp reference.

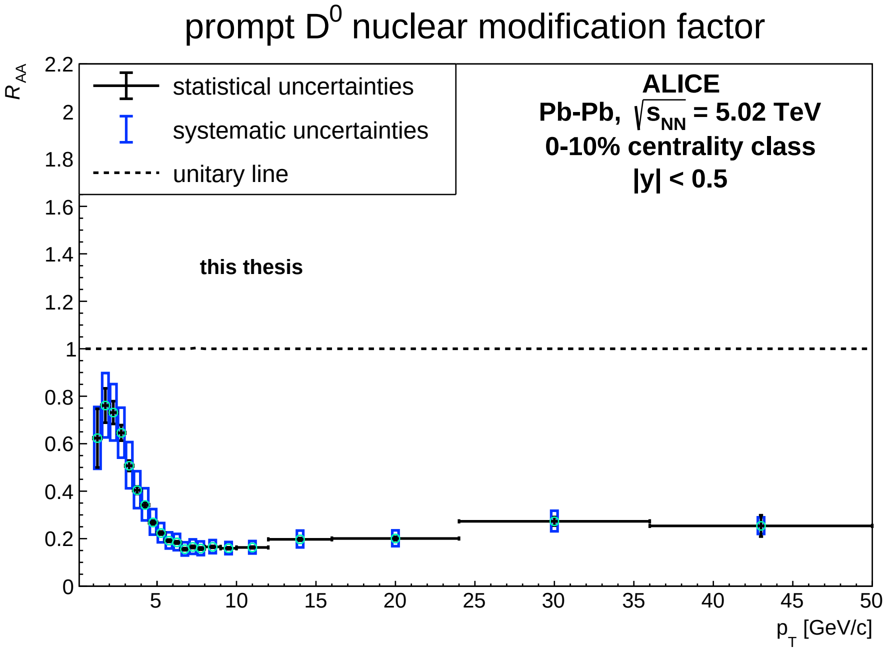

Figure 4.14: Prompt D^0 nuclear modification factor in (1.0, 50.0) GeV/c.

---

[7] To estimate the contribution due to the proportionality hypothesis between R_{AA}'s, values of the proportionality constant have been changed to 1 and 2 for low transverse momentum, and to 1 and 3 for high transverse momentum. Differences between the corresponding nuclear modification factors and the central ones are then used as contributions.

The well-expected suppression with respect to the unitary binary-scaling case is apparent across the entire momentum range. Yet, in the low-p_{T} range, quite higher values are seen, compatibly with the prediction of a shift of the Pb-Pb spectrum due to HF energy loss through the QGP. A comparison with theoretical trends is due to better understand the physics underlying the experimental results. This is the object of the next paragraph.

p_{T}-bin (GeV/c)	R_{AA}	p_{T}-bin (GeV/c)	R_{AA}
(1.0, 1.5)	$0.623 \pm 0.123^{+0.131}_{-0.129}$	(6.5, 7.0)	$0.156 \pm 0.005^{+0.029}_{-0.027}$
(1.5, 2.0)	$0.761 \pm 0.072^{+0.137}_{-0.134}$	(7.0, 7.5)	$0.165 \pm 0.005^{+0.032}_{-0.029}$
(2.0, 2.5)	$0.731 \pm 0.048^{+0.120}_{-0.117}$	(7.5, 8.0)	$0.158 \pm 0.005^{+0.030}_{-0.028}$
(2.5, 3.0)	$0.646 \pm 0.033^{+0.106}_{-0.104}$	(8.0, 9.0)	$0.165 \pm 0.004^{+0.029}_{-0.027}$
(3.0, 3.5)	$0.507 \pm 0.022^{+0.100}_{-0.095}$	(9.0, 10.0)	$0.159 \pm 0.004^{+0.026}_{-0.025}$
(3.5, 4.0)	$0.404 \pm 0.016^{+0.080}_{-0.075}$	(10.0, 12.0)	$0.163 \pm 0.004^{+0.027}_{-0.025}$
(4.0, 4.5)	$0.342 \pm 0.012^{+0.070}_{-0.065}$	(12.0, 16.0)	$0.197 \pm 0.005^{+0.037}_{-0.034}$
(4.5, 5.0)	$0.268 \pm 0.008^{+0.056}_{-0.051}$	(16.0, 24.0)	$0.200 \pm 0.007^{+0.034}_{-0.032}$
(5.0, 5.5)	$0.223 \pm 0.006^{+0.042}_{-0.039}$	(24.0, 36.0)	$0.273 \pm 0.018^{+0.045}_{-0.042}$
(5.5, 6.0)	$0.191 \pm 0.005^{+0.035}_{-0.033}$	(36.0, 50.0)	$0.254 \pm 0.044^{+0.036}_{-0.034}$
(6.0, 6.5)	$0.184 \pm 0.005^{+0.036}_{-0.033}$		

Table 4.8: Prompt D^0 nuclear modification factor in (1.0, 50.0) GeV/c with corresponding symmetrical statistical uncertainties and asymmetrical systematic uncertainties.

Comparison with Theory

In the following, the nuclear modification factor shown in figure 4.14 is represented alongside theoretical trends extracted using different descriptions of the quark gluon plasma, several energy exchange mechanisms and charm hadronisation modes. These are illustrated in detail in [33], [34] and [35]. Here, a brief description of the three models is provided before the comparison with the outcome of the present analysis.

- LIDO;
  LIDO stands for *Linearized Boltzmann with diffusion model.* In this model, the heavy quarks scatter off medium particles described by a linearized Boltzmann equation with pQCD matrix elements (the scattering component), and between

scatterings propagate according to a Langevin equation (the diffusion component) with empirical temperature- and momentum-dependent transport coefficients to describe the soft non-perturbative components of the interaction missing from the above scattering picture. Both elastic and inelastic scatterings are included in the scattering component. The scattering process inside a medium is a multi-scale problem that includes a momentum transfer scale $\mathcal{Q}$ and a medium scale that is proportional to the temperature $\mu\pi$T. The diffusion component has several parameters depending on the way in which transport coefficients are parametrised. The idea is to include non-perturbative contributions in terms of these transport coefficients [33].

- TAMU;
  This approach (developed at the Texas A&M University) implements a strong-coupling scheme in both micro- and macro-physics (i.e., HF transport and bulk evolution, respectively) of QGP and hadronic matter, and has been found to describe HF data at RHIC fairly well. Its building blocks are a quantitatively constrained hydrodynamic bulk evolution into which HF transport is implemented using non-perturbative interactions for heavy quarks and mesons through QGP, hadronisation and hadronic phases of a nuclear collision. Since the diffusion processes are restricted to elastic interactions, it is of particular interest to study whether the much increased p_{T}-reach at the LHC requires additional physics not included in such approach, e.g., radiative processes. For the application to LHC improved heavy-quark baseline spectra and fragmentation in pp collisions are used, along with an update of the heavy quark T-matrix by including the gluonic sector, and a revised tune of the hydrodynamic model to bulk observables [34].

- Catania.
  In the heavy quark sector, in particular for charm flavour, there has been a general consensus on the key role of hadronisation by coalescence to correctly predict the transverse momentum spectra of D mesons. In the considered work, carried out at Catania University, a coalescence plus fragmentation approach is employed to calculate the p_{T} spectrum of charmed D^0 mesons (among the others) in a wide range of transverse momentum from low p_{T} up to about 10 GeV/c. The contribution from decays of heavy hadron resonances and also the one due to fragmentation of heavy quarks which do not undergo the coalescence process are included. The coalescence process is tuned to have all charm quarks hadronising in the $p_{\mathrm{T}} \to 0$ limit, whereas at finite p_{T} charm quarks not undergoing coalescence are hadronised by independent fragmentation [35].

The comparison between the experimental and theoretical nuclear modification factors for prompt D^0 mesons is shown in figure 4.15. Logarithmic scale is used for the horizontal axis to highlight low-p_T behaviour.

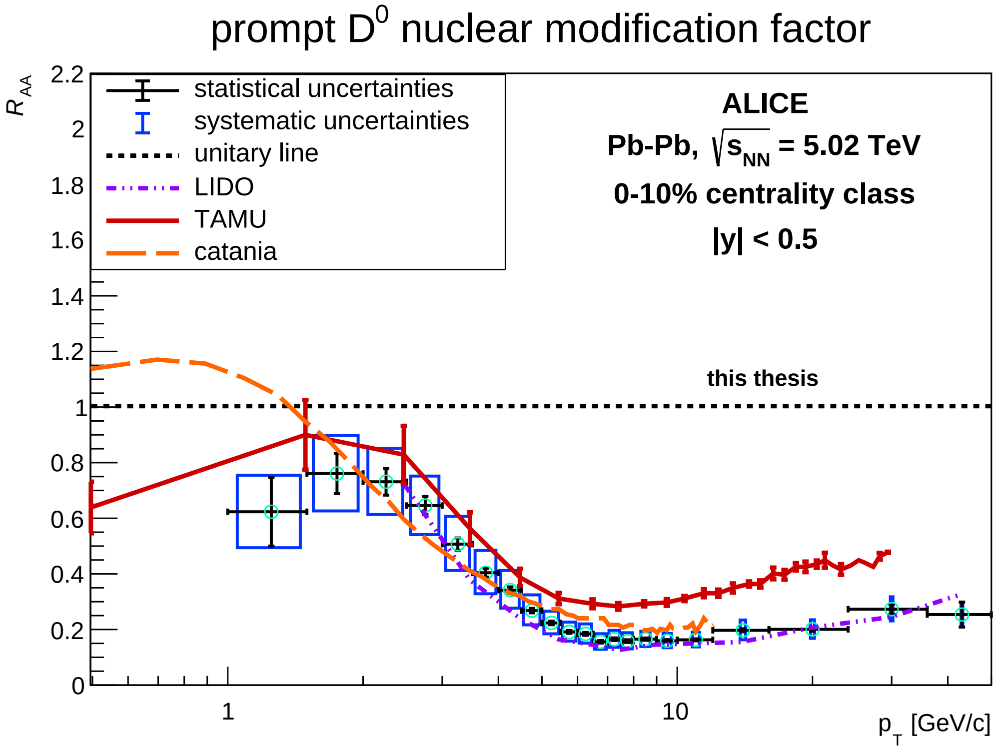

Figure 4.15: Prompt D^0 nuclear modification factor in (0.5, 50.0) GeV/c. This thesis measurements and theoretical models LIDO [33], TAMU [34] and Catania [35] are compared.

Below $p_T = 2.5$ GeV/c, a bump which is often ascribed to recombination effects combined with a radial flow "boost" is evident.[8] The value of the nuclear modification factor stays below unity. In most models, this is due to nuclear shadowing of the initial state parton distribution functions.[9] Here, the experimental trend is best described by the TAMU nuclear modification factor: although somewhat overestimated, the deviation seems to be overall covered by uncertainties in both the experimental measurements and the model. The Catania prediction of the R_{AA} is actually enhanced in the low-p_T range and a prominent peak is visible around 1.0 GeV/c, incompatibly with the outcome of the present analysis. The LIDO curve, instead, is not defined for such range of transverse momentum. As momentum grows, on the other hand, it is the latter to best describe the experimental data: the two trends are compatible within uncertainties. The Catania model does achieve a better agreement than it does at lower values of p_T, although still not fully satisfactory as a description of observations. Finally, the TAMU R_{AA} is not suppressed enough from 5 GeV/c on, with an increasing discrepancy as momentum grows.

The TAMU and Catania models, as those providing a description at low transverse

---

[8] Radial flow is a hydrodynamical effect associated to the plasma radial expansion after thermalisation.

[9] Nuclear shadowing consists in the suppression of very-low x ($\lesssim 10^{-2}$) partons in the nuclear landscape.

momentum, both include the coalescence hadronisation mechanism, with the latter relying rather heavily on it in such range. A crucial difference between the two papers seems to be the use of non-perturbative lattice QCD and perturbative QCD, respectively. This could be a reason behind the better agreement between TAMU and the outcome of this thesis work analysis for such range. A point in favour of this idea is the fact that the vice versa is actually observed as momentum increases, with Catania nuclear modification factor approaching the experimental one, and TAMU's getting farther. Of course, to say that this can be regarded as the main reason is simplistic to the very least. However, a thorough discussion of the various theoretical assumptions involved in the estimate of the proposed trends is out of the scope of the present work.

On the other hand, at higher momenta the LIDO curve is a better representative of the data. Here, a feature that could make the difference is the nature of transport coefficients (relevant in the diffusion stage through the medium). In fact, while in the TAMU case they are computed through non-perturbative QCD, in the LIDO approach they are tuned to reproduce experimental observables. Still, other differences are expected to come into play, as for instance the inclusion of scattering and radiative processes. Incidentally, TAMU description lacks such mechanism, which would further justify the overestimation for higher momenta.

Comparison with Latest Approved Experimental Results

To conclude, a comparison of the outcome of the present analysis (involving data collected in 2018) with the results stemming from 2015 measurements [10] is considered. The discussion is based on figure 4.16, reported below. Data points and accompanying uncertainties from 2015 measurements are represented in shades of orange and black. Until interval 10-12 GeV/c, bin size is doubled with respect to the present analysis, whereas thereon the binning is identical for the two cases. Logarithmic scale is used for the horizontal axis to highlight low-p_{T} behaviour. Higher statistics of 2018 measurements is visible in overall considerable enhancement of statistical uncertainties. Systematic uncertainties are roughly halved (in absolute value). This is partly due to globally lower values of the nuclear modification factor. On the other hand, 2015 systematic contributions on the D-meson yield in Pb–Pb collisions were estimated considering the following sources: (i) extraction of the raw yield from the invariant-mass distributions; (ii) track reconstruction efficiency; (iii) D-meson selection (cut) efficiency; (iv) PID efficiency; (v) generated D-meson pT shape in the simulation; (vi) subtraction of the feed-down from beauty-hadron decays [10]. Since only the PID efficiency contribution has been neglected in this work,[10] the decrease must also be due to a somewhat important suppression of the primary contributions, i.e., those coming from the yield extraction, the cut efficiency and the track efficiency.

---

[10] This contribution is below 1% in both cases.

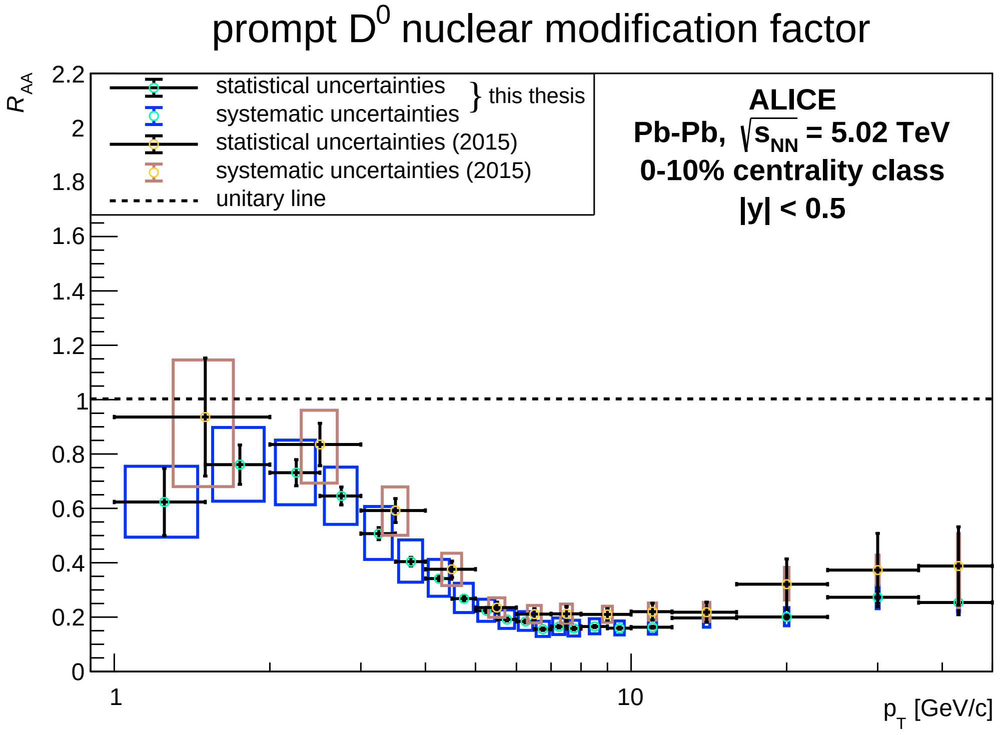

Figure 4.16: Prompt D^0 nuclear modification factor in (1.0, 50.0) GeV/c. This thesis measurements and measurements published in [10] are compared.

In general, the most distinctive feature between the two cases is the stably larger magnitude of the 2015 quantity. The low-p_T bump is not observed in such case. On the other hand, while the bin-wise difference changes as momentum varies, there does not seem to be a considerable horizontal shift between the two curves. Except for the bump, a similar decrease leads to a common stationary region in the neighbourhood of 8 GeV/c, to then evolve into a mild growth from 10 GeV/c on. At the same time, significantly larger discrepancies are observed for low and high momentum. These are important, as they modify the physical interpretation corresponding to the experimental curve, depending on the compatibility with the various theoretical models.

The 2018 finer binning, allowed by higher statistics, increases the likelihood that important features of the quantity under study do not go overlooked (e.g., the bump), partly by reducing the degree of approximation used in various contexts (e.g., the MC p_T-shape), partly by better probing the momentum dependence for the considered quantities. Future improvements are also expected in this respect, thanks to the setup upgrade that will lead to a notable increase in statistics through enhanced spatial resolution.

Chapter 5

A Multivariate Significance Study

In the previous chapters of this thesis, the extraction of signal coming from prompt D^0 mesons produced in lead-lead collisions at ALICE experiment has been carried out. The selection of optimal topological cuts is a crucial stage of such process and it is performed by probing a dense space of cuts configurations, for each of which the statistical significance of the signal is estimated by a MC sample of neutral D mesons and the actual data background. The set of cuts maximising such quantity is chosen as the best and then used in the actual extraction. This is performed for every transverse momentum interval considered in the analysis.

The optimisation procedure of chapter 3 is traditional in the sense that a “brute-force” approach is taken when assessing the value of the significance for thousands of cuts configurations. Another possibility in this context is the usage of multivariate analysis techniques, usually referred to as Machine Learning (ML) tools. These have as a goal the fitting of a trend in its most general sense, and can serve as binary/multiple classifiers and regressors. In general, all of these can be thought of as function-fitting algorithms.[1] In the classification case, the outcome of a process is determined by a set of *explanatory* variables. It is straightforward to see how this applies to the present case, with the purest separation between prompt D^0 mesons and background as a function of topological variables being the desired outcome.

Multivariate techniques can belong to the family of *supervised* or *unsupervised* learning algorithms. The former make use of training events, for which the desired output is known, to determine the mapping function (predictor) that either describes the decision boundary or approximates the underlying functional behaviour defining the target value [36]. At any rate, a validation stage always follows the estimation of the predictor, which, if passed, permits its usage in actual regression problems.

Nowadays, several of these techniques are available, having evolved considerably with respect to the fundamental algorithms they are based on. This progress is due to the

---

[1] For instance, a simple yes/no scenario can be represented by using a sigmoid function: $\Sigma(\vec{x}) = \Pi_i[(1 + e^{-x_i})^{-1}]$.

classification power these tools have shown to possess in various fields, among which the natural sciences.

In this chapter, the effectiveness of *Boosted Decision Trees* as a supervised learning algorithm is assessed, in particular probing the complex signal extraction at low transverse momenta. The concept of binary decision tree is first illustrated, as the basic ingredient to carry out the later analysis. At the same time, fundamental ideas of ML algorithms, i.e., training, overtraining and validation/test are discussed. The second half of the chapter focuses on the analysis results, obtained with the same statistics used for the concerned p_{T} interval in the cut optimisation of chapter 3. This way, a comparison between the statistical significance in the two cases can be set, thus investigating the possibility of an enhancement of signal extraction by means of multivariate boosted decision trees.

5.1 Decision Trees

Decision trees are amongst the most intuitive multivariate analysis techniques. In fact, even their more complex forms are based on a *binary decision tree*, a structure as the one presented in figure 5.1 (a). A binary tree subdivides the space of explanatory variables in a set of rectangles (figure 5.1 (b)) on the basis of which subdivision achieves the best separation, proceeding in order of classification power of the variables.[2] As an example, consider figure 5.1: at the beginning (root node) the dataset is split at value $x_1 = \vartheta_1$: the bound leading to highest separation as far as such variable is concerned. The same procedure is carried out again for both new partitions, employing the variable x_2, and so on, for other possible variables. The splitting usually stops when no further separation can be accomplished.

The decision tree algorithm basically consists in a hyper-rectangular recursive subdivision of the space spanned by the explanatory variables, with boundaries that can be represented as trivial constant functions in given ranges (defined by previous bounds). Each region is characterised by a class that basically represents the majority of instances contained therein (in the present context, signal and background). The most important property of the recursive binary tree is its interpretability, as opposed to more complex machine learning techniques like neural networks.

5.1.1 Training

Decision trees ultimately provide a piecewise constant approximation to the discrete-valued function that is being modelled, the ideal classifier. In the limit of point-like binning and infinite dataset such object would be obtained. Correspondingly, a binary tree has

---

[2] Here, the term separation is used because the purpose of the present analysis is classification. However, trees are used also as regression tools. In such case, they are referred to as regression trees.

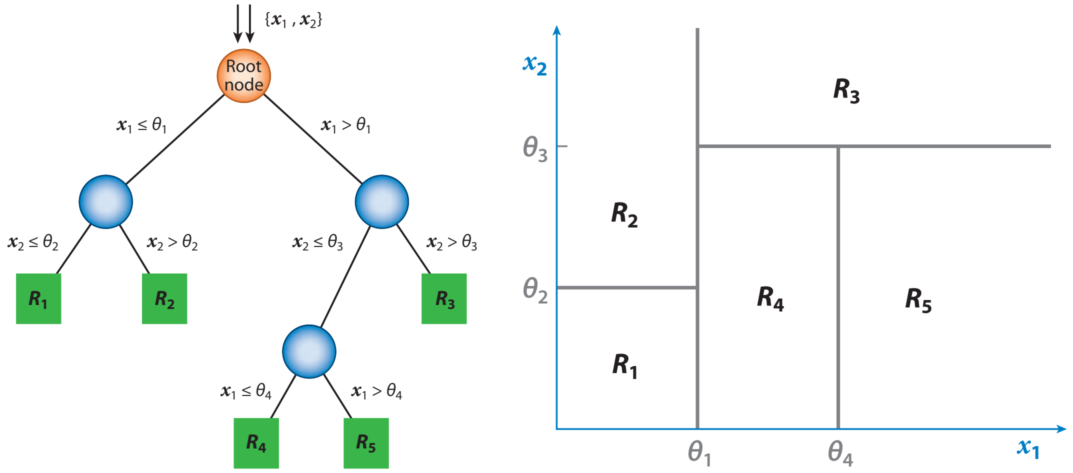

(a) *Binary decision tree diagram.* (b) *Two-variable space DT subdivision.*

Figure 5.1: A schematic of a binary decision tree with two feature variables, x_1 and x_2 and illustration of the corresponding partitions of the two-dimensional feature space [37].

the following important features, crucial to the training stage, that also propagate when performing the real classification:

- Grid points;

  The points to be probed as bounds within the intervals spanned by each explanatory variable.

- Depth;

  The maximum number of times the dataset can be sequentially partitioned. In figure 5.1 (a), this number is 3, as the right-hand side branch is further split twice after the first cut.

- Cost function.

  The cost function is a χ^2−like quantity in the sense that its goal is quantifying the quality of the provided mathematical representation of the ideal classifier. In particular, it is oftentimes used as a criterion to stop node splitting. The cost functions preferred when working with binary trees are Gini Index and the Information Entropy. In the present work, Gini index [38] is employed:

  $$g = \sum_{k}^{K} p_{mk}(1 - p_{mk}); \tag{5.1}$$

  where:

  $$p_{mk} = \frac{1}{\mathrm{N}_m} \sum_{x_i \in R_m} I(y_i = k). \tag{5.2}$$

  In practice, at each node, region R_m is assigned the quantity p_{mk}, which gives the fraction of instances correctly classified as belonging to class k (among K total

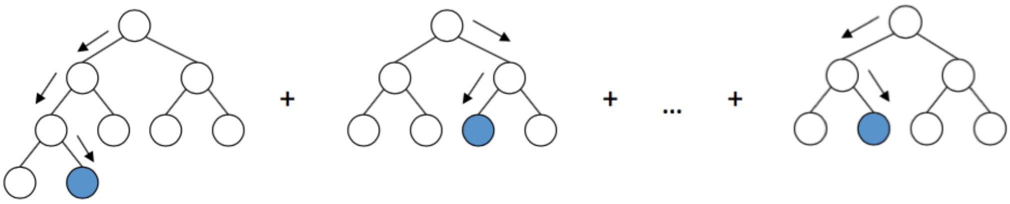

Figure 5.2: In ensemble learning, the different outcomes of a forest of decision trees are combined into a global response function, on the basis of which each candidate is ultimately classified. Figure adapted from Alex Rogozhnikov GitHub Blog: Gradient Boosting Explained.

classes). The index can then be conceived of as the training error rate of the node, if p_{mk} is interpreted as the probability of $x_i \in R_m$ instance to pertain to class k.

5.1.2 Ensemble Learning. Boosting

Binary classification trees are usually unstable with respect to statistical fluctuations biasing the training dataset the final subdivision stems from. This is the case, for instance, when two explanatory variables are close in classification power. In such scenario, a fluctuation may determine an outcome different from the optimal one, thus leading to an overall alteration in the tree growth, starting from the concerned node. This may have sizeable consequences in the classification. An effective way to deal with this issue is working with an ensemble of trees, that is, a *forest*: doing so, high-quality classifiers can be built combining modest predictors [37]. A pictorial representation of a forest of decision trees is given in figure 5.2.

The forest is built upon the same training sample, with events being reweighed tree by tree (misclassified events are given more importance): this is what is called (*adaptive*) *boosting*, and it is used in the present study.[3] A single classifier is eventually extracted in the form of an average of the various trees. Boosting provides the classifier with solid statistical stability and can notably enhance its performance with respect to a single tree. As a matter of fact, the "merging" of several modest classifier into a unique predictor has been shown to often perform best. In this sense, when working with forests it can be optimal to set low depth ($\sim 2, 3$) so as to prevent overtraining and at the same time limit interaction between explanatory variables.

---

[3] There are several kinds of boosting. For instance, another typology is based on the usage of a random subset of all variables, growing each tree in the forest employing only a resampled fraction of the training sample (Random Forest Boosting).

BDT Response Function

Forests assign a value to each candidate based on the outcomes of all of their trees. This number is the so-called *response function.* The response function characterising the various candidates has the precise form of average computed accounting for the class attributed to one candidate by all the trees. In the simple case of two classes, signal can be assigned the value 1, while background the value -1, for the entire forest. Each candidate, x_i, will then be characterised by a response function value:

$$f(x_i) = \frac{\sum_{j=0}^{\mathrm{N_{trees}}} I_j(y_i \equiv \text{signal})}{\mathrm{N_{trees}}}, \tag{5.3}$$

where $y_i = y_{x_i}$. The candidate-wise BDT response will thus range between -1 and 1.

In the case of a boosted forest, thus, no precise subdivision of the explanatory variable space is privileged. Instead, it is the response function to be used as a selection variable. In practice, cutting on such quantity, only those candidates that have a response function above the given threshold are kept as signal. Here, a suitable criterion to choose the bound is the maximisation of the statistical significance of the sample. Proceeding as explained, impactful topological cut variables (decay length, etc.) distributions are expected to change similarly as seen in the traditional analysis: after all, independently of the particular tree and node, the best separation will stably be achieved when the bound is set around a certain value because they are good signal-background classifiers. On the other hand, non-trivial changes can be observed for secondary cut variables distributions.

5.2 Low-p_T Range Analysis

Due to the large combinatorial background, the lowest transverse momentum interval, (1.0, 1.5) GeV/c, is the hardest as far as signal extraction is concerned. For this reason, multivariate boosted decision trees are used to perform a training/validation classification study on the sample in this interval, in view of the opportunity to exploit the power of such tool for actual signal extraction. To this end, the Root toolkit TMVA (Toolkit for Multivariate Data Analysis with Root) is utilised [36]. Used datasets are once again MC signal sample and actual data sidebands background of 5.02 TeV per nucleon pair lead-lead collisions in centrality class 0-10%.

In the context of multivariate analyses, it is customary to employ a (larger) fraction of the available dataset to train the algorithm, and the complementary as a test sample.[4] In this work, the main goal is assessing whether a BDT-based extraction could lead to better significance than the traditional analysis based on topological cuts, so, while training and test samples are kept separate, the usual convention is not adopted. Instead, in order

---

[4] Actually, three statistically independent samples should be used in order to carry out parameter optimisation, an overtraining study, and the performance validation.

to perform a meaningful comparison, the test set is chosen such that the background sidebands and the MC signal sample have precisely the same statistics as those used in the cut optimisation study (for the lowest-p_T interval) of chapter 3. In this way, the values of significance obtained in the two cases are indicators of whether the BDT algorithm is promising as an improver of low transverse momentum signal extraction.

5.2.1 Training

As a result of the TMVA training phase, a considerable amount of useful information concerning explanatory variables is extracted, besides assigning a net response value to each candidate. This quantity stems from the combination of classifications performed by a number of binary trees: one thousand in the present work. In figure 5.3 trees number 1 and 40 are shown as examples.

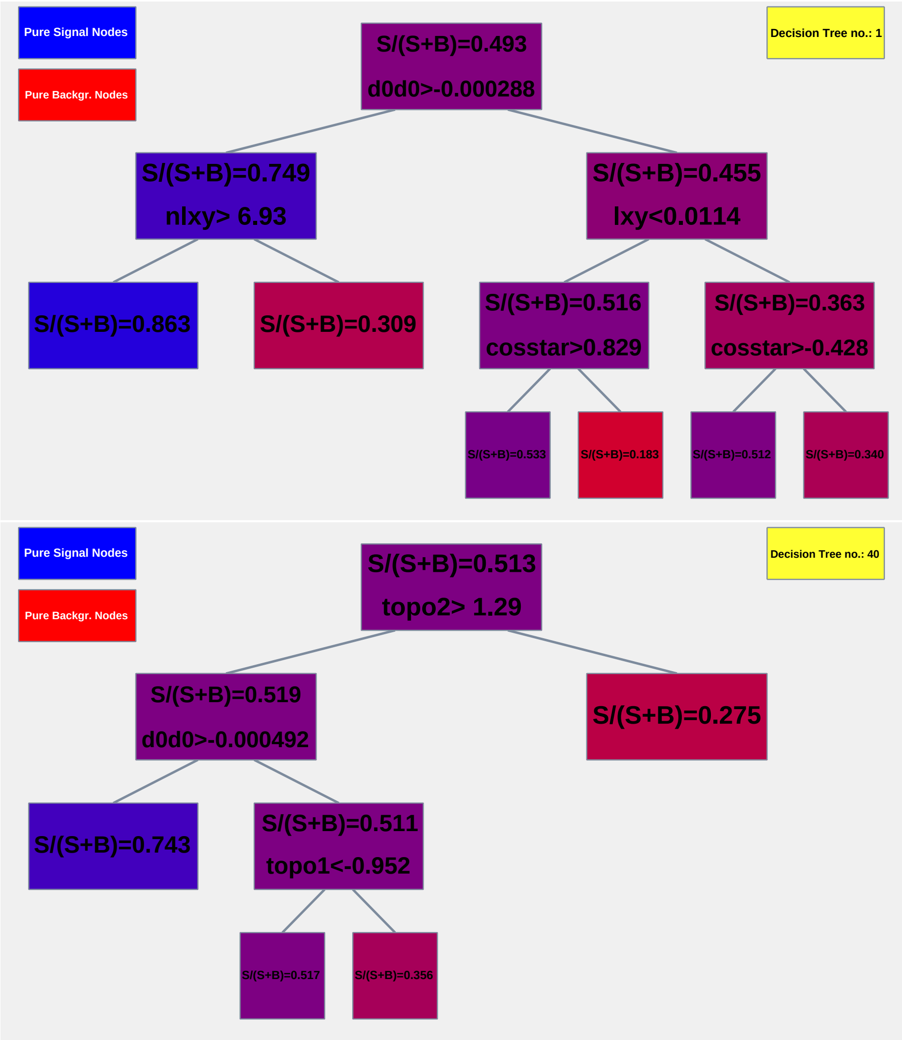

Figure 5.3: First and fortieth binary decision trees of the 1000-fold forest grown for the training phase. A half-signal, half-background dataset is used to train the algorithm. Blue and red rectangles indicate pure signal and background nodes, respectively.

As seen by the chromatic correspondence, pure signal or background nodes are not achieved, but a selection based on powerful topological variables like the normalised decay length and the product of impact parameters leads to a high degree of separation (tree number 1). Thus, as remarked previously, it is expectable that the distributions of these variables will be noticeably suppressed starting from a certain threshold for high-significance cuts on the response, in analogy with the traditional topological optimisation analysis. Such claim is confirmed by signal impact parameters product distribution of figure 5.4.

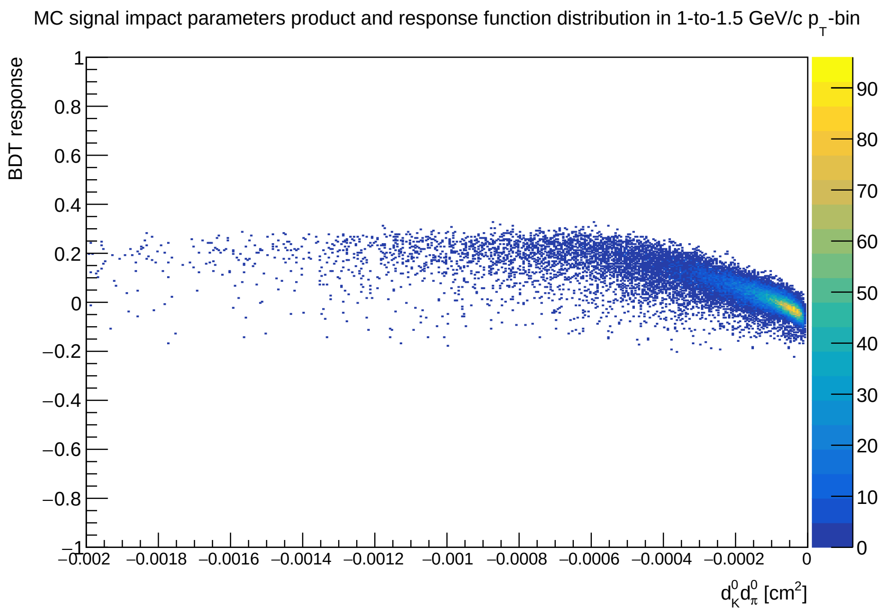

Figure 5.4: Signal impact parameters product and BDT response colour map.

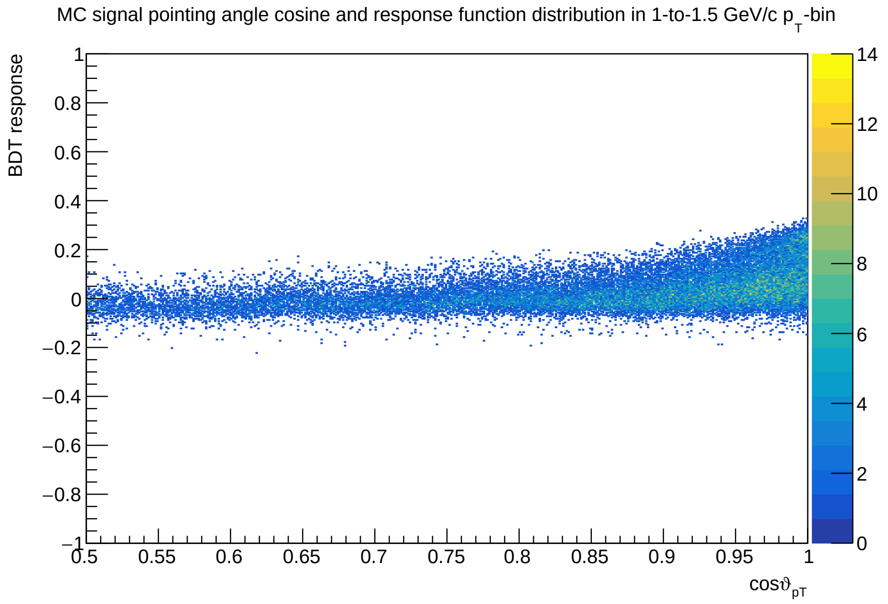

Figure 5.5: Signal pointing angle cosine and BDT response colour map.

As the BDT response (lower-bound) cut grows larger than zero, a notable rejection of candidates with relatively larger $\mathrm{d}_0^{\mathrm{K}} \times \mathrm{d}_0^{\pi}$ takes place, in agreement with topological arguments. This fact still holds for the pointing angle distribution, reported in figure 5.5. It does, however, much less evidently. This is partly due to the parallel usage of the transverse projection of pointing angle cosine and to the overall lower impact of this quantity as a separator, but also to the non-trivial link between the response and $\cos\vartheta_{\mathrm{pt}}$ as an explanatory variable. A lower-bound cut on the response retains more candidates at high values, in agreement with topological arguments, yet skimming the distribution throughout the entire range.

Parameters Optimisation

Figure 5.6 presents background and signal BDT response spectra. As expected, the two distributions are shifted in the response negative and positive directions, respectively. The selection of good candidates is ultimately performed by imposing a threshold on this quantity, and the retained sample features will differ depending on the chosen value. Signal and background efficiencies, the respective fractions conserved after cutting, will generally have a monotonous behaviour with the cut value; likewise will the signal purity – a signal-to-total yield ratio. The statistical significance will instead often show a more complex trend, as can be foreseen by considering its mathematical form. The cut is selected maximising the latter as done previously, keeping in mind its relation with the raw yield relative uncertainty.

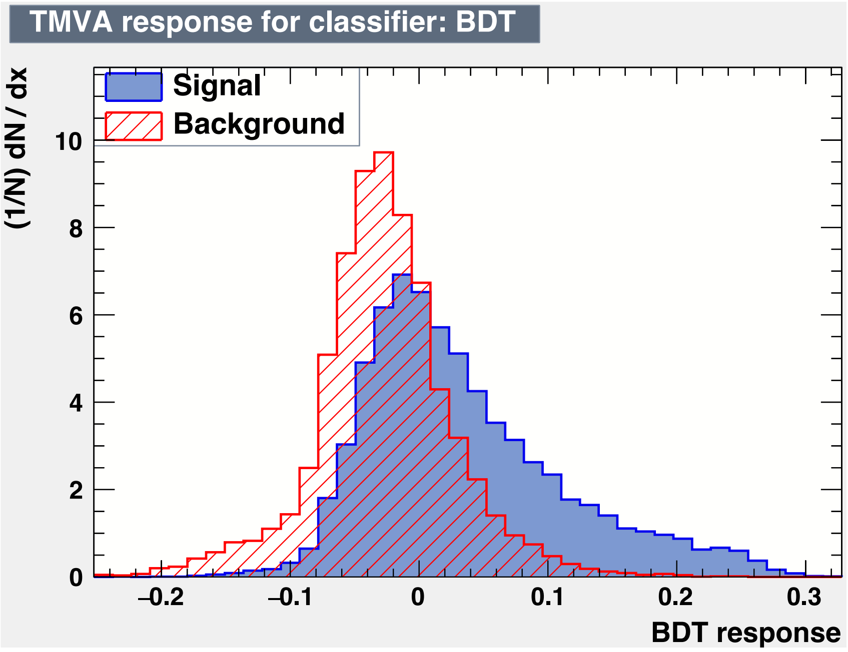

Figure 5.6: Background and signal BDT response spectra for training dataset.

The proposed response dependence (figure 5.7) is observed for these quantities, when considering a half-signal, half-background dataset. Of course, modifying the relative abundances of instances belonging to the two classes will change the various curves. However, at the training stage it is reasonable to set same magnitude samples, so as to equilibrate the optimisation and facilitate interpretation of the trees.

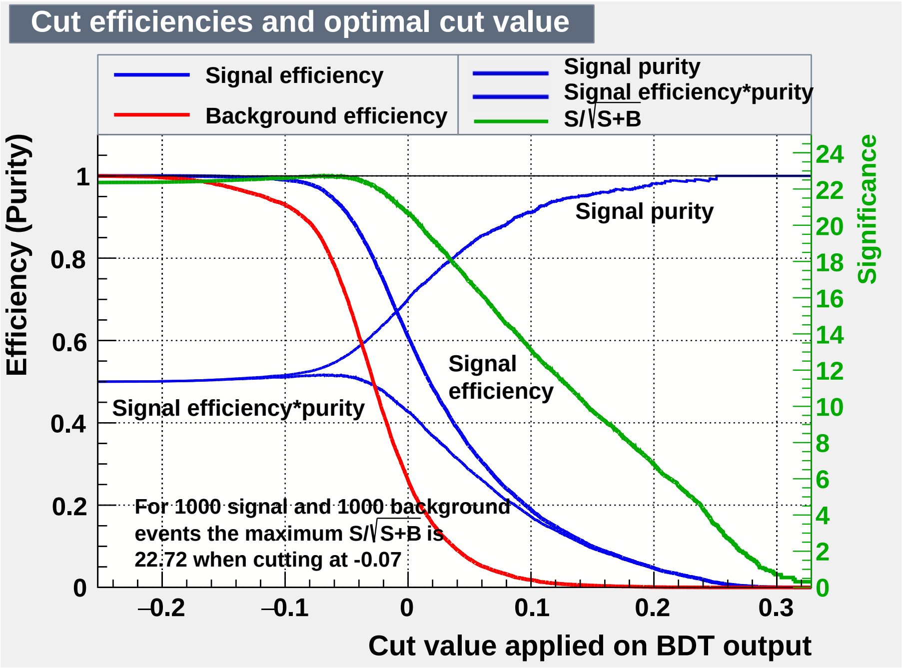

Figure 5.7: Signal and background efficiencies, and various other indicators of the achieved degree of classification as functions of cut on the BDT response.

Efficiencies and purity show the mentioned monotonic behaviour. The significance, instead, mildly grows up to a stationary point to then fall rapidly as the response value increases.

An exhaustive representation of the data samples used during the training stage, including the BDT response distribution for background and signal is reported in parallel coordinates figures 5.8 and 5.9.

5.2.2 Overtraining. Test. Statistical Significance

When the degrees of freedom of the employed multivariate algorithm "exceed" the complexity of the problems under study, the likelihood of overtraining, i.e., over-reproducing the features of the training set including possible fluctuations, is high. In such case, the classification of the test sample will be poorer. In order to avoid this scenario, an overtraining check is conducted as a first stage of the validation phase. In particular, the response distributions of background and signal should be reasonably similar in the training and test cases, as coming from the same ideal response probability distribution. In order to check such fact, one can operate qualitatively, i.e., by visually assessing the similarity (which will

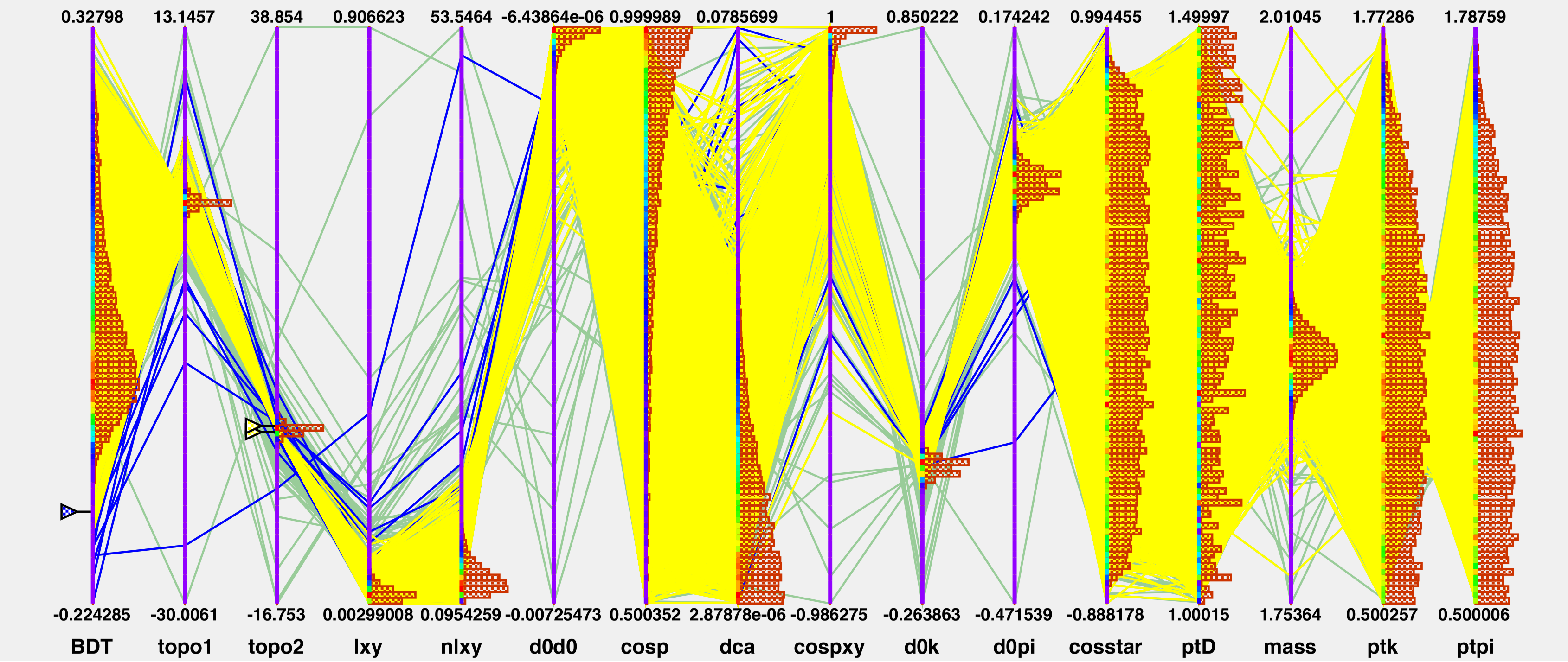

Figure 5.8: Signal parallel coordinates. The spectra appearing for each of the topological variables include all the signal instances used during training.

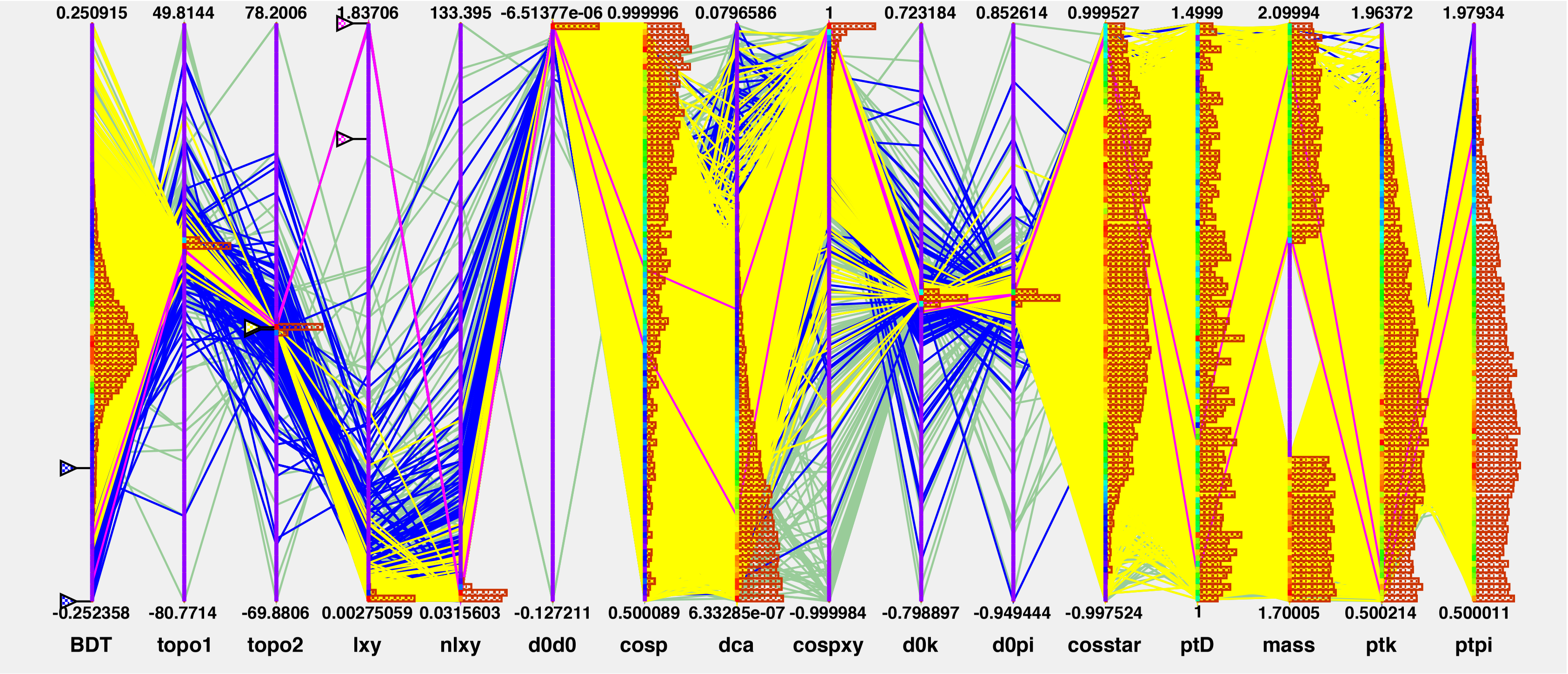

Figure 5.9: Background parallel coordinates. The spectra appearing for each of the topological variables include all the background instances used during training.

make the check not quite rigorous), or quantitatively, by means of a Kolmogorov-Smirnov test. In this work, the former way is preferred due to TMVA technical complications in the second approach [39]. Superposed distributions are presented in figure 5.10.

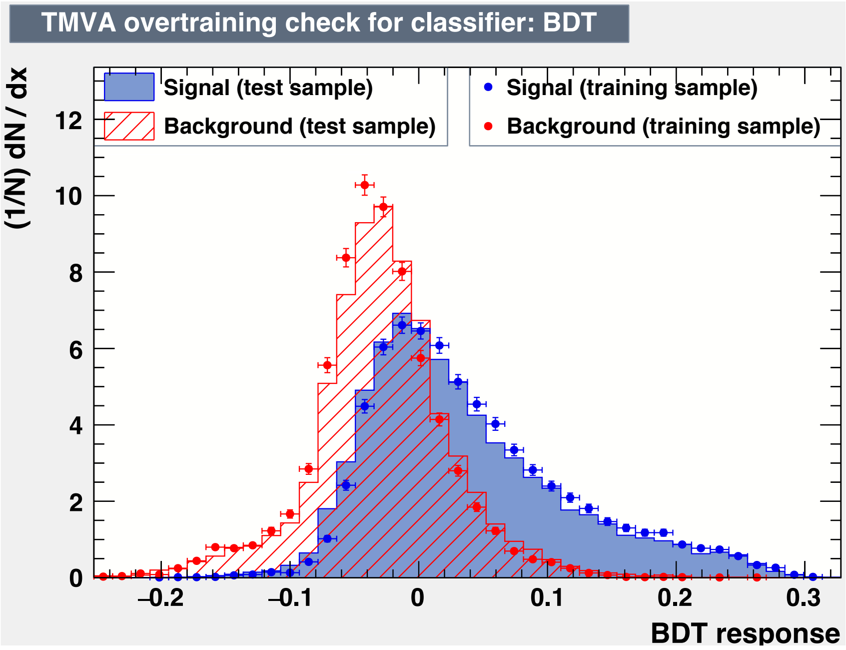

Figure 5.10: Overtraining check. Training and test signal and background distributions appear similar enough to proceed with the testing of the trained algorithm.

In absence of considerable fluctuations, the training and test histograms can be assumed to be products of the same signal and background distributions, thus discarding the overtraining hypothesis. This is the scenario observed above. The test stage and, more particularly, the significance assessment are thus undergone.

Significance

The application of the forest obtained as a result of training on the test dataset leads to the following significance curve as a function of BDT response. This is presented in figure 5.11. As mentioned, statistics for test signal and background samples has been chosen equal to that used in the topological cut optimisation analysis. The statistical significances obtained in the two cases are thus comparable.

It is apparent that this quantity can reach moderately higher values in the multivariate case. This happens for a continuous range for a cut on the response. Correspondingly, it is expected that the usage of the present trained forest on experimental data lead to slightly better signal extraction. Of course, the systematic sources of deviation related to the discrepancies between simulations and experimental reality are to affect the outcome of such extraction. However, considering what seen in previous chapters, it is not expected to prove wrong the present claims. It is thus concluded that the BDT-based signal extraction

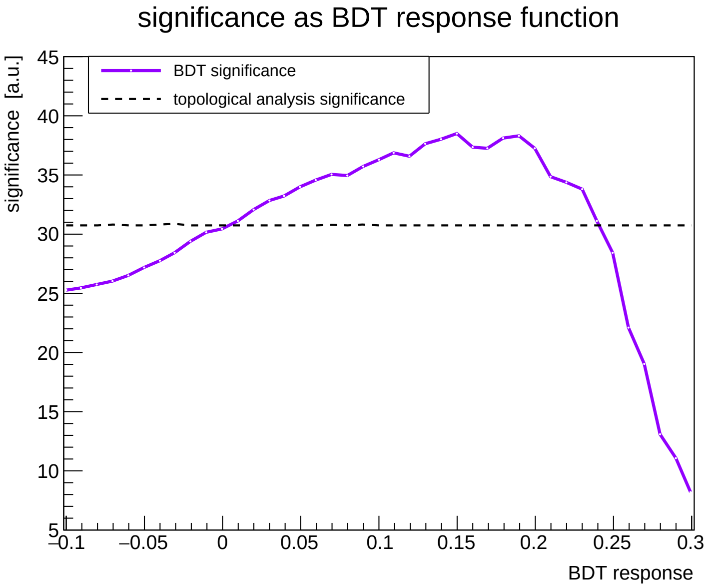

Figure 5.11: Significance trend as a function of BDT response in the neighbourhood of zero. A larger value than the maximum significance of chapter 3 analysis is observed for a cut between 0 and 0.25 .

is a promising prospect. As a matter of fact, it could also be carried out on other p_T intervals, while searching for individual optimal binary tree configuration as a potential further improvement. At the same time, the magnitude of the improvement is such that results obtained in the traditional way can be regarded as satisfactory. Conclusively, these two approaches can work jointly: the solidity of the topological analysis can be complemented by the power of multivariate tools, thus leading to sizeable improvements in signal extraction and possibly allow the search for rare objects that can be produced in high energy processes. An instance of these are exotic hadrons expected to form through quark coalescence in the medium, such as (multiply) heavy flavoured baryons (Ξ_c^+, Ξ_{cc}^{++}, etc.). These particles, whose yields are predicted to be spectacularly enhanced in heavy-ion collisions as opposed to the proton-proton case [40], could be sought by means of their multiple hadronic decay chains, with such a measurement ultimately contributing to deepen the understanding of formation mechanisms in the deconfined QCD plasma.

Conclusions

This thesis work has quantified the production of charmed D^0 mesons in lead-lead collisions with the ALICE experiment at the CERN LHC. In particular, the observables of interest that have been measured are the transverse momentum spectrum and the nuclear modification factor. Two radically different approaches in the optimisation of the selection conditions of prompt D^0 signal have been studied. Such process is essential to carry out the aforementioned measurements, which can be particularly challenging in the low transverse momentum range ($p_{\mathrm{T}} \lesssim 3$ GeV/c), thus calling for a dedicated study.

Results stemming from standard rectangular cuts search of the best topological selections have been used to evaluate the quantities of interest. On the other hand, the statistical significance, as a measure of the classification capability of either algorithm, has been employed (in conditions of same statistics) to compare the effectiveness of the former with the conditions established by means of multivariate Boosted Decision Trees. This study has brought about preliminary results in the direction of similar classification power for the two methods, considering that no drastic improvement has been observed in the second case with respect to the first. Notwithstanding, second-order features of the multivariate algorithm could be investigated as sources of further improvement. At the same time, the optimisation strategy used to obtain results could be refined: more topological variables could be dealt with simultaneously, the search resolution could be increased, etc.

Post-selection invariant mass analysis of fully reconstructed topologies originated from the D^0 decay has allowed signal extraction. Throughout this process systematic effects affecting the accuracy of results have been introduced. The corresponding systematic uncertainties have been subsequently estimated. In general, they do not exceed 20%, except for the lowest-significance p_{T} intervals, i.e., the lowest and highest in transverse momentum. The same holds for statistical uncertainties.

The transverse momentum spectrum of charmed mesons is subject to sizeable changes when heavy-ions collide and evolve into a strongly-interacting macroscopic system, with respect to the case of nucleon-nucleon reactions. Both nuclear and quantum-chromodynamics effects contribute in such situation. These changes have been normalised to the QGP-free scenario of proton-proton collisions through the computation of the nuclear modification factor. Employing the extracted spectrum, along with previous measurements, such quantity has been calculated and compared to theoretical models and past experimental results, in the latter case highlighting sensible increase in statistics, which has permitted finer binning and smaller relative uncertainties. From the theoretical standpoint, models do reproduce observations, although none of them provides a satisfactory description in the entire momentum range that has been probed. This is not unexpected, given the concurring mechanisms involved in the description of the production and interaction of D^0 mesons in a QGP.

As an outlook, upgrade of ITS, TPC and other parts of the ALICE setup, that will lead to higher accuracy and precision in measurements, along with ever-improving models, are expected to further deepen the understanding of heavy flavour energy loss mechanisms in the plasma. In the future, focus will be directed also towards the production of exotic multiply heavy flavoured baryons. These would provide a direct window on hadron formation from a deconfined QGP, and since spectacular enhancement effects would be expected in the case of heavy-ion collisions [40], they constitute an important future area of measurement in the field of ultra-relativistic heavy-ion physics.

Bibliography

[1] Michael L. Miller, Klaus Reygers, Stephen J. Sanders, and Peter Steinberg. Glauber Modeling in High-Energy Nuclear Collisions. *Ann. Rev. Nucl. Part. Sci.*, 57:205–243, 2007.

[2] Carlos A. Salgado. Lectures on high-energy heavy-ion collisions at the LHC, 2009. arXiv:0907.1219.

[3] Andrea Festanti. Measurement of the D0 meson production in Pb–Pb and p–Pb collisions with the ALICE experiment at the LHC, PhD Thesis, Università degli Studi di Padova, 2015.

[4] ALICE Collaboration. Centrality determination of Pb-Pb collisions at $\sqrt{s_{NN}} = 2.76$ TeV with ALICE. *Phys. Rev. C* 88 (2013) 044909. arXiv:1301.4361.

[5] Reinhard Stock (Editor). Encyclopedia of Nuclear Physics and its Applications. Wiley, 2013.

[6] Matthew D. Schwartz. Quantum Field Theory and the Standard Model. Cambridge University Press, 2014.

[7] R. Hagedorn. Statistical Thermodynamics of Strong Interactions at High Energy. *Suppl. Nuovo Cimento*, 3:147, 1965.

[8] Martin Wilde for the ALICE Collaboration. Measurement of Direct Photons in pp and Pb–Pb Collisions with ALICE. *Nuclear Physics A* 904–905 (2013) 573c–576c. arXiv:1210.5958.

[9] M. Tanabashi et al. (Particle Data Group). PDG, The Review of Particle Physics. *Phys. Rev. D* 98, 030001 (2018).

[10] ALICE Collaboration. Measurement of D^0, D^+, D^{*+} and D_s^+ production in Pb-Pb collisions at $\sqrt{s_{NN}} = 5.02$ TeV. *JHEP* 1810 (2018) 174. arXiv:1804.09083.

[11] Lyndon Evans and Philip Bryant. LHC Machine. 2008 *JINST* 3 S08001.

[12] Werner Herr and Bruno Muratori. Concept of luminosity. 2003.

[13] A. Kalweit. Highlights from the ALICE experiment. *Nuclear Physics A* 982 (2019) 1–7.

[14] John Jowett. LHC Report: entering the last week of the heavy-ion run. 2018.

[15] ALICE Collaboration. The ALICE experiment at the CERN LHC. 2008 *JINST* 3 S08002.

[16] ALICE Data Preparation Group. ALICE Data Flow. 2018.

[17] R. Fruhwirth. Application of Kalman Filtering to Track and Vertex Fitting. *Nuclear Instruments and Methods in Physics Research Section A: Accelerators, Spectrometers, Detectors and Associated Equipment*, 262(2–3):444–450, 1987.

[18] ALICE Collaboration. Performance of the ALICE experiment at the CERN LHC. *International Journal of Modern Physics A Vol.* 29, No. 24 (2014) 1430044.

[19] Torbjorn Sjostrand, Stephen Mrenna, and Peter Z. Skands. PYTHIA 6.4 Physics and Manual. *JHEP*, 0605:026, 2006.

[20] Xin-Nian Wang and Miklos Gyulassy. HIJING: A Monte Carlo Model for Multiple Jet Production in pp, pA and AA Collisions. *Phys. Rev. D*, 44:3501–3516, 1991.

[21] GEANT. A simulation toolkit.

[22] Andrea Dainese. Charm production and in-medium QCD energy loss in nucleus–nucleus collisions with ALICE. PhD Thesis, Università degli Studi di Padova, 2003.

[23] Andrea Rossi. Charm production in proton-proton collisions at the LHC with the ALICE detector. PhD Thesis, Università degli Studi di Trieste, 2010.

[24] Padova University ALICE Group. Private Correspondence.

[25] M. Cacciari, M. Greco and P. Nason. The p_{T} spectrum in heavy flavor hadroproduction. *JHEP* 05 (1998) 007. arXiv:hep-ph/9803400.

[26] M. Cacciari, S. Frixione and P. Nason. The p_{T} spectrum in heavy flavor photoproduction. *JHEP* 03 (2001) 006. arXiv:hep-ph/0102134.

[27] Lennart van Doremalen. Beauty of the Quark Gluon Plasma. Prospect for B^0 measurement in ALICE. Master Thesis, Utrecht University, 2017.

[28] ALICE Collaboration. ALICE Off-line Project.

[29] P. Hristov. AliRoot Primer.

[30] ALICE Collaboration. Measurement of D^0, D^+, D^{*+} and D_s^+ production in pp collisions at $\sqrt{s} = 5.02$ TeV with ALICE. 2019. arXiv:1901.07979.

[31] CMS collaboration. Suppression and azimuthal anisotropy of prompt and nonprompt J/Psi production in PbPb collisions at $\sqrt{s_{\mathrm{NN}}} = 2.76$ TeV. *Eur. Phys. J. C* 77 (2017) 252. arXiv:1610.00613.

[32] Jan Uphoff, Oliver Fochler, Zhe Xu, and Carsten Greiner. Open Heavy Flavor in Pb–Pb Collisions at $\sqrt{s_{\mathrm{NN}}} = 2.76$ TeV within a Transport Model. *Phys. Lett. B*, 717:430–435, 2012.

[33] Weiyao Ke, Yingru Xu, Steffen A. Bass. A linearized Boltzmann–Langevin model for heavy quark transport in hot and dense QCD matter. *Phys. Rev. C* 98, 064901 (2018). arXiv:1806.08848.

[34] Min He, Rainer J. Fries, Ralf Rapp. Heavy Flavor at the Large Hadron Collider in a Strong Coupling Approach. arXiv:1401.3817.

[35] Salvatore Plumari, Vincenzo Minissale, Santosh K. Das, Gabriele Coci, Vincenzo Greco. Charmed Hadrons from Coalescence plus Fragmentation in relativistic nucleus-nucleus collisions at RHIC and LHC. *Eur.Phys.J.C* (2018) 78:348. arXiv:1712.00730.

[36] A. Hoecker, P. Speckmayer, J. Stelzer, J. Therhaag, E. von Toerne, H. Voss. TMVA 4. Toolkit for Multivariate Data Analysis with ROOT. Users Guide. arXiv:physics/0703039.

[37] Pushpalatha C. Bhat. Multivariate Analysis Methods in Particle Physics. *Ann.Rev.Nucl.Part.Sci.* 61 (2011) 281-309.

[38] Trevor Hastie, Robert Tibshirani, Jerome Friedman. The Elements of Statistical Learning. Springer, 2009.

[39] ROOT Forum: Kolmogorov-Smirnov test values.

[40] ALICE Collaboration. A next-generation LHC heavy-ion experiment. arXiv:1902.01211.